CHAPTER 3

UNSYMMETRICAL MESOGENIC DIMERS OF CYANOAZOBENZENE AND AZO/ AZOMETHINE NAPHTHALENE

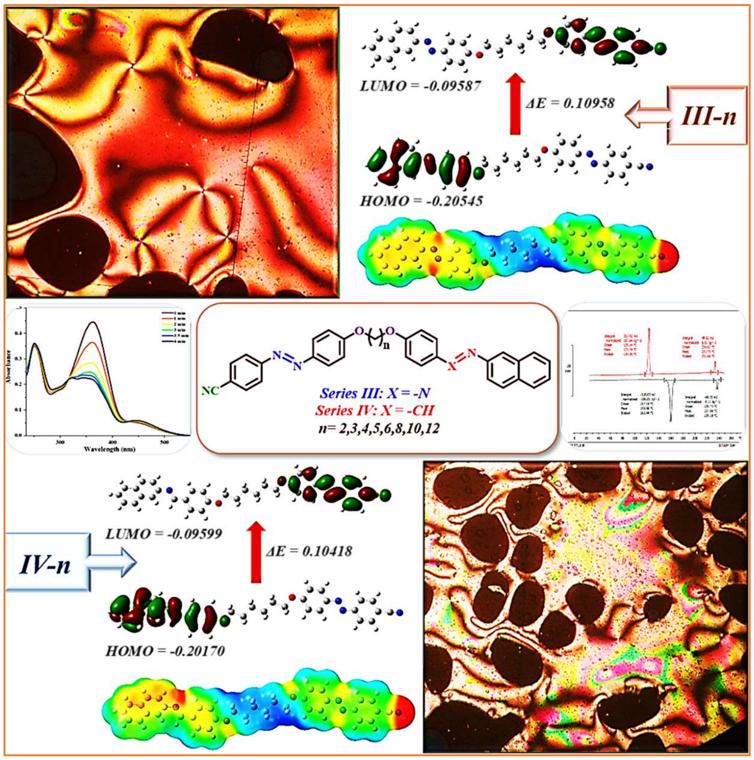

3.1 Introduction

Liquid crystal (LC) dimers are molecules composed of two mesogenic units separated by a flexible spacer, commonly an alkyl chain. They are attracting significant attention due to their role as model compounds for both main chain and side chain liquid crystalline polymers.[1] There are two main types of dimers: symmetric dimers, where both mesogenic units are identical, and non-symmetric/ unsymmetrical dimers, where the two mesogenic groups differ. Non-symmetric dimers stand out for their intriguing polymorphic properties.[2] The introduction of non-symmetry in dimers can be achieved by connecting different mesogenic units, adjusting the length of terminal chains/flexible spacers, employing diverse terminal groups and evenness of the spacer group.

Dimers containing azobenzene moieties are particularly noteworthy due to their unique characteristics. Understanding the different types of liquid crystal dimers and their properties is crucial for developing new materials with tailored optical and electronic properties. Various unsymmetrical liquid crystalline dimers with azo linakges have been extensively explored in recent years, elucidating their mesomorphic behaviours and structure-property relationships.[3] **Fig. 3.1** shows some examples of unsymmetrical LC dimers containing azo linkages. Subala et al. introduced dimers containing biphenyl and azobenzene segments linked by flexible spacers, altering paraffinic chain lengths while keeping terminal alkyl and alkoxy tails constant, resulting in enantiotropic mesomorphism.[4] Paterson et al. focused on azobenzene-based dimers designed for the NTB phase.[5] Bai et al. synthesized dimers incorporating azobenzene and 1,3,4-oxadiazole groups, with dimers exhibiting a monolayer smectic A phase.[6] Chan et al. reported unsymmetrical dimers with an isoflavone-based moiety.[7] Martínez-Felipe and Imrie investigated dimers involving hydrogen bonding, utilizing benzoic acid and pyridyl fragments, and varying spacer lengths to study transitional properties.[8] Pan et al. explored disc-rod shape-amphiphilic dimers with triphenylene and azobenzene mesogens.[9] Varia et al. studied T-shaped dimers with biphenyl nuclei and various flexible spacers, identifying mesophases in the series.[10] Prasad et al. synthesized non-symmetrical dimers with bent-core and rod-like monomers linked by flexible alkylene spacers, observing diverse mesophases including N, SmA, SmC, and Col_x, and studying the influence of polar –CN end groups on mesomorphic properties.[11]

Cyanoazobenzene has gained attention as a promising component for LC dimers due to its unique photo-responsive properties. The azobenzene unit can undergo reversible *trans-cis* isomerization upon exposure to light, which can lead to changes in the LC phase behaviour and optical properties, making them potential candidates for applications in optoelectronics and optical data storage [12,13]. There have been reports of tetrasubstituted tetrathiafulvalenes (TTFs) that contain photo responsive 4-cyanoazobenzenyl units which show liquid crystalline properties[14].

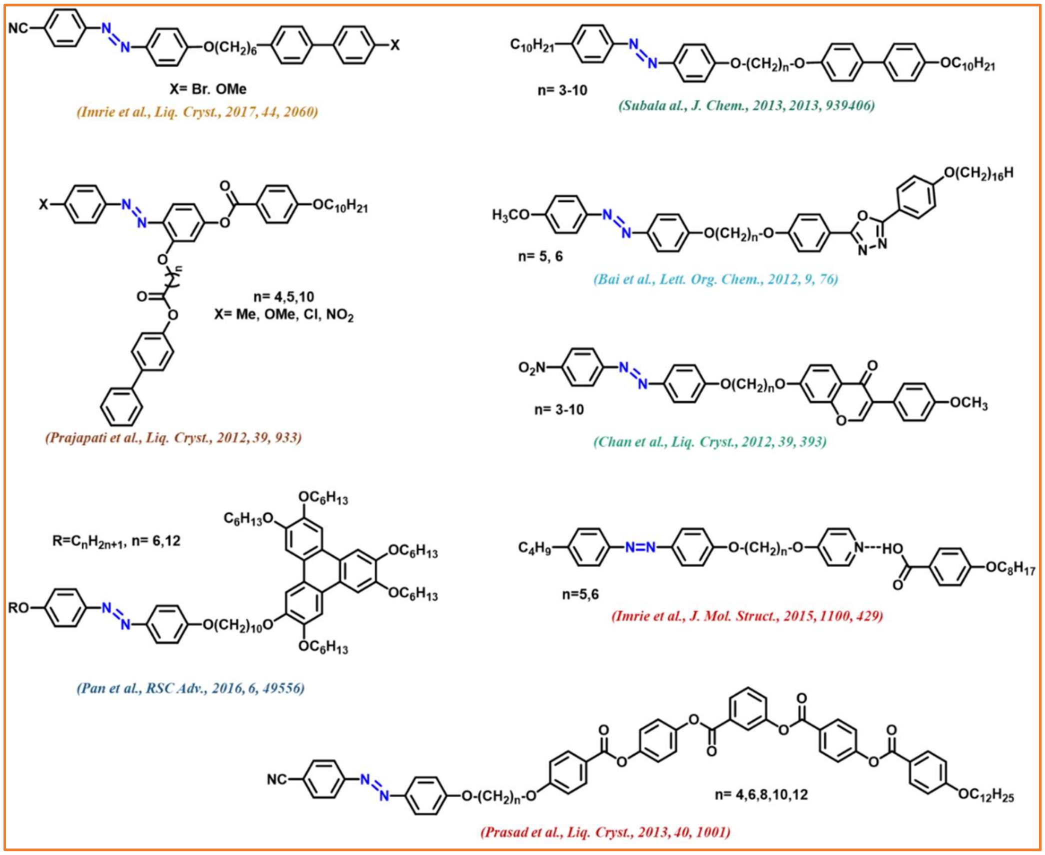

Fig. 3.1: Some examples of Unsymmetrical LC dimers containing azo linkages

Schiff base linkages, also known as azomethine linkages, play a significant role in the field of liquid crystals due to their unique properties that influence the behaviour of liquid crystal materials. **Fig. 3.2** illustrates several examples of unsymmetrical liquid crystal dimers incorporating azomethine linkages. These dimers showcase the diverse structural variations possible within this class of compounds, highlighting the versatility of azomethine linkages in liquid crystal design. Each molecule presents unique arrangements of functional groups and substituents, which can significantly influence the mesomorphic behaviour. Yeap et al. introduced a series of dimers with diverse terminal substituents, exhibiting enantiotropic chiral nematic phases.[15,16] They also investigated dimers with varying flexible spacers, showing high thermal stability and an enantiotropic N phase.[17] Another study by Yeap et al. presented dimers, incorporating benzothiazole and benzylideneaniline core units, with promising liquid crystal properties.[18] A new set of asymmetrical dimeric molecules, featuring a Schiff-base and a chalcone, was synthesized and investigated for liquid crystal and fluorescence properties.[19] Imrie et al. reported unsymmetrical liquid crystal dimers with a Schiff base and nitroazobenzene, observing nematic-isotropic transition behaviour influenced by spacer length.[20] Luckerhust et al. explored non-symmetric dimers with cyanobiphenyl and Schiff base, noting alternating transition temperatures based on spacer length.[21] Our group has reported unsymmetrical liquid crystalline dimers with a rigid biphenyl core and an ether-linking group attached with Schiff base.[22]

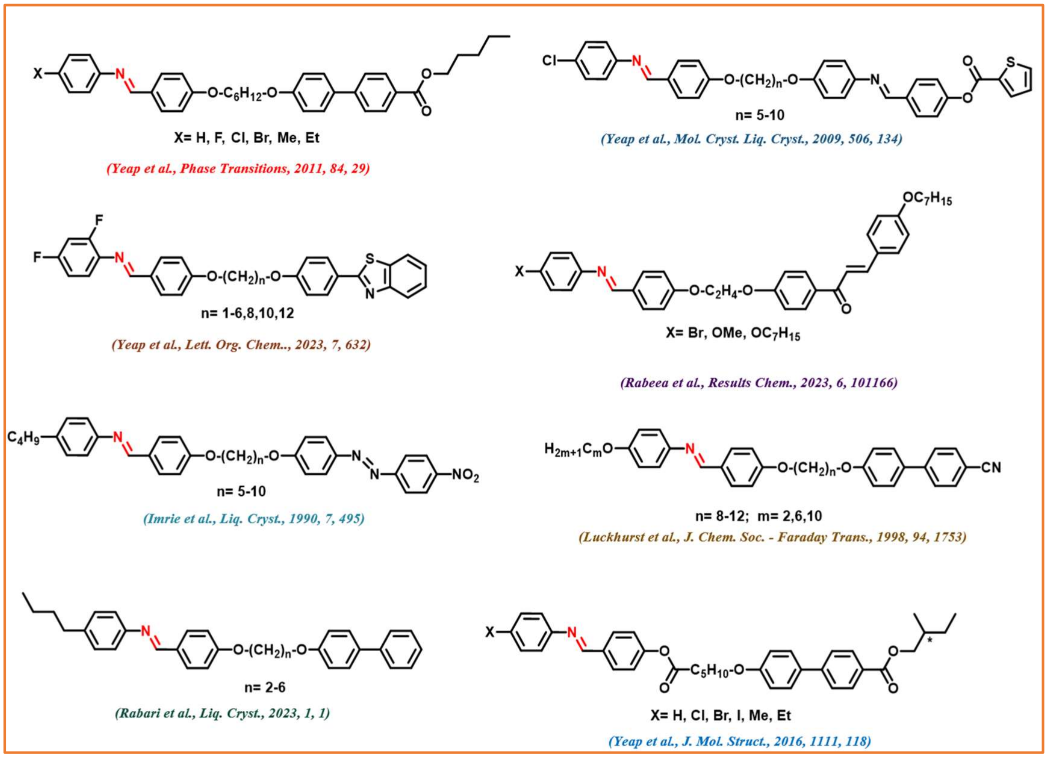

(Yeap et al., Phase Transitions, 2011, 84, 29)

(Yeap et al., Mol. Cryst. Liq. Cryst., 2009, 506, 134)

(Yeap et al., Lett. Org. Chem.., 2023, 7, 632)

(Rabeea et al., Results Chem., 2023, 6, 101166)

(Imrie et al., Liq. Cryst., 1990, 7, 495)

(Luckhurst et al., J. Chem. Soc. - Faraday Trans., 1998, 94, 1753)

(Rabari et al., Liq. Cryst., 2023, 1, 1)

(Yeap et al., J. Mol. Struct., 2016, 1111, 118)

Fig. 3.2: Some examples of Unsymmetrical LC dimers containing azomethine linkages

3.2 Objectives

The objective of our work is to synthesis of unsymmetrical liquid crystalline (LC) dimers to investigate the influence of naphthalene moieties on mesomorphism. While unsymmetrical dimers incorporating azobenzene and azomethine linkages with various mesogenic cores have been extensively reported, those utilizing simple aromatic units are relatively scarce. Given that naphthalene moieties tend to increase the breadth of molecules, there's a concern that they might diminish the likelihood of exhibiting LC properties. To address this, we have chosen to incorporate naphthalene moieties into our dimers and synthesized two series of compounds. In ***Series III-n***, one end contains cyanoazobenzene moiety while the other end contains azo naphthyl, whereas in ***Series IV-n***, the other end contains azomethine naphthyl. We have varied the length of the flexible spacer from n=2-6, 8, 10, and 12 to study its effect on the LC properties of the resulting dimers. By systematically varying the structure of the dimers and characterizing their liquid crystalline behaviour, we aim to gain insights into the role of naphthalene moieties as mesogenic cores and understand how different spacer lengths impact the LC properties of the dimers.

3.3. Results and Discussion

3.3.1 Synthesis

The synthesis of liquid crystalline dimers from series-***III-n*** and series-***IV-n*** was carried out following a standardized method outlined in **Scheme 3.1** and **Scheme 3.2**, respectively. The preparation of key intermediates including *(E)*-4-(naphthalen-2-yldiazenyl)phenol (NpAzOH) and *(E)*-4-((naphthalen-2-ylimino)methyl)phenol (NpAmOH) was given in detail in Chapter 2A, Section 2A.5.3. *(E)*-4-((4-hydroxyphenyl)diazenyl)benzonitrile (CNAzOH) was detailed in Section 3.5. CNAzOH underwent a reaction with excess α, ω-dibromoalkane in acetone in the presence of potassium carbonate (K_2CO_3) and a catalytic amount of potassium iodide (KI) to yield *(E)*-4-((4-(n-bromoalkoxy)phenyl)diazenyl)benzonitrile (CBr-n), where n is the number of carbons present in the flexible spacer. Subsequently, a Williamson ether reaction between CBr-n and NpAzOH/ NpAmOH in the presence of anhydrous potassium carbonate and potassium iodide in acetone led to the formation of ***III-n*** and ***IV-n*** (*n* = 2-6,8,10,12). The synthesis methodology remained consistent for each member of the series, with detailed synthesis and characterization data provided for individual compounds. (Section 3.5)

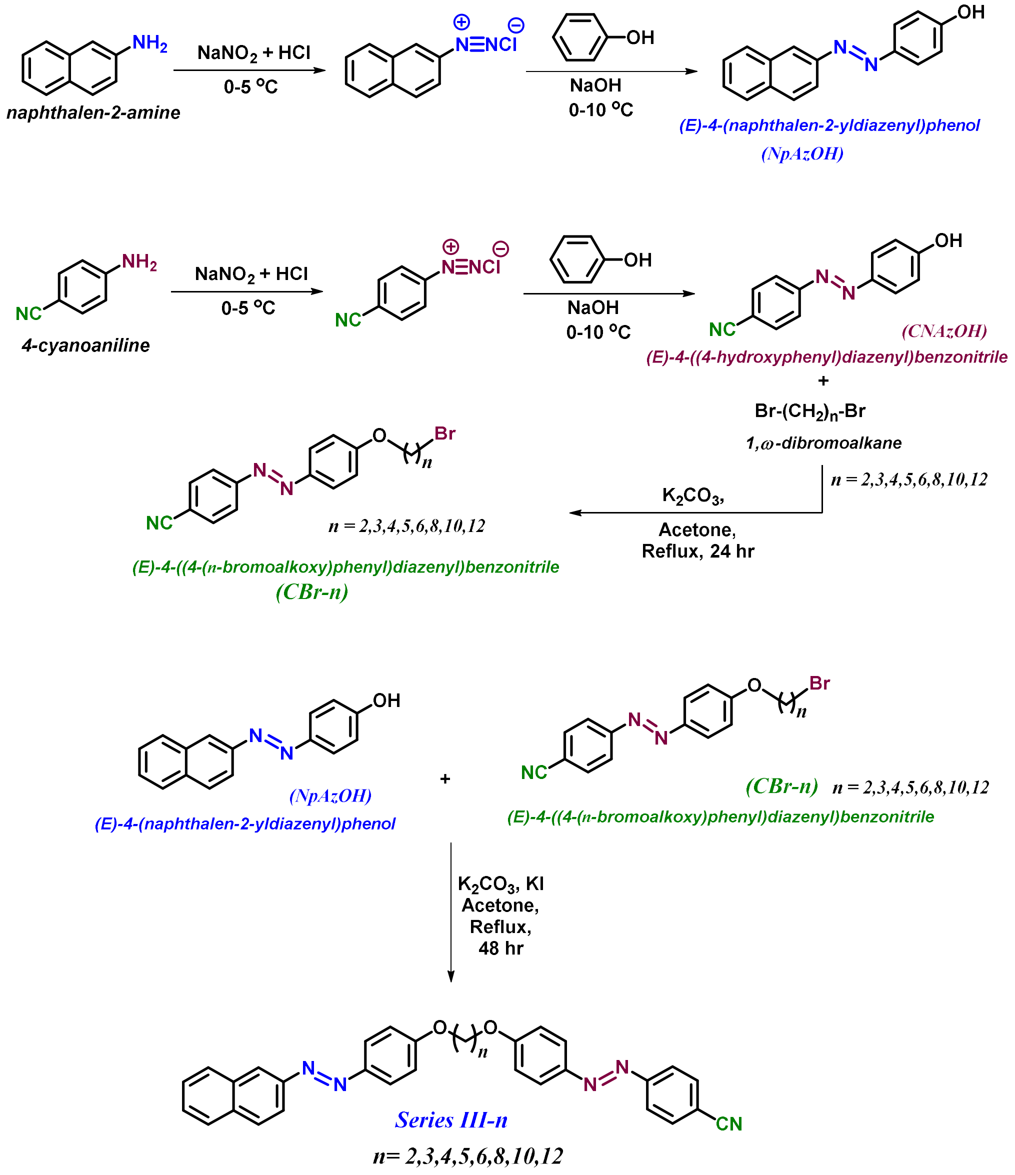

Scheme 3.1: Synthesis scheme for the dimers of series *III-n*

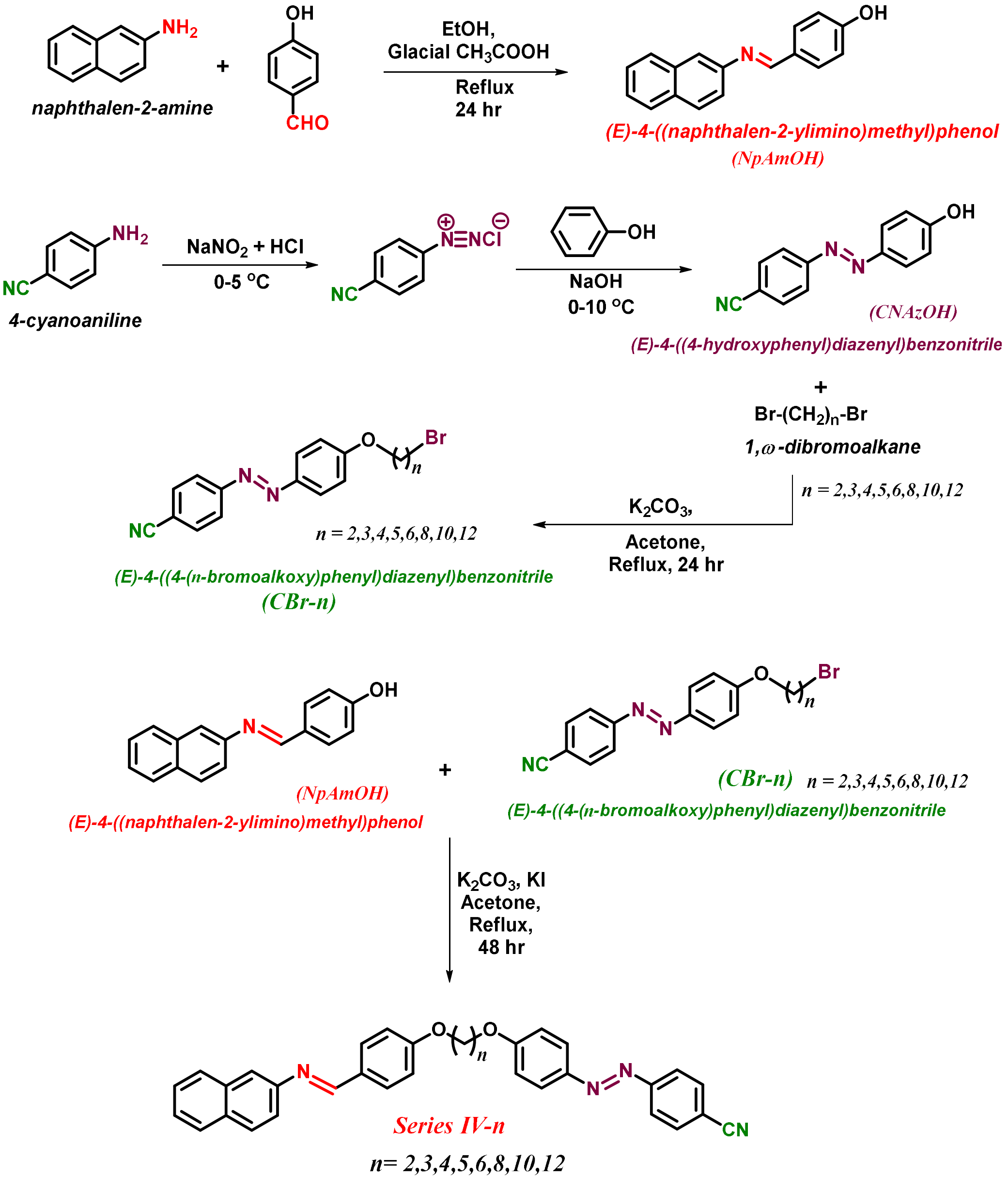

Scheme 3.2: Synthesis scheme for the dimers of series *IV-n*

3.3.2 Chemistry

Through the use of various analytical methods, including FT-IR, ^{1}H NMR, ^{13}C NMR and elemental analysis, the correct structures were verified. The structures of ***III-6*** and ***IV-6*** described in detail as representative of the series. FT-IR spectra of dimer ***III-6*** shows the C-H stretching bands for both alkyl and benzylic groups between 2800-3100 cm^{-1}. The medium intensity bands at the frequency range 1622–1602 cm^{-1} could be attributed to azo (-N=N-) group stretching. Similarly, the aromatic (-C=C-) stretching bands were observed at the frequency range of 1553–1507 cm^{-1}. Medium intensity band for the nitrile group (-C≡N) appeared around 2220-2228 cm^{-1}.

The ^{1}H NMR of ***III-6*** showed triplets for at δ 4.06-4.39 ppm for the protons on carbon which is attached to oxygen atom. The other methylene protons were observed as multiplet in between d 1.28–1.90 ppm. Aromatic protons were appeared in between δ 6.86-d 8.17 ppm. In the ^{13}C NMR of ***III-6***, signal for methylene protons of flexible spacer were observed around δ 25 to 30 ppm. For the carbon which is directly attached to oxygen signal was found around δ 69 ppm. All aromatic carbons were found around δ value of 110-165 ppm. The presence of the cyano group (-CN) is confirmed by the observation of a distinct peak at δ 121 ppm due to nitrile carbon. Dimers of ***Series IV-n*** has Imine linkage instead of azo linkage, so the rest structure is similar to that of **Series *III-n.*** So, the FT-IR spectra of ***IV-6*** showed the medium intensity bands at the frequency range 1622–1602 cm^{-1} which could be attributed to imine (-CH=N-) group stretching. The imine proton of Schiff base linkage was appeared as a singlet at δ 9.29 ppm. The imine carbon of –CH=N- linkage was observed at δ 163.71 ppm.

3.3.3 Mesomorphic Behaviour

The phase transition temperatures and mesomorphic behaviour of all the compounds were investigated using differential scanning calorimetry (DSC) while the textures of mesophase were observed using polarizing optical microscope (POM).

3.3.3.1 Differential scanning calorimetry study (DSC)

The thermograms were calculated utilising DSC During both heating and cooling cycles, all phase transitions of the compounds were monitored at a rate of 10 ºC min^{-1}. Transition temperatures (in °C) and associated enthalpy of transition (ΔH) in (kJ mol^{-1}) of dimers ***III-n*** are as presented in **Table 3.1** and dimers ***IV-n*** are as presented in **Table 3.2**. For all of the compounds, DSC curves and POM observations produced distinct transition temperatures and textures, and they exhibited good agreement throughout the numerous heating/cooling cycles.

Table 3.1: Transition temperatures (in °C) and associated enthalpy of transition (ΔH) in (kJ mol^{-1}) of *III-n*

Dimer *III*-n	n	Transition Temperatures (°C) and ΔH (kJmol^{-1})	
		Heating	Cooling
III-2	2	Cr 230.93 (44.11) N 283.23 (2.57) Iso	Iso 281.63 (-2.48) N 208.03 (-52.02) Cr
III-3	3	Cr 188.63 (52.96) N 201.43 (0.78) Iso	Iso 195.32 (-0.55) N 176.97 (-55.71) Cr
III-4	4	Cr 229.28 (88.62) N 270.10 (2.24) Iso	Iso 268.43 (-2.60) N 202.76 (-81.31) Cr
III-5	5	Cr 182.92 (24.56) N 195.31 (2.19) Iso	Iso 192.45 (-1.11) N 173.14 (-31.28) Cr
III-6	6	Cr 173.92 (44.44) N 239.05 (2.17) Iso	Iso 234.03 (-2.06) N 159.13 (-44.23) Cr
III-8	8	Cr 188.22 (68.25) N 227.38 (2.56) Iso	Iso 224.59 (-2.41) N 158.43 (-68.22) Cr
III-10	10	Cr 189.28 (5.88) N 198.57 (0.25) Iso	Iso 196.62 (-0.31) N 170.09 (-6.54) Cr
III-12	12	Cr 177.45 (12.23) N 186.49 (0.10) Iso	Iso 182.53 (-0.11) N 157.31 (-10.82) Cr

N, Nematic; Iso, Isotropic liquid; Cr, Crystalline solid

Table 3.2: Transition temperatures (in °C) and associated enthalpy of transition (ΔH) in (kJ mol^{-1}) of *IV-n*

Dimer *IV*-n	n	Transition Temperatures (°C) and ΔH (kJ mol^{-1})	
		Heating	Cooling
IV-2	2	Cr 197.88 (26.47) N 264.82 (2.69) Iso	Iso 263.78 (-2.76) N 134.81 (-23.71) Cr
IV-3	3	Cr 180.34 (43.54) N 195.79 (0.80) Iso	Iso 194.16 (-0.54) N 142.17 (-31.83) Cr
IV-4	4	Cr 190.36 (36.57) N 249.27 (3.45) Iso	Iso 248.76 (-2.74) N 124.81 (-25.03) Cr
IV-5	5	Cr 160.65 (34.18) N 191.67 (0.93) Iso	Iso 188.49 (-0.94) N 139.55 (-23.98) Cr
IV-6	6	Cr 159.80 (58.54) N 237.06 (2.82) Iso	Iso 233.73 (-3.04) N 123.74 (-57.23) Cr
IV-8	8	Cr 163.36 (38.74) N 219.39 (2.78) Iso	Iso 217.41 (-2.50) N 115.64 (-35.43) Cr
IV-10	10	Cr 158.87 (63.95) N 193.48 (2.53) Iso	Iso 191.38 (-2.90) N 141.93 (-54.14) Cr
IV-12	12	Cr 150.64 (68.72) N 186.14 (3.24) Iso	Iso 183.66 (-3.37) N 128.85 (-65.47) Cr

N, Nematic; Iso, Isotropic liquid; Cr, Crystalline solid

In order to determine the phase transition temperatures and enthalpy values, the DSC analysis of dimers of both the series ***III-n*** and ***IV-n*** were performed during heating and cooling cycles. Dimers ***III-n*** have shown two endothermic transitions (Cr-to-N and N-to-Iso) in heating cycle and two exothermic transitions (Iso-to-N and N-to-Cr) in cooling cycle.

The corresponding DSC thermogram for dimers ***III-6*** shown in **Fig. 3.3(a)**. Cr to N transition occurs at 173.92 °C with an associated enthalpy change (ΔH) of 44.44 kJ mol^{-1} and the subsequent transition to the isotropic liquid state occurs at 239.05 °C with ΔH of 2.17 kJ mol^{-1}. It's worth noting that a reversed phenomenon is observed during the cooling scan, indicating the reversibility of these transitions. Dimer ***III-6*** have shown two exothermic transitions (Iso-to-N and N-to-Cr) in cooling cycle at 234.02 °C and 159.13 °C respectively.

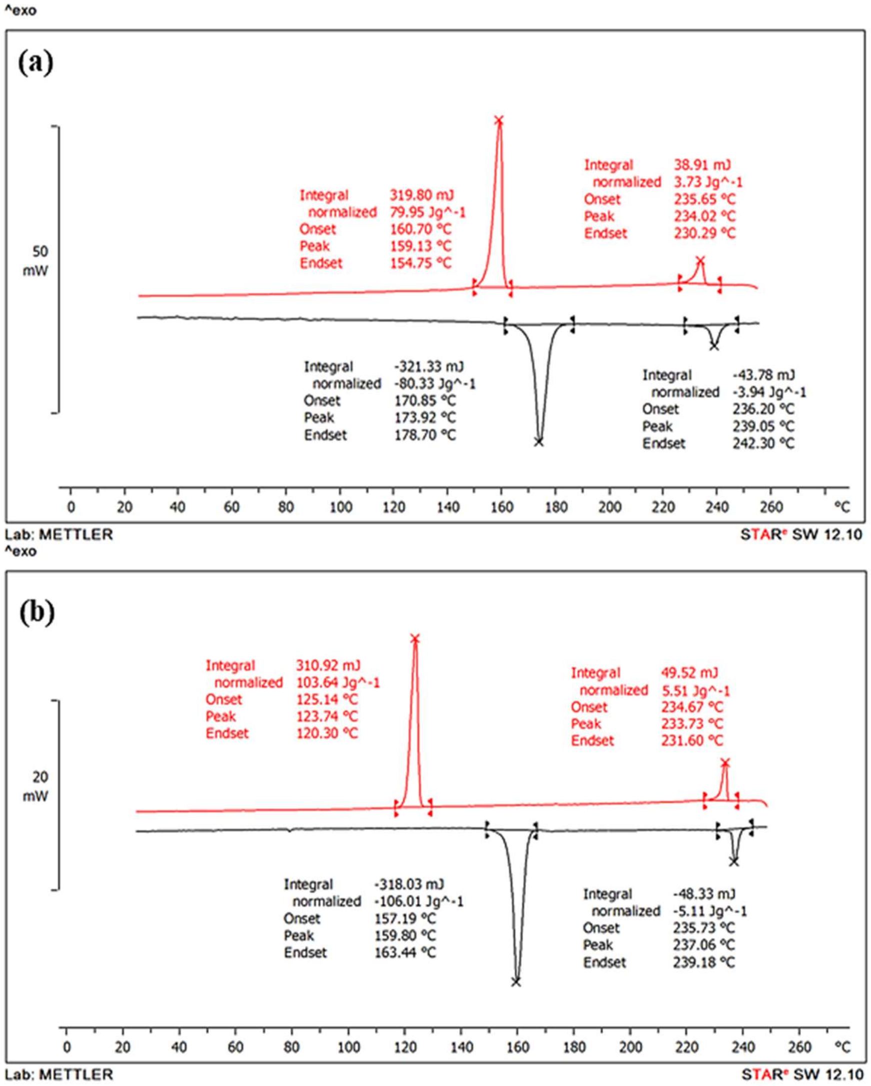

Fig. 3.3: DSC thermogram of Dimers (a) *III-6* and (b) *IV-6*

Dimers of ***Series IV-n*** also shows enantiotropic nematic (N) mesophase. ***IV-6*** shows endothermic transitions Cr-to-N and N-to-Iso at 159.8 °C (ΔH=58.54 kJ mol^{-1}) and 237.06 °C (ΔH=2.82 kJ mol^{-1}) on heating and on cooling, it shows two exothermic peaks at 233.73 °C (ΔH=3.04 kJ mol^{-1}) and 123.74 °C (ΔH=57.23 kJ mol^{-1}) for Iso-to-N and N-to-Cr transitions respectively (**Fig. 3.3b**). Furthermore, an interesting observation is that the mesophase range of the nematic phase decreases as the length of the flexible spacer is extended. This suggests a correlation between chain length and the stability of the nematic phase in the studied dimers.

3.3.3.2 Polarising optical microscopy (POM)

To ascertain the liquid crystalline properties of the dimers under investigation, compounds were carefully sandwiched between coverslips and observed under Polarized Optical Microscopy (POM). They were then heated to reach the isotropic state and subsequently subjected to a slow cooling process (i.e., 10 °C min^{-1}) from the isotropic state.

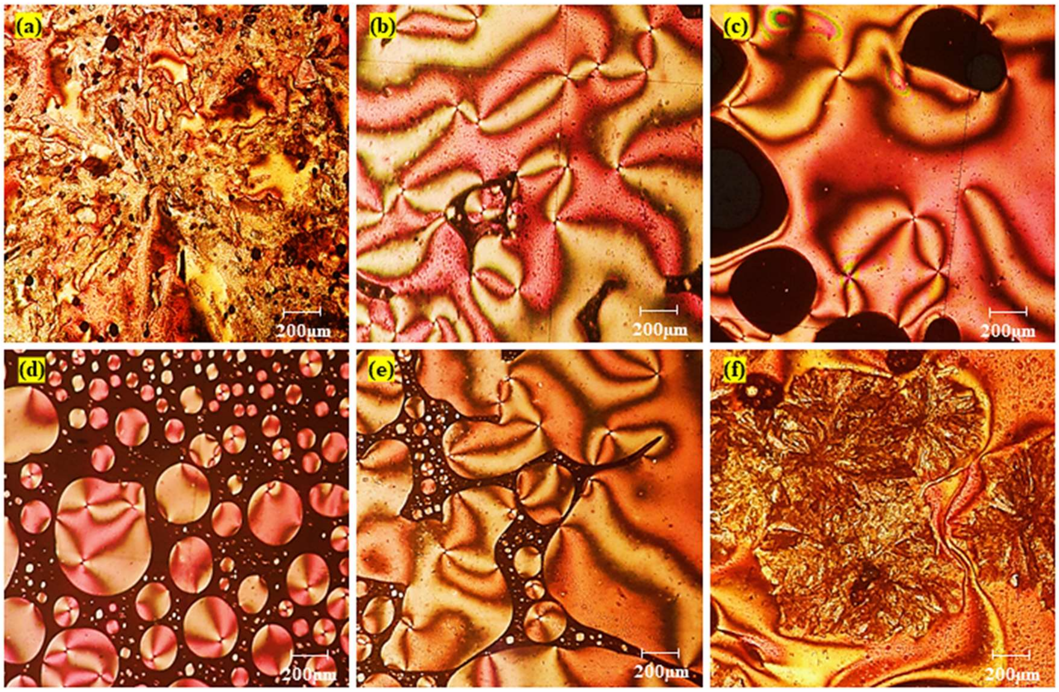

Fig. 3.4: Optical microphotographs of dimer *III-6* (a) Cr-N transition at 172 °C during heating, (b) Schlieren texture at 174 °C, (c) N-Iso transition at 239 °C, (d) Nematic droplets at 235 °C upon cooling, (e) Schlieren texture at 233 °C, (f) N-Cr transition at 160 °C.

All the dimers of ***Series III-n*** and ***Series IV-n*** show enantiotropic nematic phase. **Fig. 3.4** displays optical microphotograph of the nematic phase for dimer ***III-6*** during the first cooling and second heating cycle. **Fig. 3.4(a)** depicts the crystalline to nematic phase transition at 170°C during the heating cycle. This transition leads to the characteristic nematic phase observed as a schlieren texture in **Fig. 3.4(b)** at 174°C. Upon further heating, the nematic phase transitions into an isotropic liquid at 239°C **(Fig. 3.4(c))**. During the cooling cycle, nematic droplets first appear at 235°C **(Fig. 3.4(d))**, which then coalesce, forming the schlieren texture at 233°C **(Fig. 3.4(e))**. Subsequently, as the temperature continues to drop, crystallization initiates at 160°C **(Fig. 3.4(f))**.

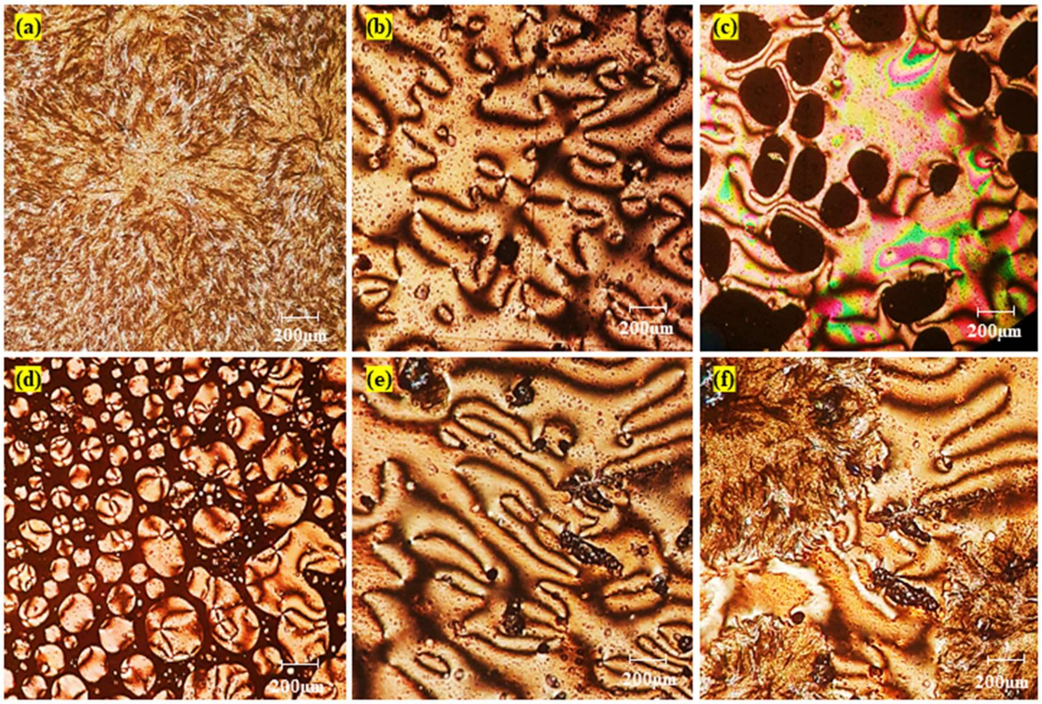

Fig. 3.5: Optical microphotographs of dimer *IV-6* (a) Crystalline state at 156 °C during heating, (b) Schlieren texture at 160 °C, (c) N-Iso transition at 237 °C, (d) Nematic droplets at 234 °C upon cooling, (e) Schlieren texture at 233 °C, (f) N-Cr transition at 125 °C.

Dimers from ***Series IV-n*** exhibit distinct nematic mesophase textures during both heating and cooling cycles. **Fig. 3.5** displays POM images of the nematic phase and schlieren textures of these ***IV-n*** dimers, showcasing a trend similar to that observed in series. Notably, the mesophase range for ***IV-6*** is more than that of ***III-6***.

3.3.3.3 Structure-property relationship

The structure-property relationship in the two series of dimers, namely ***III-n*** and ***IV-n***, is notably influenced by the length of the flexible spacer, particularly concerning the transition temperatures associated with the Nematic-to-Isotropic (N-Iso) phase transition. In both series, an intriguing odd-even effect becomes evident. The plot in **Fig. 3.6** and **3.7** further demonstrates how the transition temperatures correlate with the no. of carbons (n) in flexible spacer.

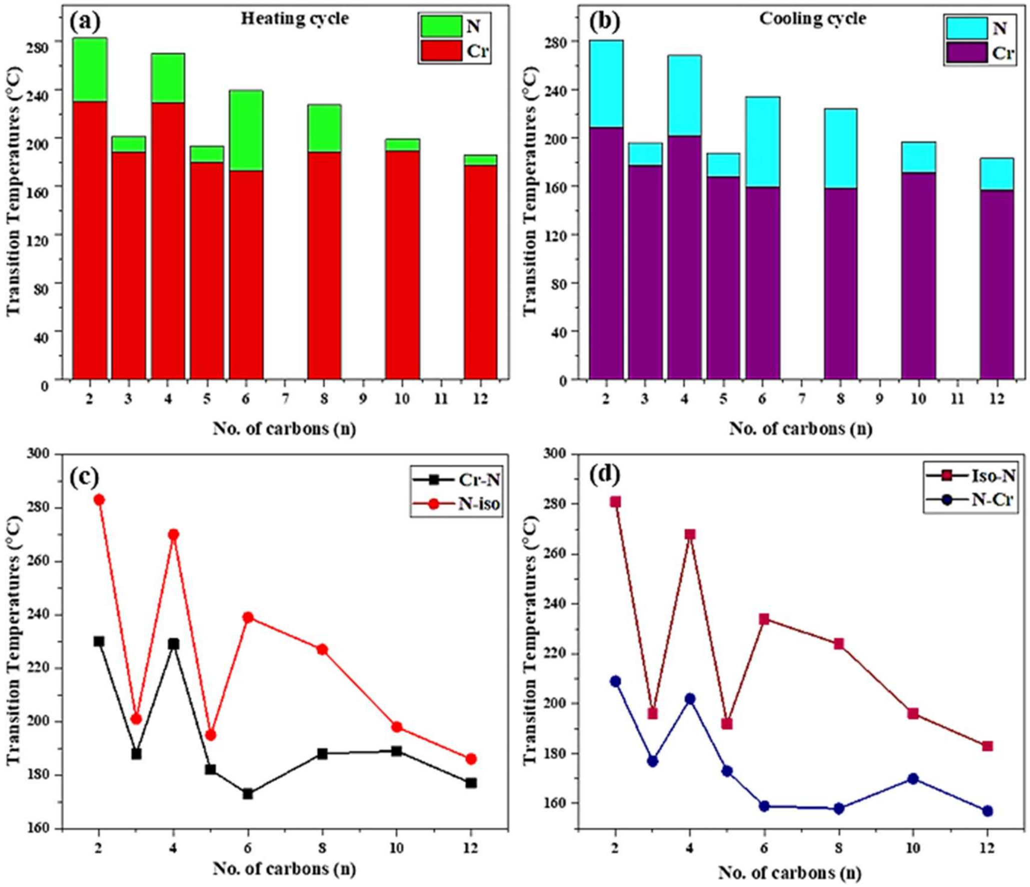

Fig. 3.6: (a and b) Bar graphs depicting mesophase stability (c and d) Line graphs illustrating transition temperatures in heating and cooling cycle for *III-n*

In the ***III-n*** series, it is observed that as the number of carbons in the flexible spacer increases, the transition temperatures for the N-Iso phase transition decrease. This implies that longer flexible spacers tend to stabilize the nematic phase at lower temperatures. However, what's particularly noteworthy is the clear odd-even effect in this series. The odd-numbered dimers, specifically ***III-3*** and ***III-5***, exhibit lower transition temperatures when compared to the other dimers within the series. This effect suggests that the presence of an odd number of carbon atoms in the spacer enhances the propensity for a lower N-Iso transition temperature in these dimers. Similarly, in the IV-n series, a similar trend is observed. Longer flexible spacers lead to decreased transition temperatures, indicating increased nematic phase stability. Additionally, an evident odd-even effect is observed, with odd-numbered dimers (IV-3 and IV-5) displaying lower transition temperatures, highlighting the influence of an odd number of carbon atoms in the spacer on the N-Iso transition temperature.

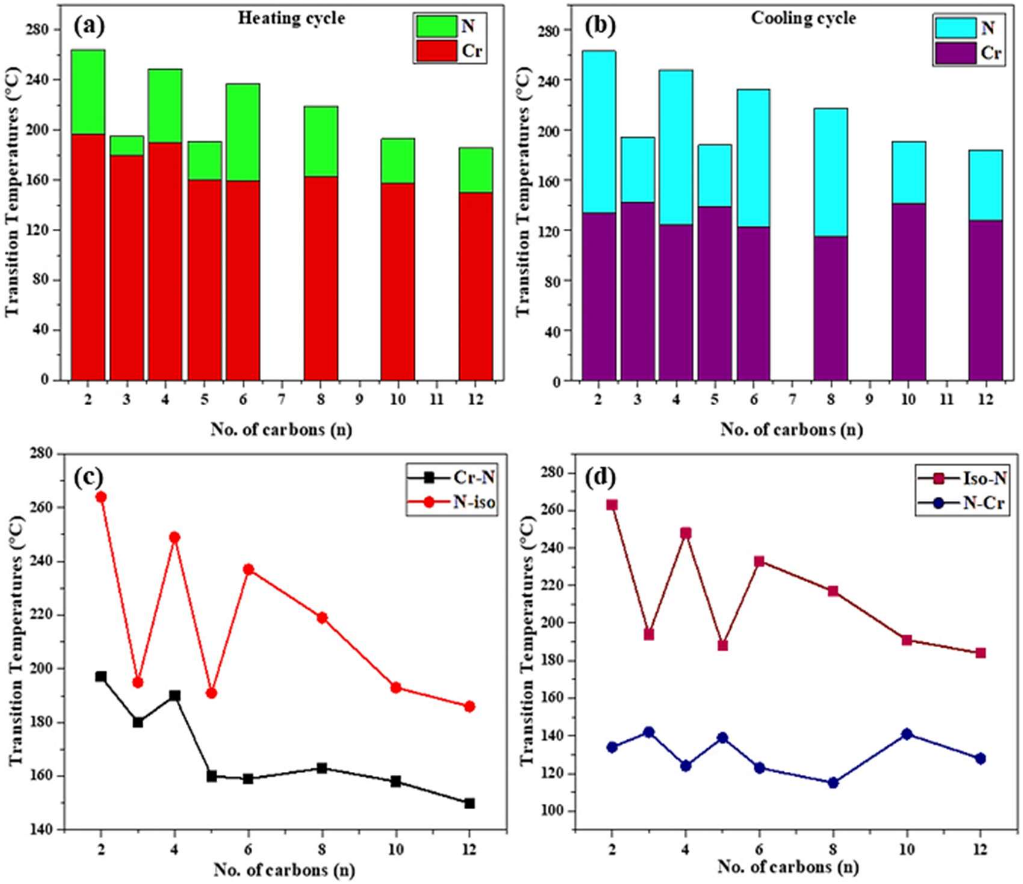

Fig. 3.7: (a and b) Bar graphs depicting mesophase stability (c and d) Line graphs illustrating transition temperatures in heating and cooling cycle for *IV-n*

Fig. 3.6 and **3.7** highlight that ***III-n*** dimers exhibit higher thermal stability than ***IV-n*** dimers, with the N-Iso transition temperatures in the ***III-n*** series are higher than those in the ***IV-n*** series. Additionally, both illustrate that the mesophase stability of the dimers is more pronounced during the cooling cycle compared to the heating cycle.

Fig. 3.8 is showing the graph of total transition stability versus the no. of carbons present in flexible spacer for both series. From this we can conclude that, the Dimers of ***Series IV-n*** have higher mesophase stability/ nematic mesophase length compared to that of dimers of ***Series III-n***. These results can be attributed to the fact that, azomethine linkages can provide more stability to mesophase, whereas azo linkages are stronger so that have higher thermal stability ($T_{N\text{-}Iso}$ transition temperatures).

Fig. 3.8: Bar graph showing mesophase stability of dimers in heating cycle for *Series III-n* and *IV-n*

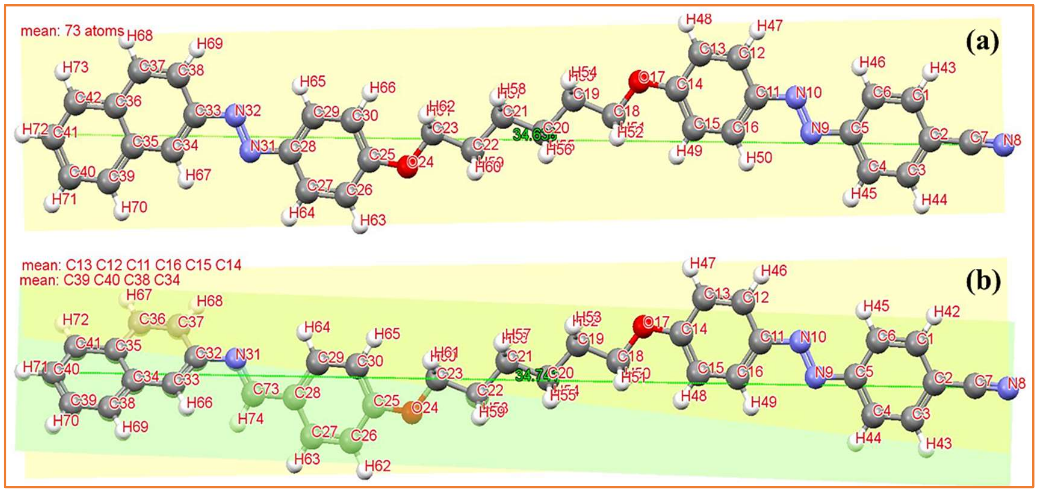

Fig. 3.9: Geometrical difference between the structure for (a) *III-6* and (b) *IV-6* shown by its planar structure

The differences in transition temperatures between ***Series III-n*** and ***IV-n*** can be attributed to the structural characteristics of the azo and azomethine linkages in the dimers. In ***Series III-n***, the presence of the central –N=N– linkage results in a more coplanar arrangement of the molecular structure. This coplanarity allows for more efficient packing of the molecules, leading to slightly higher thermal stabilities. The molecules in ***Series III-n*** can organize themselves more closely due to this planar arrangement. In contrast, ***Series IV-n*** contains the central –CH=N– linkage, which is less coplanar. This non-coplanar configuration hinders the efficient packing of molecules, resulting in lower thermal stabilities compared to ***Series III-n***. Furthermore, the thermal stability of a mesophase is a crucial factor when considering mesomorphic behaviour in relation to chemical constitution. The temperature range of a mesophase is influenced, in part, by the unpredictable nature of the crystal-to-mesophase transition temperature. In **Fig. 3.9**, it is evident that in ***Series IV-n*** (***IV-6***), the naphthalene ring is slightly tilted and lies in different planes. This structural feature reduces the packing efficiency of the molecules. As a result, the non-coplanar arrangement of the naphthalene ring in ***IV-6***, contributes to its low transition temperatures relative to the more coplanar molecules of ***Series III-n***.

The observed small enthalpies for even-membered dimers are in line with findings reported in previous research on pyrene-based dimers. This similarity suggests a common underlying mechanism, which we attribute to the enhanced biaxiality of the mesogenic units within our naphthalene-based dimers. The relatively high biaxiality associated with the naphthalene-based units likely contributes to the observed low enthalpy values. This behaviour aligns with the trends observed in pyrene-based materials, underscoring the importance of molecular structure and biaxiality in governing the thermotropic properties of liquid crystal dimers.[23–25]

Table 3.3 presents an outline of transition temperatures (in °C) and comparative geometry data, contrasting the ***III-n*** series with a closely related series with comparable structures. The dimers in series ***III-n*** show enantiotropic mesogenic behaviour, in contrast to series A, where only two members exhibit enantiotropic mesophase behaviour. Compared to series A, the dimers in our current series display greater thermal and mesophase stability. The primary distinction between series A and series III-n is the composition of their aromatic cores at one end: series III-n includes azonaphthalene moiety, whereas series A contains a biphenyl ring. This difference results in an elongated molecular structure and increased polarizability, which together contribute to the improved thermal and mesophase stability observed in our current series.

Table: 3.3 Comparison of transition temperatures (°C) of present series *III-n* and structurally related series A[26]

No. of C in chain (n)	Series A (BpnCN)		Series *III-n*	
	Transition Temperatures (°C)			
	$T_{Cr\text{-}N/Iso}$	$T_{N\text{-}Iso}$	$T_{Cr\text{-}N}$	$T_{N\text{-}Iso}$
2	217	-	230	283
3	218	-	188	201
4	190	208	229	270
5	169	-	182	195
6	154	183	173	239

N, Nematic; Iso, Isotropic liquid; Cr, Crystalline solid; (-) *Transition not exist.*

3.3.4 Thermogravimetric analysis (TGA)

Dimers ***III-6*** and ***IV-6*** were subjected to TGA measurements in a nitrogen atmosphere at temperatures ranging from 25 to 550 °C. **Fig. 3.10** presents the TG curve for dimer ***III-6*** and ***IV-6***. There is minimal mass loss up to 400 °C for ***III-6*** and 300 °C for ***IV-6.*** Steady loss of mass after that, which may be attributed to the thermal decomposition. Both the dimers are fairly stable at higher temperatures.

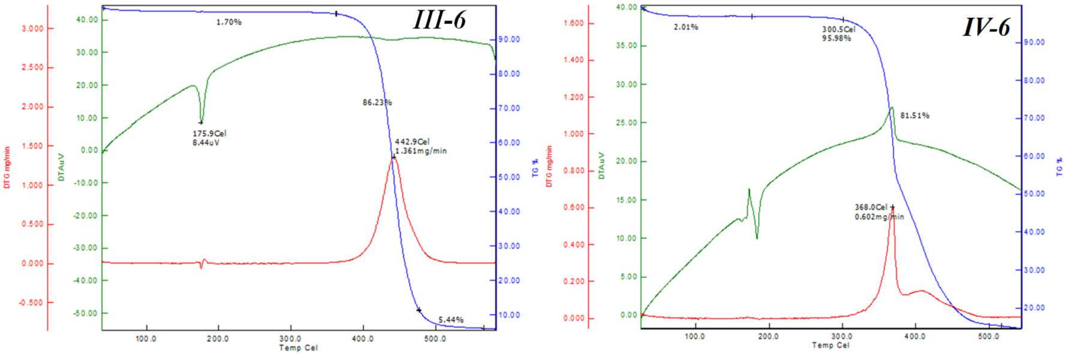

Fig. 3.10: TGA plot for *III-6* and *IV-6*

3.3.5. Computational studies

Density Functional Theory (DFT) was employed using Becke's three-parameter hybrid functional (B3LYP) at the 6-31 G basis set level[27]. DFT theoretical calculations are required to comprehend the molecular approaches, predicted optimized structures, and vibrational frequencies The theoretical calculations for the proposed compounds were carried out by Gaussian 09 software. We optimized the energy of conformations until they found a minimum-energy geometrical structure and then used that structure to calculate frequencies and thermodynamic properties. In order to depict molecular structures, carbon, nitrogen, oxygen, and hydrogen atoms are colour-coded as follows: grey for carbon, blue for nitrogen, red for oxygen, and white for hydrogen. Sigma and pi bonds are utilized to connect these atoms, forming the three-dimensional arrangement of the molecules. **Fig. 3.11** showcases the optimized molecular structures for dimers in both series.

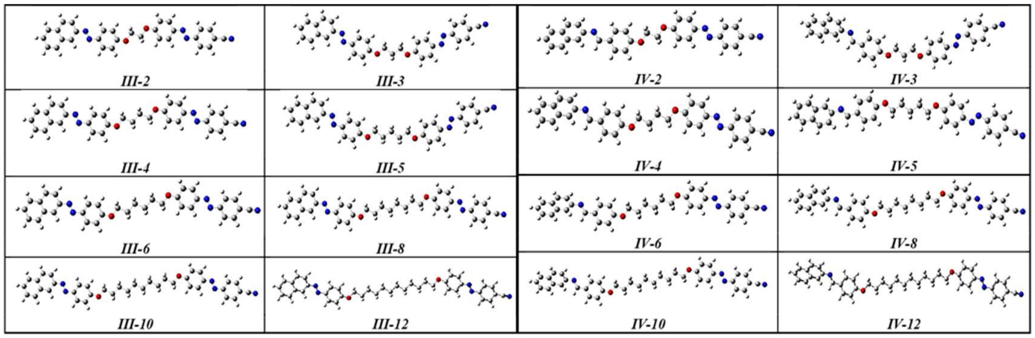

Fig. 3.11: Optimized molecular structures of dimers of *Series III-n* and *IV-n*

Table 3.4 presents the stabilization energy or energy minima values (in Hartree) for each dimer. The energy minima decreases as the number of carbons in the flexible spacer chain of the dimers increases. The comparison of the interaction energy between the two series reveals that the members of ***Series III-n*** exhibit greater energetic stability compared to the dimers of ***Series IV-n***.

Table 3.4: Quantum mechanical descriptors

Dimer	*Energy minima (Hartree)*	*HOMO*	*LUMO*	*I* (eV)	*A* (eV)	*ΔE* (eV)	*η*	*δ*	*χ*	*ω*
				Series III-n						
III-2	-1619.298	-0.210	-0.099	5.703	2.684	3.019	1.510	0.662	4.193	5.824
III-3	-1658.616	-0.208	-0.098	5.668	2.662	3.006	1.503	0.665	4.165	5.771
III-4	-1697.934	-0.207	-0.097	5.632	2.636	2.997	1.498	0.667	4.134	5.703
III-5	-1737.253	-0.207	-0.096	5.629	2.605	3.024	1.512	0.661	4.117	5.605
III-6	-1776.568	-0.205	-0.096	5.591	2.609	2.982	1.491	0.671	4.100	5.637
III-8	-1855.201	-0.204	-0.095	5.565	2.593	2.972	1.486	0.673	4.079	5.597
III-10	-1933.834	-0.204	-0.095	5.548	2.583	2.965	1.483	0.674	4.065	5.573
III-12	-2012.467	-0.203	-0.095	5.537	2.576	2.961	1.480	0.675	4.057	5.558
				Series IV-n						
IV-2	-1603.291	-0.205	-0.099	5.576	2.690	2.886	1.443	0.693	4.133	5.920
IV-3	-1642.600	-0.204	-0.098	5.551	2.666	2.885	1.442	0.693	4.108	5.851
IV-4	-1681.927	-0.203	-0.097	5.522	2.640	2.882	1.441	0.694	4.081	5.780
IV-5	-1721.244	-0.200	-0.096	5.446	2.611	2.835	1.417	0.705	4.029	5.726
IV-6	-1760.560	-0.202	-0.096	5.489	2.612	2.877	1.438	0.695	4.050	5.703
IV-8	-1839.194	-0.201	-0.095	5.468	2.595	2.872	1.436	0.696	4.032	5.659
IV-10	-1917.827	-0.200	-0.095	5.454	2.585	2.869	1.434	0.697	4.019	5.631
IV-12	-1996.460	-0.201	-0.095	5.468	2.578	2.890	1.445	0.692	4.023	5.600

I, Ionization Potential; *A*, Electron Affinity; *ΔE*, Energy gap; *η*, Global hardness; *δ*, Global softness; *χ*, Chemical reactivity; *ω*, Electrophilicity index

3.3.5.1. Frontier molecular orbitals (FMOs) and Molecular electrostatic potential (MEP)

The electronic properties such as HOMO (Highest Occupied Molecular Orbital) and LUMO (Lowest Unoccupied Molecular Orbital) energy levels, were calculated for the optimised geometries. The frontier molecular orbitals (FMOs) were analysed to predict the chemical reactivity and stability of the compounds[28]. The HOMO–LUMO energy gap was calculated to determine the potential for electron transfer in the compounds[29]. In ***Series III-n***, the HOMO is primarily constituted by the π-orbitals originating from the naphthyl ring, with a minor contribution from the azo linker (-N=N-) (**Fig. 3.12**). The LUMO is associated with the corresponding anti-bonding orbital of the connected phenyl ring bearing a cyano substituent. In ***Series IV-n*** dimers, the HOMO is mainly localized by the π-orbitals of the naphthyl unit, with a smaller contribution from the π-orbitals of the -CH=N- linker. The LUMO is associated with the corresponding anti-bonding orbital of the phenyl ring containing a cyano substituent. Notably, there is a slight disparity in the HOMO-LUMO energy values, with ***Series III-n*** dimers exhibiting marginally higher values than those of ***Series IV-n***. Additionally, it is worth mentioning that the length of the flexible spacer has no observable impact on the spatial distribution of electron densities within the Molecular Orbitals (MOs).

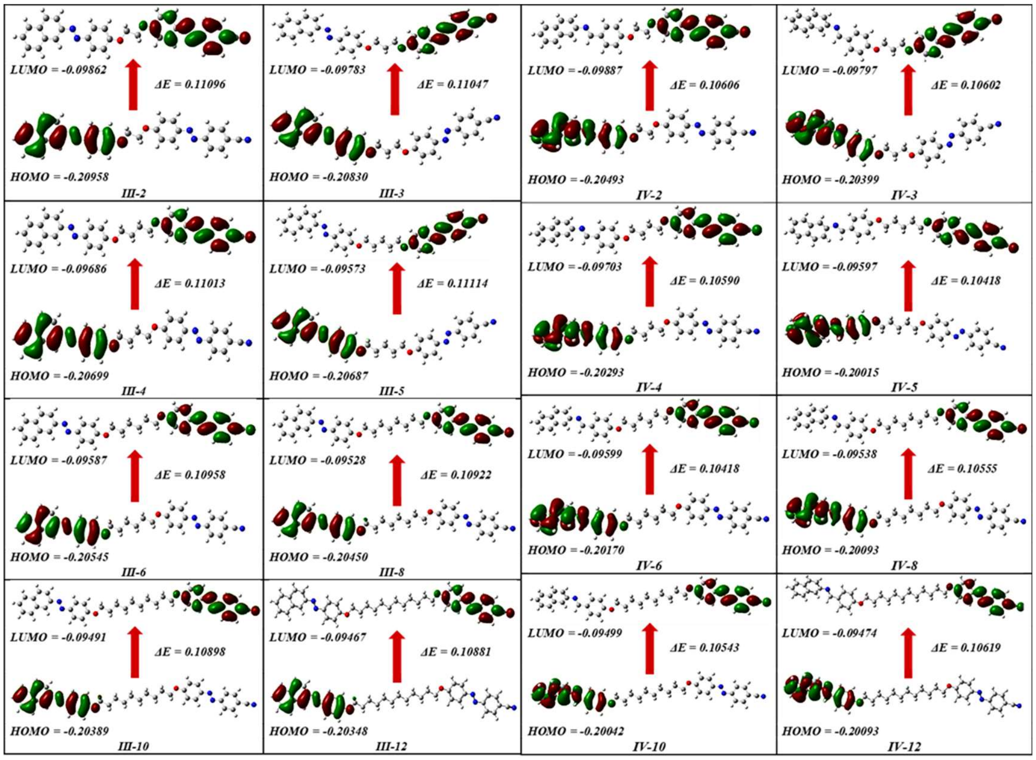

Fig. 3.12: FMOs for the dimers of *Series III-n* and *IV-n* (Values of HOMO, LUMO and ΔE are in a.u.)

Interestingly, when we increase the length of the flexible spacer, this does not lead to a significant alteration in the energy gap, as evidenced in **Table 3.4**. This stability in the energy gap can be attributed to the high concentration of charge density situated around the cores of the dimers, as visually represented in **Fig. 3.12.** Furthermore, it is worth noting that there is no substantial variation in the HOMO energy, which remains consistently around ~-0.20 a.u., and the LUMO energy, which remains around ~-0.09 a.u., across all dimers. This consistent behaviour indicates the system's stability even when modifying the length of the flexible spacer. Remarkably, the studied dimers exhibited nearly identical values for parameters, including chemical hardness (η) and softness (δ), which remained consistent across the varying lengths of the flexible spacer chains in the dimers.

Typically, molecular-molecular interactions play a crucial role in shaping the mesophase behaviour of calamitic dimers. This behaviour predominantly hinges on the molecular geometry, polarizability (α), dipole moment (μ), and the electronic characteristics of the entire molecule [30].

Table 3.5: Optical properties and dimensional parameters of the dimers

Dimer	***Dipole Moment μ (debye)***	***Polarizability (α) (a.u.)***	***Length (L) Å***	***Width (D) Å***	***Aspect ratio (L/D)***	***Mesophase range (ΔT) °C***
			Series III-n			
III-2	6.248	496.889	29.662	5.568	5.327	52.30
III-3	6.324	505.812	29.962	7.640	3.921	12.80
III-4	6.196	518.762	32.142	5.907	5.441	40.81
III-5	6.219	528.761	32.498	7.646	4.250	12.39
III-6	6.163	540.732	34.638	6.339	5.464	65.13
III-8	6.143	563.030	36.201	6.525	5.548	39.16
III-10	6.130	585.490	38.743	6.659	5.818	9.29
III-12	6.121	608.057	41.287	6.754	6.112	9.04
			Series IV-n			
IV-2	5.4241	480.323	29.778	5.565	5.350	66.94
IV-3	5.6641	489.551	29.967	7.603	3.941	15.45
IV-4	5.4259	502.468	32.243	6.007	5.367	58.91
IV-5	5.5665	513.205	33.596	7.712	4.356	31.02
IV-6	5.4194	524.598	34.753	6.321	5.498	77.26
IV-8	5.4127	546.978	37.232	6.547	5.686	56.03
IV-10	5.4077	569.490	39.708	6.708	5.919	34.61
IV-12	5.4040	592.122	42.211	6.823	6.186	35.50

For each individual molecule within these compounds, the dipole moment value consistently falls within a range of approximately 5.4 to 6.3 Debye. (**Table 3.5**) Typically, molecular-molecular interactions are recognized for their substantial influence on dipole moments. Notably, odd-membered dimers exhibit higher dipole moments in comparison to even-membered dimers. This phenomenon could account for the lower clearing temperatures and reduced mesophase length observed in these dimers. It's important to note that this trend is consistent across both series.

Table 3.5 presents the polarizability values for each member in both ***Series III-n*** and ***Series IV-n***. Furthermore, it is evident that the length of the flexible spacer exerts an influence on the stability of members in both series. A notable and highly significant correlation is observed between the polarizability and the length of the flexible spacer in both Series. Specifically, the polarizability increases in direct proportion to the chain length

The dramatic odd-even effects observed in the transitional properties of dimers arise from the dependence on the molecular shape dictated by the number of atoms linking the mesogenic units. Specifically, even-membered dimers exhibit a linear shape, while odd-membered dimers adopt a bent shape. (**Fig. 3.13**) This structural difference influences the compatibility with the molecular organization found in the nematic phase, leading to distinct transitional behaviours such as alternation in nematic-isotropic transition temperatures and melting points.[1,31]

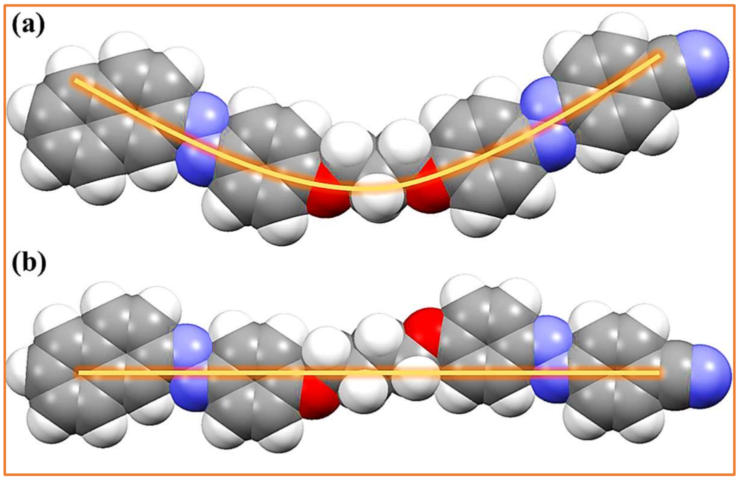

Fig. 3.13: Space-filling model of (a) *III-3* (Odd membered dimer) and (b) *III-4* (even membered), showcasing the spacer in the all-trans conformation.

The molecular electrostatic potential (MEP) surface was also generated to visualise the electron density distribution and predict the sites of electrophilic and nucleophilic attacks[32]. Furthermore, the formation of mesophases in these compounds is influenced by the packing arrangement of the molecules, which is likely influenced by the distribution of charges within the compounds. In this study, the distribution of charges within the compounds was determined using the DFT/B3LYP method with a 6-31G basis set. The visual representation of the MEP surface, as depicted in **Fig. 3.14**, plays a pivotal role in comprehending these interactions[33].

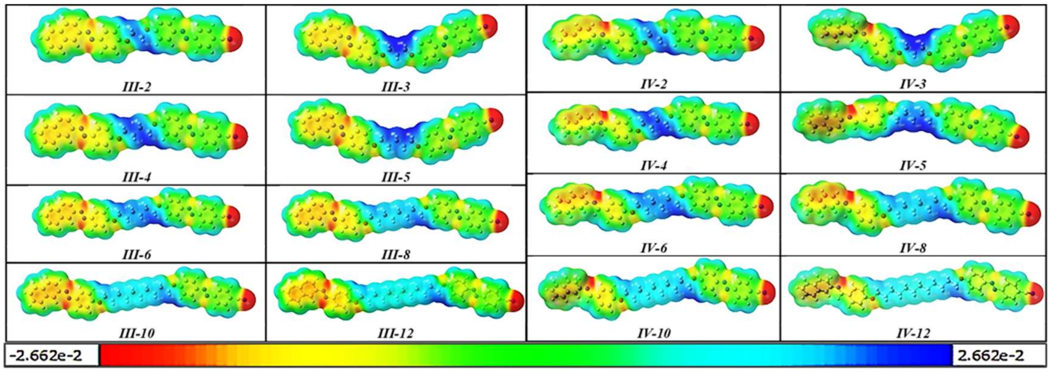

Fig. 3.14: MEP contours of the dimers of *Series III-n* and *IV-n*

Electrophiles typically target areas with a higher negative charge, shown in red, while nucleophiles prefer regions with less negative charge, indicated in blue. Red regions are primarily concentrated around the Cyano group and nitrogen atoms of azo groups, while blue regions are commonly found along the carbon chain of the flexible spacer. The separation of charges in the dimers leads to end-to-end interactions, resulting in the formation of a nematic mesophase characterized by limited lateral ordering.

3.3.5.2 Vibrational studies

The calculated vibrational frequencies of the compounds were compared with the experimental values obtained from FT-IR spectra. The theoretical frequencies showed good agreement with the experimental values, confirming the accuracy of the DFT calculations. The obtained geometries were further confirmed by the vibrational frequency analysis, which yielded no imaginary frequency. **Fig. 3.15** depicts the plot which shows the comparison of the vibrational frequency obtained from the experiment and calculated at B3LYP-6-31G level theory for dimers ***III-6*** and ***IV-6***.

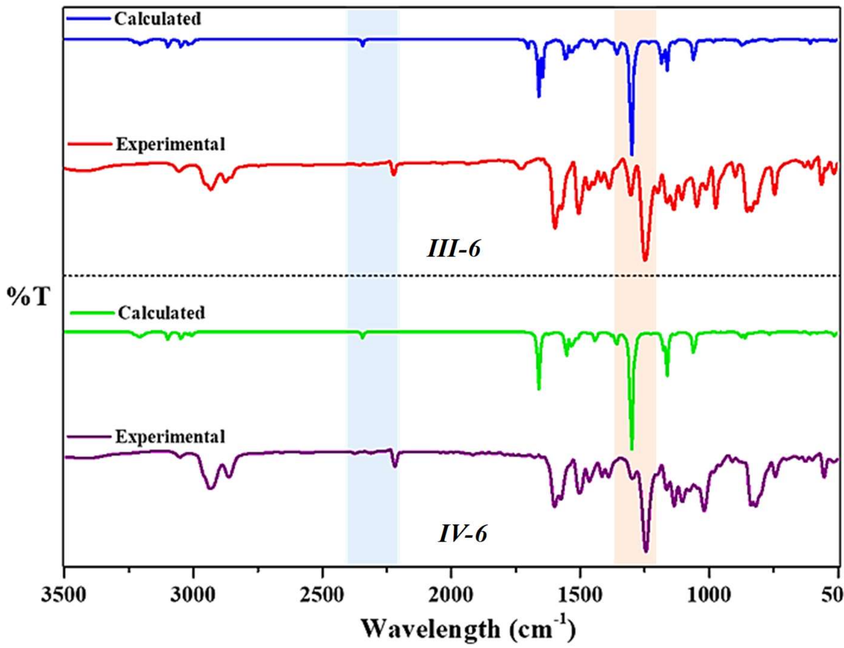

Fig. 3.15: Comparison of the vibrational frequency obtained from the experiment and calculated at B3LYP-6-31G level theory (gas phase) for dimers *III-6* and *IV-6*

The vibrational modes of phenyl rings and naphthalene rings include C-H stretching vibrations (3000-2800 cm^{-1}), out-of-plane and in-plane C-H bending vibrations (850-700 cm^{-1}), and -C=C- stretching vibrations (1570-1500 cm^{-1}), with good agreement between theoretical and experimental values. C-C stretching vibrations are observed between 1450-1300 cm^{-1}, while in-plane C-C bending vibrations occur around at 1010-1030 cm^{-1}. C-N vibrations at 1600 cm^{-1} indicate a -N=N- double bond. -CH=N- vibrations (imine groups) are seen at 1600 cm^{-1}. The cyano group (nitrile) exhibits C-N stretching vibrations at 2220 cm^{-1}. Ether groups display C-O stretching vibrations (1260-1200 cm^{-1}) and O-C-O bending vibrations (720-640 cm^{-1}) in line with theoretical calculations.

3.3.6. Photochromic behaviour

Compounds containing azo linkage are considered dynamic because they exhibit photoisomerization, mainly through the π-π* transition. This process allows the molecule to switch between *cis* and *trans* isomeric forms when exposed to light. This unique property makes azo compounds an attractive choice for the creation of light-responsive materials.[34–38] A dual beam spectrophotometer equipped with a 1 cm quartz cuvette and a 365 nm filter was used to measure photoisomerization in ***III-6***. **Fig. 3.16** shows the photoisomerization in ***III-6***.

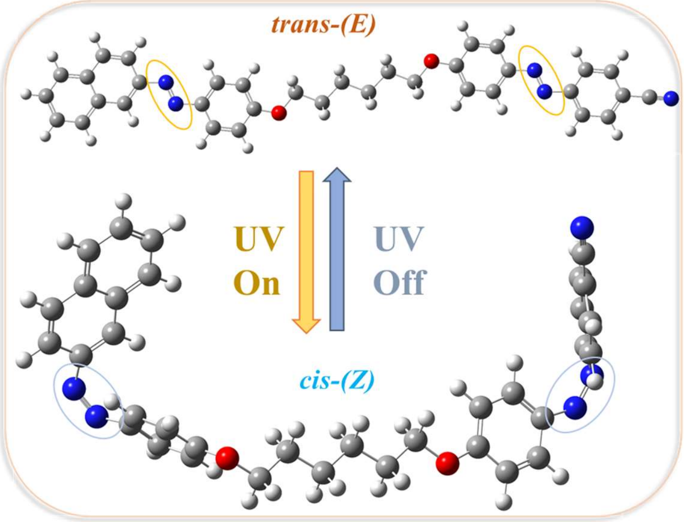

Fig. 3.16: Photoisomerization in *III-6*

In **Fig. 3.17(a),** UV-Vis spectra of ***III-6*** under varying UV exposure times reveal *trans* (E)-*cis (Z)* isomerization, evident by a decrease in the π-π* transition at 365 nm and an increase in the n-π* transition at 440 nm. The system reaches a photo stationary state within 3.5 minutes due to steric hindrance favouring *cis-to-trans* reversion. For the thermal back relaxation process (**Fig. 3.17(b)**), ***III-6*** was left in the dark, and absorbance was monitored until it fully transformed into the stable trans form. This spontaneous process, driven by energy release from the cis form, shows an increase in absorption maxima followed by a slight decrease at longer wavelengths, confirming no side reactions with two isosbestic points. Full trans configuration stability is restored after approximately 4.5 hours.

TD-DFT technique with the B3LYP functional and 6-31G(d,p) basis set in Gaussian 09 were utilized for theoretical calculations, incorporating an implicit solvent model for chloroform for dimer ***III-6***. We observed a prominent π-π* transition, characterized by the excitation of an electron from a π bonding orbital (HOMO) to a π* antibonding orbital (LUMO). This transition was evidenced by the absorption peak at 365 nm, corresponding to the HOMO-1 → LUMO transition. Additionally, the presence of a cyano group (-CN) in ***III-6*** induced an electron-withdrawing effect, resulting in a significant dipole moment. This led to a broad absorption peak at 440 nm, attributed to a n-π* transition. Here, the interaction between the lone pair on the nitrogen atom of the cyano group and the π* antibonding orbital contributed to the observed absorption, corresponding to the HOMO → LUMO transition. Furthermore, we determined the energy band gap of ***III-6*** from UV data using a Tauc plot (**Fig. 3.18**) for both cis and trans configurations. Our analysis revealed a close agreement between the experimental and calculated energy gap values, with the cis form exhibiting a comparatively lower energy gap than the trans form. This observation underscores the sensitivity of the energy gap to molecular conformation.

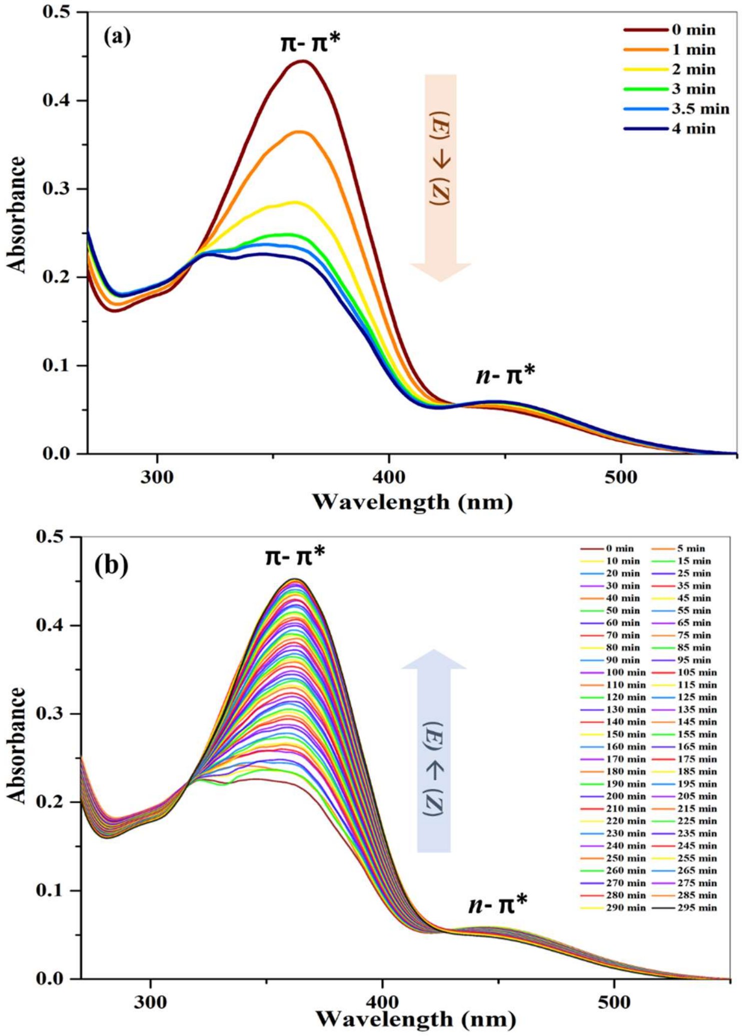

Fig. 3.17: Absorption spectra for *III-6* (a) with various UV exposure times. The UV illumination of 0 sec ~ No UV (b) Thermal back relaxation process

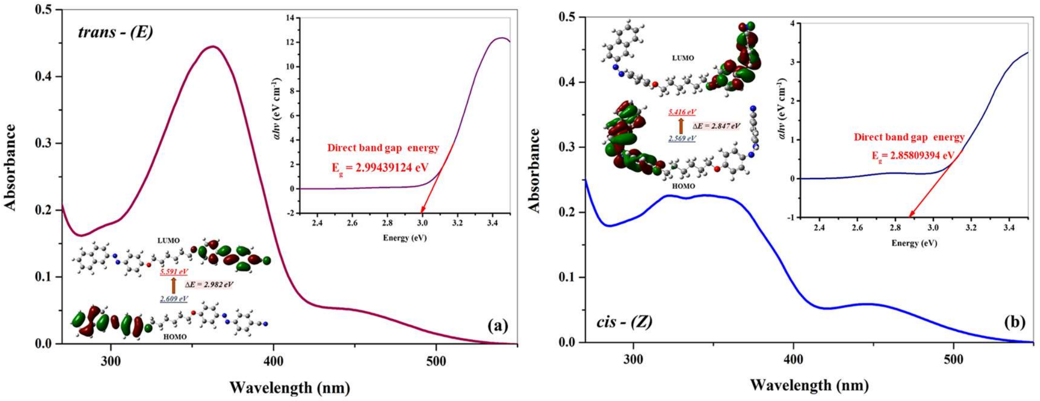

Fig. 3.18: Tauc plot for *III-6* showing a comparison between the experimental and calculated energy band gap for both (a) *trans* and (b) *cis* form

3.3.7 Thermal Photoisomerization studies of *III-6*

The photoinduced conformational changes in the liquid crystalline materials, which can self-assemble themselves find applications like self-healing materials[39], molecular electronics[40–43], photomechanical devices[44] etc. Hence thermo-photoisomerization, the process by which azobenzene molecules undergo isomerization in response to thermal and light stimuli, is pivotal for the development of responsive materials and devices. Understanding the mechanism of isomerization could lead to significant progress in creating new technologies such as molecular electronics, photovoltaics and pharmacology[45–47], surface science[48–50], optical data storage devices, and sensors. Despite the promising attributes of the cyanoazobenzene-naphthalene dimer, its potential applications, especially those exploiting its thermo-photoisomerization abilities, have not been thoroughly investigated. This study aims to fill that gap by exploring the physical applications of the novel azobenzene molecule through its thermo-photoisomerization behaviour. We propose that the unique properties of our synthesized molecule can be utilized to develop advanced materials with customized responsiveness to environmental stimuli.

The isomerization of azobenzene and its derivatives under different environmental conditions like electric and magnetic fields[51,52], heat[53] and light[54] is well studied. Earlier studies on the Langmuir monolayers of liquid crystalline azobenzene molecules have shown the effect of dipole moments in the molecules on their organization at the air-water interface[55–57]. The isomerization process can change the dipole moments in the molecule and the kinetics of isomerization can be affected by the local electrical fields[58]. On the other hand, the thermal isomerization rate constant depends on the polarity of the solvent used[59–61]. Regarding the kinetics of thermal-isomerization in azobenzene derivatives, several studies were conducted using Langmuir-Blodgett films[62]. In these studies, they found that the kinetic of isomerization was of first order. But earlier studies on azobenzene in polycarbonate thin film recorded a deviation from the first-order kinetics and attributed to free volume distribution on the reactivity[63]. At the air-water interface, the deviation from the first-order phase transition was studied by Bharat et. al and developed a kinetic model using a combination of first and second-order transitions[56]. Although the above studies show the switching of the molecules from trans to cis state and vice versa, there have been no studies to understand how the interactions between closely spaced dipole moments affect the molecular packing and change the surface free energy at the air-water interface.

3.3.7.1 Experimental setup

We have studied the Langmuir monolayer of the ***III-6*** using the surface manometry technique. Langmuir monolayers were formed by spreading 0.1 mg/ml solution of ***III-6*** molecules in the HPLC grade chloroform on the deionized water subphase. The resistivity of the deionised water was 18.2 MΩ.cm and the temperature of the subphase was maintained using a heated/chilled water circulator (make: Julabo). After spreading the ***III-6***/chloroform solution on the subphase, the chloroform evaporates and a stable monolayer form at the air-water interface. The monolayer was compressed between two moving barriers at a speed of 7 mm/min to obtain the π-A_m isotherms. To obtain the isotherm of ***III-6*** molecules in trans-state, the monolayer compression was done in the dark (the trough was enclosed in a dark chamber to avoid stray light). The isotherms of the ***III-6*** in the cis state were obtained by compressing the monolayer in the presence of the UV light of 365 nm. The kinetics of the photoisomerization was studied by compressing the trans-***III-6*** molecules to a target pressure of 20 mN/m and then shining it with a UV light at fixed barrier position corresponding to the target pressure. UV light source was placed 10 cm away from the air-water interface to maintain constant intensity for all the experiments. The surface pressure was monitored as a function of time after shining with UV light. Similarly, the kinetics of the thermal isomerization was studied by compressing the cis-***III-6*** monolayer to a target pressure and then switching off the UV light.

3.3.7.2 Results and Discussion of the study

The π-A_m isotherms and compression moduli of Langmuir monolayer of azobenzene derivative (***III-6***) with UV light and dark at 298 K is shown in **Fig. 3.19(a)**. The isotherm was reproducible for the solution concentration of 0.1 mg/ml. The phases exhibited by the monolayer are classified using compressibility modulus values (see **Fig. 3.19(b)**). In the dark chamber, the ***III-6*** molecules will be in the trans-state and the monolayer exhibited gaseous phase for a mean molecular area greater than 29 Å2. The monolayer exhibited a liquid expanded (LE) phase between 29 Å2 and 10.5 Å2 and it collapsed at 10.49 Å2 with a collapse pressure of 66.4 mNm^{-1}. The π-A_m isotherm of the monolayer in the presence of UV light (i.e., the ***III-6*** molecules are in the cis-state) shifted to a lower mean molecular area. It exhibited a gaseous phase for an area greater than 22 Å2 followed by LE phase between 22 Å2 and 20 Å2. The monolayer exhibited a co-existence of LE and ordered liquid condensed (LC) phase for the area between 20 Å2 and 18 Å2. Further compression led to the uniform ordered LC phase between 18 Å2 and 11 Å2. The monolayer collapsed at 11 Å2 with a collapse pressure of 59.3 mNm^{-1}. The decrease in the mean molecular area for the monolayer of ***III-6*** in the cis-state as compared to that of the trans-state may be attributed to the low molecular density and orientation of the cis-***III-6*** molecule.

The Brewster angle microscopy (BAM) images of the ***III-6*** monolayer without UV are shown in **Fig. 3.20**. There is no significant change in the BAM image when UV is shined on the monolayer compared to the monolayer in the dark environment. Usually, azobenzene molecules will be in *trans*-state when in the dark and when exposed to UV light their conformation changes to the cis-state[64]. Muzikante et al. studied this transition from trans to cis state by measuring the surface potential using the Kelvin probe method[65].

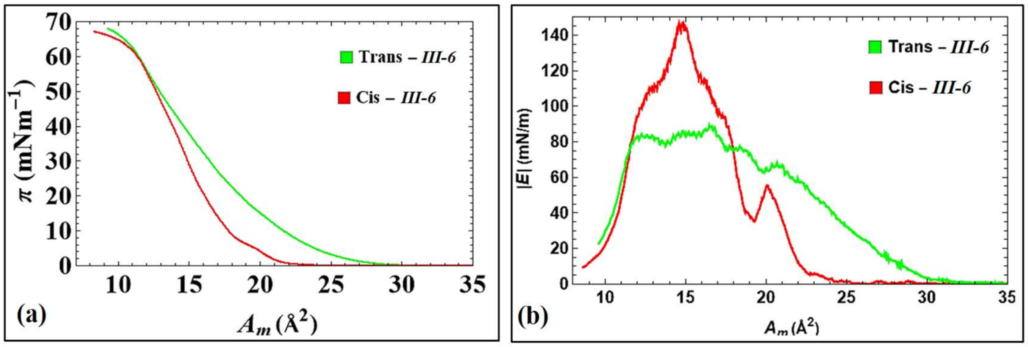

Fig. 3.19 (a) π-A_m isotherm of trans and cis-*III-6* monolayer at 298 K and (b) Variation in the compressibility moduli ($|E|$) with mean molecular area (A_m) for the Langmuir monolayer of trans and cis- *III-6* at 298 K.

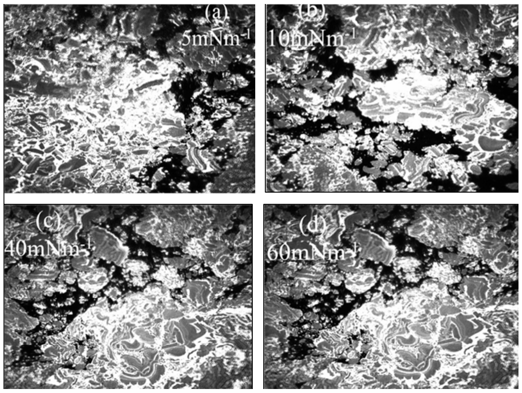

Fig. 3.20 BAM images of the trans-*III-6* monolayer at (a) Liquid Expanded (LE) phase, (b) Liquid expanded-liquid condensed co-existence region, (c) liquid condensed phase and (d) collapsed state at 298 K.

Yim et al. studied the photoisomerization using interfacial rheology of the Langmuir monolayer[66]. Studies carried out by Arya et. al., have shown that the photoisomerization from trans to cis or vice versa is a first-order kinetic process[49]. Bharat et al. found a deviation from the first-order kinetics when trans-cis photoisomerization occurs in a mesogenic azobenzene derivative[56]. We have carried out the photoisomerization of ***III-6*** molecules at different temperatures. The monolayer was compressed to a uniform LE phase and the UV light of 365 nm was shined with a fixed barrier position. The change in the conformation from trans-state to cis-state changes the surface pressure. **Fig. 3.21** shows the variation of change in the surface pressure ($\Delta\boldsymbol{\pi} = \boldsymbol{\pi}(\boldsymbol{t}) - \boldsymbol{\pi}(\mathbf{0})$) as a function of time for different temperatures of the subphase. Interestingly, we find that for temperatures less than 303 K the surface pressure decreases during the photo-isomerization and for temperatures greater than 303 K the surface pressure increases during the photo-isomerization. The change in the surface pressure as a function of time can be understood from the model given by Raghavendra et al.[67]. The model considers the simultaneous photo-isomerization of trans molecules and thermal isomerization of the cis molecules. The net change in the surface pressure of the monolayer is due to the change in the relative composition of the trans and cis isomers in the monolayer.

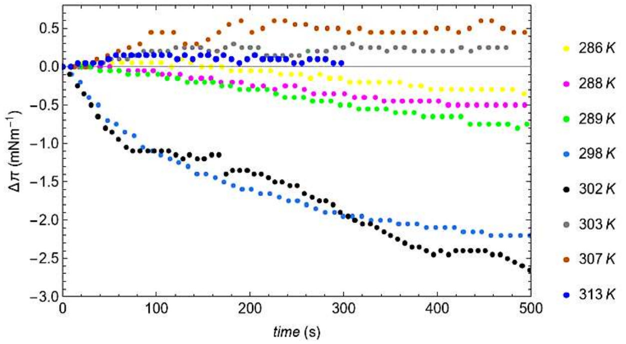

Fig. 3.21 Variation in the surface pressure as the function of time after monolayer of trans-*III-6* shined with UV light for different temperatures.

The rate of change of surface pressure as a function of time depends on the kinetics of photo-isomerization and thermal isomerization processes.

The variation in the surface pressure as a function of time can be written as formula:

$$\pi(t) = \frac{\Gamma_{tr}^{0}\,(\Delta k)(\pi_{tr}^{0} - \pi_{c}^{0})}{\Delta k + (\Gamma_{tr}^{0}\,k_2 - \Delta k)(1 - e^{-\Delta k t})} + \pi_{c}^{0} + \pi_{p}^{0} \qquad (1)$$

where, $\pi(t)$ is the surface pressure of the monolayer measured at any time t after the shining of the UV light to the monolayer formed by trans-***III-6*** molecule at $A_m = A^0{}_m$, Γ_{tr}^{0} is the mole fraction of trans -***III-6*** molecule at time $t = 0$, just before shining. π_{tr}^{0} and π_{c}^{0} are the surface pressures of pure trans and cis-***III-6*** monolayers at $A_m = A^0{}_m$. The difference in the packing fraction of the trans and cis molecules leads to another term for surface pressure denoted by π_{p}^{0}. The term Δk is the difference between k_1 and k_2, where k_1, *and* k_2 are the rate constants of photo and thermal isomerization, respectively. The equation (1) is fit to the experimental data and the rate constants of photo-isomerization and thermal isomerization are obtained from the fit parameters. **Fig. 3.22** shows the variation in the surface pressure as the function of time after the monolayer of trans-***III-6*** is shined with UV light for different temperatures along with the fit to the curves as per equation (1).

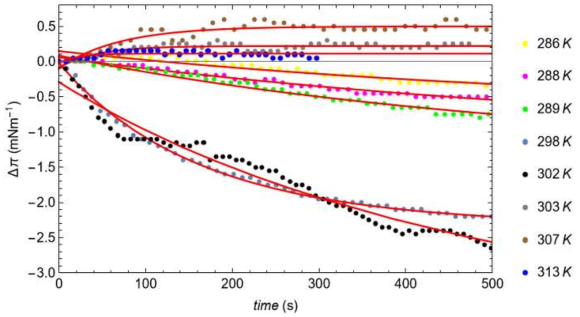

Fig. 3.22 Variation in the surface pressure as the function of time after monolayer of trans-*III-6* shined with UV light for different temperatures. The red line corresponds to the fit equation 1.

The kinetics of isomerization of ***III-6*** molecules in the monolayer at different temperatures of the subphase were studied to understand the energetics of the isomerization process. For the subphase temperatures less than 303 K, the surface pressure (π) decreases gradually with respect to time as shown in **Fig. 3.22**. The relative changes in the surface pressure increased with temperature. However, for temperatures greater than 303 K, the relative change in π increases initially with respect to time and then saturates. Earlier studies have reported only the increase in the surface pressure during photoisomerization and this was attributed to the increased dipole moment of the molecules (in cis-state) and reduced effective Am due to changes in the conformation of the molecules[56]. The switching between the positive and negative slope of π-t curves during photo isomerization at different temperatures is not observed for other azobenzene molecules. We attribute this behaviour to the presence of two azobenzene groups in a molecule. The photoisomerization of both the azobenzene groups would decrease the effective dipole moment and the area occupied by the molecules. If the thermal isomerization is high then on shining UV light, both rate of transition of trans molecules and cis molecules will be almost the same and hence effectively only one of the azobenzene moiety isomerizes there by increasing the surface pressure by a small amount. Such a behaviour can be seen for temperatures greater than 303 K for the molecules studied. However, for temperatures less than 303 K, the rate of thermal isomerization may be less as compared to the photo isomerization and hence both the azobenzene moieties isomerize to the cis state and the total dipole moment of the molecule and area per molecule decreases there by decreases the surface pressure. This claim is further supported from the calculations of rate constants of the photo and thermal isomerization processes for different temperatures. **Fig. 3.23(a)** shows the variation of k_1 and k_2 as a function of temperature. The rate constant for thermal and photo-isomerization is almost constant for temperatures less than 303 K. For temperatures greater than 303 K we found that the rate constant associated with the thermal-isomerization increases rapidly with the temperature and the variation in the photoisomerization rate constant is negligible.

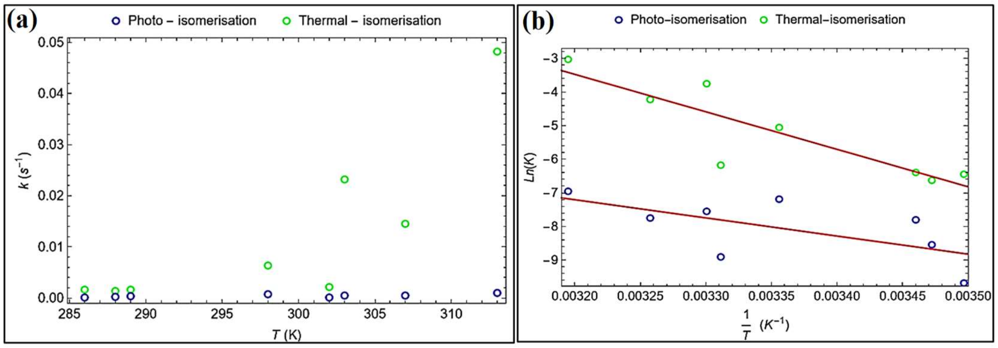

Fig. 3.23 The variation in rate constants for photo and thermal isomerisation for Langmuir monolayer of *III-6* molecule with respect to (a) temperature (b) as a function of $\frac{1}{T}$.

The activation energy associated with photo and thermal isomerization can be calculated using the Arrhenius equation given by the formula[68]:

$$\boldsymbol{lnk(T) = ln\,A - \frac{E_a}{RT}} \tag{2}$$

where $\boldsymbol{E_a}$ is the activation energy of the first-order reaction, *A* is the pre-exponential term and R, T are the universal gas constant and the subphase temperature respectively**.** **Fig. 3.23(b)** shows the plot of *ln(K)* versus $\frac{1}{T}$ for both photoisomerization and thermal isomerization processes. The slope of the plot i.e., $\frac{E_a}{RT}$ gives activation energy associated with thermal and photo-isomerization. The activation energy for photo isomerization was 44.86 kJmol^{-1} which is less than the thermal isomerization (92.7890 kJmol^{-1}) compared to other systems studied earlier[67,69].

3.4 Conclusion

In summary, this study investigated sixteen non-symmetric dimers of cyanoazobenzene and azo/azomethine naphthalenes, confirming their structural properties using various analytical techniques. The dimers exhibited enantiotropic nematic phases, with transition temperatures influenced by spacer length and odd-even effects. Dimers of ***Series III-n*** displayed higher thermal stability than azomethine naphthalene dimers (***Series IV-n***), with more pronounced mesophase stability during cooling. The azomethine linkages provided a greater mesophase range, while the azo linkages offered higher thermal stability. Photochromic behaviour was observed, with rapid photoisomerization. The spontaneous thermal back relaxation process revealed full restoration of the stable trans configuration. Computational studies added insights into the electronic structure, electrostatic potential, and optical characteristics of the dimers. We also studied thermo-photoisomerization of the molecule using the Langmuir monolayer technique. The surface pressure-area per molecule isotherm studies show that the cis-form of the ***III-6*** occupies a lower area and exhibits a co-existence region between liquid expanded and condensed phases. The BAM images show the closely packed bright images of molecules at the gaseous phase itself. The packing density of the molecules further increased in higher-ordered phases. The kinetics of isomerization of the ***III-6*** Langmuir monolayer suggests that the rate constant associated with thermal isomerization follows Arrhenius temperature dependence and at higher temperatures the rate constant increases rapidly. The photoisomerization rate constant did not vary significantly for the temperature ranges studied. The activation energy for photo isomerization (44.86 $kJmol^{-1}$) was found to be lesser than the activation energy associated with thermal isomerization (92.78 $kJmol^{-1}$).

3.5 Experimental Section:

3.5.1 Materials

All the starting materials and reagents were purchased from (S.R.L. Chemicals, Mumbai) and used without further purification. Solvents like acetone, ethyl acetate and petroleum ether (60-80) were de-moisturized and purified before use.

3.5.2. Measurements

The instruments used are the same as in section **2A.5.2.**

3.5.3 Synthesis and Characterization:

3.5.3.1 4-((E)-(4-((ω-(4-((E)-naphthalen-2-yldiazenyl)phenoxy)alkyl)oxy)phenyl) diazenyl) benzonitrile (III-n)

3.5.3.1.1 (E)-4-(naphthalen-2-yldiazenyl)phenol (NpAzOH)

The synthesis of (E)-4-(naphthalen-2-yldiazenyl)phenol (NpAzOH) is described in Chapter 2, Section 2A.5.3.1.

3.5.3.1.2 (E)-4-((4-hydroxyphenyl)diazenyl)benzonitrile (CNAzOH)[70]

A solution of 4-cyanoaniline (0.71 g, 6 mmol) in a solution of hydrochloric acid (6 ml, 4M) was added to a solution of sodium nitrite (0.42 g, 6.1 mmol) in 2 ml water, and the mixture was stirred for 4 h under N_2 atmosphere at 273–278 K. Then urea (0.01 g, 0.2 mmol) was added to decompose excessive nitrous acid, and the mixture was further stirred for 30 min. The solution of the diazonium salt was added to an aqueous phenol (0.62 g, 6.6 mmol), sodium carbonate (3 g), baking soda (0.2 g) and ice (15 g) at 273–278 K. The mixture was stirred for 7 h. After the reaction solution was neutralized with a solution of hydrochloric acid (13.6 ml, 3 M), the mixture was filtrated. Orange block-like crystals (1.27 g, 5.7 mmol,95%) were obtained by recrystallization from absolute alcohol. It was confirmed with the constant melting point. Orange crystals, Yield: 95% (1.27 g); M.P. 208 °C (reported 207 °C)[71]

3.5.3.1.3 (E)-4-((4-(n-bromoalkoxy)phenyl)diazenyl)benzonitrile (CBr-n)[70]

A mixture of 4-(4-hydroxyphenylazo)benzonitrile (0.02 mol), α,ω-dibromoalkane (0.08 mol), potassium carbonate (2.07 g, 0.015 mol) and acetone was heated under reflux with stirring for 24 h. The reaction mixture was filtered hot, and the residue was washed with acetone. The acetone was evaporated and petroleum ether was added to the concentrated organic extracts. The resulting precipitate was collected and dried. The crude product was recrystallized from ethanol twice. It was confirmed with the constant melting point. All the CBr-n were synthesized by a procedure similar to this and confirmed with the reported literature.

3.5.3.1.4 Synthesis of 4-((E)-(4-((ω-(4-((E)-naphthalen-2-yldiazenyl)phenoxy)alkyl) oxy)phenyl)diazenyl)benzonitrile (III-n)

In a round bottom flask with a reflux system and stirring for 15 minutes, (E)-4-(naphthalen-2-yldiazenyl) phenol (**NpAzOH**) (0.52 mmol) and **CBr-n** (0.5 mmol) were dissolved in acetone. Additions of anhydrous K_2CO_3 (2.17 g, 15.7 mmol) and a catalytic amount of KI were made to the reaction mixture, and the system was refluxed for about 48 h (monitored by TLC). The hot solution was filtered and washed with acetone after the reaction was finished. The filtrate was then collected and evaporated in a rotary evaporator. Cold petroleum ether was added to the concentrated extracts, and the resulting precipitate was filtered and washed two times with this same solvent. Column chromatography is used to purify the resulting compound. (96:4 pet ether: ethyl acetate)

3.5.3.1.5 Characterization of dimers III-n:

4-((E)-(4-(2-(4-((E)-naphthalen-2-yldiazenyl)phenoxy)ethoxy)phenyl)diazenyl) benzonitrile (*III-2*):

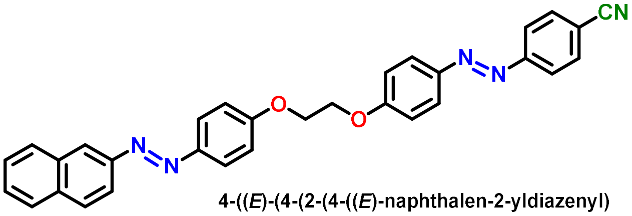

4-((*E*)-(4-(2-(4-((*E*)-naphthalen-2-yldiazenyl) phenoxy)ethoxy)phenyl)diazenyl)benzonitrile

Orange crystals, Yield: 65%; **IR** ν_{max}/cm^{-1}: 3052.34, 2948.59 (C_{sp3}-H), 2880.23, 2222.32 (C≡N), 1599.80 (-N=N-), 1241.82 (C-O), 1137.92 (C-N), 843.57; **^{1}H NMR (400 MHz, $CDCl_3$): δ (In ppm)**: 8.42 (s, 1H, Ar-H), 8.08 (d, *J* = 2 Hz, 1H, Ar-H), 8.06 (d, *J* = 2 Hz, 1H, Ar-H), 8.02 (d, *J* = 8.5 Hz, 2H, Ar-H), 7.98 (d, *J* = 8.8 Hz, 2H, Ar-H), 7.95 (d, *J* = 8.8 Hz, 2H, Ar-H), 7.80 (d, *J* = 8.8 Hz, 2H, Ar-H), 7.58 (d, *J* = 9.4 Hz, 2H, Ar-H), 7.56 (d, *J* = 8.8 Hz, 2H, Ar-H), 7.06 (d, *J* = 3.2 Hz, 2H, Ar-H), 7.04 (d, *J* = 3.2 Hz, 2H, Ar-H), 4.13 (t, *J* = 6 Hz, 4H, -O-C$\underline{H}_2$- X 2); **^{13}C NMR (400MHz, $CDCl_3$): δ (In ppm):** 162.42 (Ar C-O-), 154.84, 150.33, 147.27, 133.24, 129.25, 128.01, 127.22, 126.76, 125.57, 124.88, 123.19, 117.40, 115.13, 114.89, 66.90 (Ar-O-C-); **Elemental Analysis**: $C_{31}H_{23}N_5O_2$:(cal): C, 74.83; H, 4.66; N, 14.08; O, 6.43; found C, 74.88; H, 4.62; N, 14.04; O, 6.41; %;

***4-((E)-(4-(3-(4-((E)-naphthalen-2-yldiazenyl)phenoxy)propoxy)phenyl)diazenyl) benzonitrile* (*III-3*):**

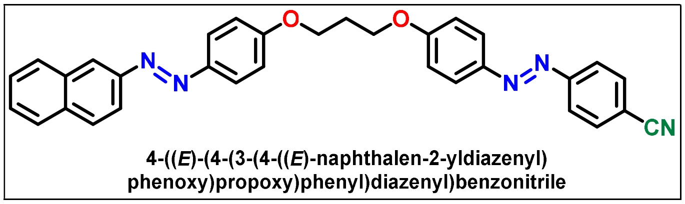

4-((*E*)-(4-(3-(4-((*E*)-naphthalen-2-yldiazenyl)
phenoxy)propoxy)phenyl)diazenyl)benzonitrile

Orange crystals, Yield: 64%; **IR** ν_{max}/cm^{-1}: 3052.29, 2966.18 (C_{sp3}-H), 2886.68, 2224.33 (C≡N), 1599.94 (-N=N-), 1244.15 (C-O), 1141.47 (C-N), 842.54; **^{1}H NMR (400 MHz, CDCl$_3$): δ (In ppm)**: 8.42 (s, 1H, Ar-H), 8.08 (d, *J* = 2 Hz, 1H, Ar-H), 8.06 (d, *J* = 2 Hz, 1H, Ar-H), 8.01 (d, *J* = 8.5 Hz, 2H, Ar-H), 7.99 (d, *J* = 8.8 Hz, 2H, Ar-H), 7.96 (d, *J* = 8.8 Hz, 2H, Ar-H), 7.80 (d, *J* = 8.8 Hz, 2H, Ar-H), 7.58 (d, *J* = 9.4 Hz, 2H, Ar-H), 7.56 (d, *J* = 8.8 Hz, 2H, Ar-H), 7.08 (d, *J* = 3.2 Hz, 2H, Ar-H), 7.06 (d, *J* = 3.2 Hz, 2H, Ar-H), 4.31 (t, *J* = 5.6 Hz, 4H-O-CH$_2$- X 2), 2.42-2.36 (m, 2H, -O-C-CH$_2$-); **^{13}C NMR (400MHz, CDCl$_3$): δ (In ppm):** 162.42 (Ar C-O-),154.84, 150.33, 147.27, 133.66, 129.33, 127.99, 127.09, 126.74, 125.57, 124.92, 123.17, 117.39, 115.01, 114.88, 64.88 (Ar-O-C-), 29.27; **Elemental Analysis**: $C_{32}H_{25}N_5O_2$:(cal): C, 75.13; H, 4.93; N, 13.69; O, 6.25; found C, 75.11; H, 4.90; N, 13.64; O, 6.21; %;

***4-((E)-(4-(4-(4-((E)-naphthalen-2-yldiazenyl)phenoxy)butoxy)phenyl)diazenyl) benzonitrile* (*III-4*)**:

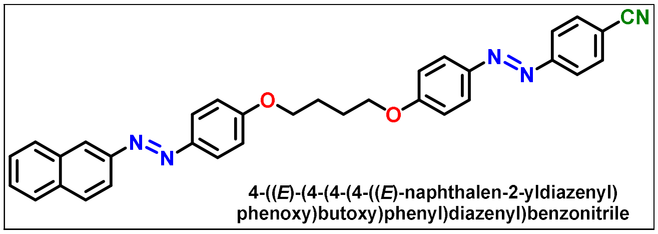

4-((*E*)-(4-(4-(4-((*E*)-naphthalen-2-yldiazenyl)
phenoxy)butoxy)phenyl)diazenyl)benzonitrile

Orange crystals, Yield: 64%; **IR** ν_{max}/cm^{-1}: 3053.73, 2946.66 (C_{sp3}-H), 2880.23, 2222.66 (C≡N), 1601.66 (-N=N-), 1253.28 (C-O), 1141.46 (C-N), 836.64; **^{1}H NMR (400 MHz, CDCl$_3$): δ (In ppm)**: 8.42 (s, 1H, Ar-H), 8.08 (d, *J* = 2 Hz, 1H, Ar-H), 8.06 (d, *J* = 2 Hz, 1H, Ar-H), 8.01 (d, *J* = 8.5 Hz, 2H, Ar-H), 7.98 (d, *J* = 8.8 Hz, 2H, Ar-

H), 7.95 (d, *J* = 8.8 Hz, 2H, Ar-H), 7.80 (d, *J* = 8.8 Hz, 2H, Ar-H), 7.58 (d, *J* = 9.4 Hz, 2H, Ar-H), 7.56 (d, *J* = 8.8 Hz, 2H, Ar-H), 7.09 (d, *J* = 3.2 Hz, 2H, Ar-H), 7.08 (d, *J* = 3.2 Hz, 2H, Ar-H), 4.32 (t, *J* = 6 Hz, 4H, -O-C$\underline{H}_2$- X 2), 2.43-2.36 (m, 4H, -O-C-$\underline{CH}_2$- X 2) ; **^{13}C NMR (400MHz, CDCl$_3$): δ (In ppm):** 162.46 (Ar C-O-), 155.51, 150.47, 147.23, 133.62, 129.34, 127.98, 127.32, 126.72, 125.50, 124.86, 123.10, 117.44, 114.95, 114.81, 69.40 (Ar-O-C-), 29.89; **Elemental Analysis**: $C_{33}H_{27}N_5O_2$:(cal): C, 75.41; H, 5.18; N, 13.32; O, 6.09; found C, 75.43; H, 5.14; N, 13.36; O, 6.10; %;

***4-((E)-(4-((5-(4-((E)-naphthalen-2-yldiazenyl)phenoxy)pentyl)oxy)phenyl)diazenyl benzonitrile* (*III-5*):**

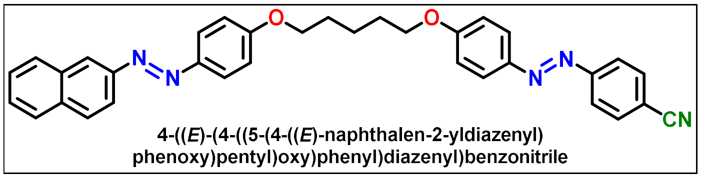

Orange crystals, Yield: 62%; **IR** ν_{max}/cm^{-1}: 3051.81, 2930.19 (C$_{sp3}$-H), 2862.11, 2219.03 (C≡N), 1598.75 (-N=N-), 1241.30 (C-O), 1139.00 (C-N), 842.93; **^{1}H NMR (400 MHz, CDCl$_3$): δ (In ppm)**: 8.42 (s, 1H, Ar-H), 8.08 (d, *J* = 2 Hz, 1H, Ar-H), 8.06 (d, *J* = 2 Hz, 1H, Ar-H), 8.01 (d, *J* = 8.5 Hz, 2H, Ar-H), 7.98 (d, *J* = 8.8 Hz, 2H, Ar-H), 7.94 (d, *J* = 8.8 Hz, 2H, Ar-H), 7.80 (d, *J* = 8.8 Hz, 2H, Ar-H), 7.58 (d, *J* = 9.4 Hz, 2H, Ar-H), 7.56 (d, *J* = 8.8 Hz, 2H, Ar-H), 7.06 (d, *J* = 3.2 Hz, 2H, Ar-H), 7.04 (d, *J* = 3.2 Hz, 2H, Ar-H), 4.13 (t, *J* = 6 Hz, 4H, -O-C$\underline{H}_2$- X 2), 2.00-1.94 (m, 4H, -O-C-$\underline{CH}_2$- X 2), 1.79-1.72 (m, 2H, -O-C-C-$\underline{CH}_2$-); **^{13}C NMR (400MHz, CDCl$_3$): δ (In ppm):** 162.68 (Ar C-O-), 154.88, 150.42, 147.16, 133.70, 129.10, 127.99, 127.22, 126.71, 125.56, 124.86, 123.15, 117.43, 114.98, 113.24, 68.28 (Ar-O-C-), 29.01, 22.80; **Elemental Analysis**: $C_{34}H_{29}N_5O_2$:(cal): C, 75.68; H, 5.42; N, 12.98; O, 5.93; found C, 75.70; H, 5.40; N, 12.99; O, 5.92; %;

***4-((E)-(4-((6-(4-((E)-naphthalen-2-yldiazenyl)phenoxy)hexyl)oxy)phenyl)diazenyl) benzonitrile* (*III-6*):**

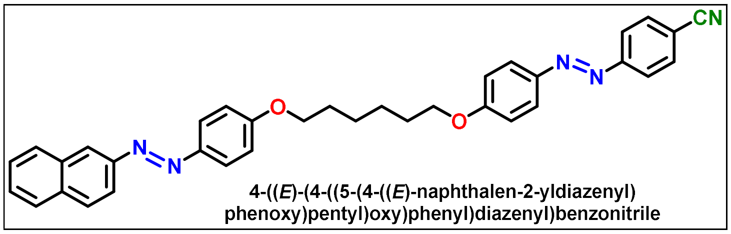

Orange crystals, Yield: 63%; **IR** ν_{max}/cm^{-1}: 3056.20, 2922.69 (C_{sp3}-H), 2850.99, 2224.05 (C≡N), 1601.47 (-N=N-), 1256.20 (C-O), 1140.80 (C-N), 839.50; **^{1}H NMR (400 MHz, $CDCl_3$): δ (In ppm)**: 8.42 (s, 1H, Ar-H), 8.08 (d, J = 2 Hz, 1H, Ar-H), 8.06 (d, J = 2 Hz, 1H, Ar-H), 8.02 (d, J = 8.5 Hz, 2H, Ar-H), 7.98 (d, J = 8.8 Hz, 2H, Ar-H), 7.95 (d, J = 8.8 Hz, 2H, Ar-H), 7.80 (d, J = 8.8 Hz, 2H, Ar-H), 7.58 (d, J = 9.4 Hz, 2H, Ar-H), 7.56 (d, J = 8.8 Hz, 2H, Ar-H), 7.06 (d, J = 3.2 Hz, 2H, Ar-H), 7.04 (d, J = 3.2 Hz, 2H, Ar-H), 4.11 (t, J = 6 Hz, 4H, -O-CH_2- X 2), 1.97-1.93 (m, 4H, -O-C-CH_2- X 2), 1.77-1.72 (m, 4H, -O-C-C-CH_2- X 2); **^{13}C NMR (400MHz, $CDCl_3$): δ (In ppm):** 162.76 (Ar C-O-), 154.90, 150.44, 147.13, 133.23, 129.31, 127.99, 127.31, 126.72, 125.56, 124.86, 123.15, 117.45, 114.98, 113.23, 68.36 (Ar-O-C-), 29.21, 25.90; **Elemental Analysis**: $C_{35}H_{31}N_5O_2$:(cal): C, 75.93; H, 5.64; N, 12.65; O, 5.78; found C, 75.90; H, 5.65; N, 12.63; O, 6.41; %;

***4-((E)-(4-((8-(4-((E)-naphthalen-2-yldiazenyl)phenoxy)octyl)oxy)phenyl)diazenyl) benzonitrile* (*III-8*):**

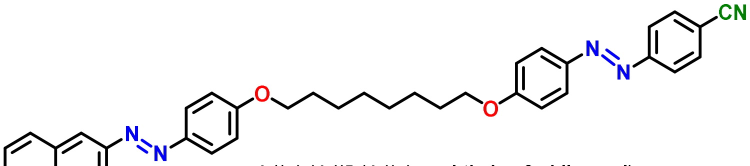

4-((*E*)-(4-((5-(4-((*E*)-naphthalen-2-yldiazenyl)
phenoxy)pentyl)oxy)phenyl)diazenyl)benzonitrile

Orange crystals, Yield: 65%; **IR** ν_{max}/cm^{-1}: 3057.00, 2922.73 (C_{sp3}-H), 2851.01, 2224.23 (C≡N), 1601.39 (-N=N-), 1257.63 (C-O), 1140.60 (C-N), 836.35; **^{1}H NMR (400 MHz, $CDCl_3$): δ (In ppm)**: 8.46 (s, 1H, Ar-H), 8.08 (d, J = 2 Hz, 1H, Ar-H), 8.06 (d, J = 2 Hz, 1H, Ar-H), 8.02 (d, J = 8.5 Hz, 2H, Ar-H), 7.98 (d, J = 8.8 Hz, 2H, Ar-H), 7.95 (d, J = 8.8 Hz, 2H, Ar-H), 7.80 (d, J = 8.8 Hz, 2H, Ar-H), 7.58 (d, J = 9.4 Hz, 2H, Ar-H), 7.56 (d, J = 8.8 Hz, 2H, Ar-H), 7.06 (d, J = 3.2 Hz, 2H, Ar-H), 7.03 (d, J = 3.2 Hz, 2H, Ar-H), 4.07 (t, J = 6 Hz, 4H, -O-CH_2- X 2), 1.89-1.83 (m, 4H, -O-C-CH_2- X 2), 1.51-1.38 (m, 8H, -O-C-C-$(CH_2)_4$-); **^{13}C NMR (400MHz, $CDCl_3$): δ (In ppm):** 162.74 (Ar C-O-), 154.83, 150.34, 147.00, 133.16, 129.23, 127.91, 127.22, 126.85, 125.47, 124.78, 123.07, 117.38, 114.90, 113.14, 68.44 (Ar-O-C-), 29.26, 29.18, 25.93; **Elemental Analysis**: $C_{37}H_{35}N_5O_2$:(cal): C, 76.40; H, 6.06; N, 12.04; O, 5.50; found C, 76.43; H, 6.07; N, 12.06; O, 5.51; %;

***4-((E)-(4-((10-(4-((E)-naphthalen-2-yldiazenyl)phenoxy)decyl)oxy)phenyl)diazenyl) benzonitrile* (*III-10*):**

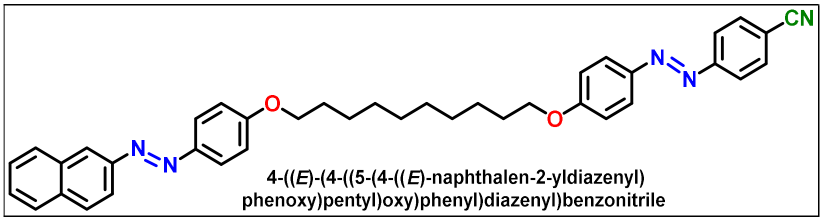

Orange crystals, Yield: 64%; **IR** ν_{max}/cm^{-1}: 3057.34, 2925.53 (C$_{sp3}$-H), 2853.76, 2220.04 (C≡N), 1599.24 (-N=N-), 1250.94 (C-O), 1143.48 (C-N), 839.84; **^{1}H NMR (400 MHz, CDCl$_3$): δ (In ppm)**: 8.42 (s, 1H, Ar-H), 8.08 (d, *J* = 2 Hz, 1H, Ar-H), 8.06 (d, *J* = 2 Hz, 1H, Ar-H), 8.02 (d, *J* = 8.5 Hz, 2H, Ar-H), 7.98 (d, *J* = 8.8 Hz, 2H, Ar-H), 7.95 (d, *J* = 8.8 Hz, 2H, Ar-H), 7.80 (d, *J* = 8.8 Hz, 2H, Ar-H), 7.58 (d, *J* = 9.4 Hz, 2H, Ar-H), 7.56 (d, *J* = 8.8 Hz, 2H, Ar-H), 7.06 (d, *J* = 3.2 Hz, 2H, Ar-H), 7.04 (d, *J* = 3.2 Hz, 2H, Ar-H), 4.19 (t, *J* = 6 Hz, 4H, -O-CH$_2$- X 2), 1.89-1.83 (m, 4H, -O-C-CH$_2$- X 2), 1.50-1.34 (m, 12H, -O-C-C-(CH$_2$)$_6$-); **^{13}C NMR (400MHz, CDCl$_3$): δ (In ppm):** 162.77 (Ar C-O-),154.83, 150.29, 146.94, 134.54, 129.24, 127.01, 127.23, 126.84, 125.47, 124.83, 123.07, 117.39, 115.13, 114.90, 68.50 (Ar-O-C-), 29.45, 29.19, 29.14, 26.01; **Elemental Analysis**: $C_{39}H_{39}N_5O_2$:(cal): C, 76.82; H, 6.45; N, 11.49; O, 5.25; found C, 76.84; H, 6.42; N, 11.45; O, 5.21; %;

***4-((E)-(4-((12-(4-((E)-naphthalen-2-yldiazenyl)phenoxy)dodecyl)oxy)phenyl)diazenyl) benzonitrile* (*III-12*):**

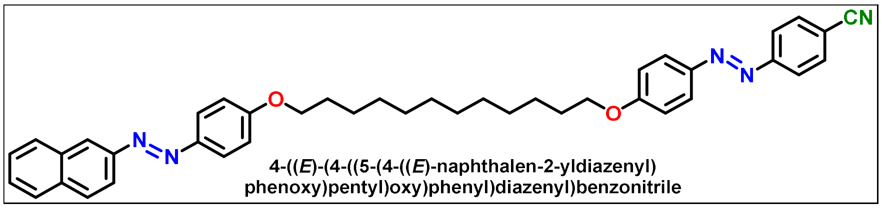

Orange crystals, Yield: 66%; **IR** ν_{max}/cm^{-1}: 3059.14, 2923.70 (C$_{sp3}$-H), 2851.50, 2223.60 (C≡N), 1601.36 (-N=N-), 1255.18 (C-O), 1141.23 (C-N), 840.97; **^{1}H NMR (400 MHz, CDCl$_3$): δ (In ppm)**: 8.42 (s, 1H, Ar-H), 8.08 (d, *J* = 2 Hz, 1H, Ar-H), 8.06 (d, *J* = 2 Hz, 1H, Ar-H), 8.02 (d, *J* = 8.5 Hz, 2H, Ar-H), 7.98 (d, *J* = 8.8 Hz, 2H, Ar-H), 7.95 (d, *J* = 8.8 Hz, 2H, Ar-H), 7.80 (d, *J* = 8.8 Hz, 2H, Ar-H), 7.58 (d, *J* = 9.4 Hz, 2H, Ar-H), 7.56 (d, *J* = 8.8 Hz, 2H, Ar-H), 7.06 (d, *J* = 3.2 Hz, 2H, Ar-H), 7.04 (d, *J* = 3.2 Hz, 2H, Ar-H), 4.07 (t, *J* = 6 Hz, 4H, -O-CH$_2$- X 2), 1.89-1.83 (m, 4H, -O-C-CH$_2$- X 2), 1.51-1.38 (m, 16H, -O-C-C-(CH$_2$)$_8$-); **^{13}C NMR (400MHz, CDCl$_3$): δ (In ppm):**

162.45 (Ar C-O-), 154.82, 149.71, 147.27, 133.16, 129.31, 127.93, 127.4, 126.70, 125.49, 124.76, 123.07, 117.34, 114.90, 113.29, 68.52 (Ar-O-C-), 29.53, 29.35, 29.18, 26.00; **Elemental Analysis**: $C_{41}H_{43}N_5O_2$:(cal): C, 77.21; H, 6.80; N, 10.98; O, 5.02; found C, 77.20; H, 6.83; N, 10.95; O, 5.03; %;

3.5.3.2. 4-((E)-(4-((ω(4-((E)-(naphthalen-2-ylimino)methyl)phenoxy)alkyl)oxy)phenyl)diazenyl)benzonitrile (IV-n)

3.5.3.2.1 (E)-4-((naphthalen-2-ylimino)methyl)phenol (NpAmOH)

The synthesis of (E)-4-((naphthalen-2-ylimino)methyl)phenol (NpAmOH) is described in Chapter 2, Section 2A.5.3.2.

3.5.3.2.2 (E)-4-((4-hydroxyphenyl)diazenyl)benzonitrile (CNAzOH)

The synthesis of (E)-4-((4-hydroxyphenyl)diazenyl)benzonitrile (CNAzOH) is detailed in section 3.5.3.1.2.

3.5.3.2.3 (E)-4-((4-(n-bromoalkoxy)phenyl)diazenyl)benzonitrile (CBr-n)[70]

The synthesis of (E)-4-((4-(n-bromoalkoxy)phenyl)diazenyl)benzonitrile (CBr-n) is given in section 3.5.3.1.3.

3.5.3.2.4 Synthesis of 4-((E)-(4-((ω(4-((E)-(naphthalen-2-ylimino)methyl)phenoxy) alkyl)oxy) phenyl)diazenyl)benzonitrile (IV-n)

In a round bottom flask with a reflux system and stirring for 15 minutes, (E)-4-((naphthalen-2-ylimino)methyl)phenol (**NpAmOH**) (0.52 mmol) and **CBr-n** (0.5 mmol) were dissolved in acetone. Additions of anhydrous K_2CO_3 (2.17 g, 15.7 mmol) and a catalytic amount of KI were made to the reaction mixture, and the system was refluxed for about 48 h (monitored by TLC). The hot solution was filtered and washed with acetone after the reaction was finished. The filtrate was then collected and evaporated in a rotary evaporator. Cold petroleum ether was added to the concentrated extracts, and the resulting precipitate was filtered and washed two times with this same solvent. To obtain the desired product, the crude precipitate was recrystallised twice from ethanol.

3.5.3.2.5 Characterization of dimers IV-n

***4-((E)-(4-(2-(4-((E)-(naphthalen-2-ylimino)methyl)phenoxy)ethoxy)phenyl)diazenyl)benzonitrile* (*IV-2*):**

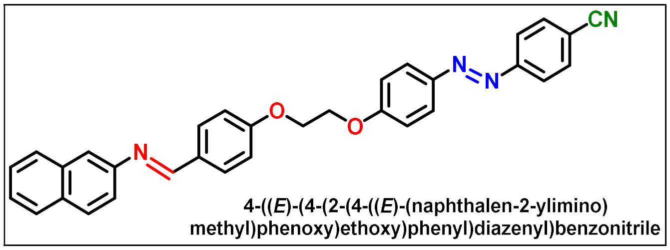

4-((*E*)-(4-(2-(4-((*E*)-(naphthalen-2-ylimino)
methyl)phenoxy)ethoxy)phenyl)diazenyl)benzonitrile

Orange crystals, Yield: 65%; **IR** ν_{max}/cm^{-1}: 3053.65, 2937.52 (C_{sp3}-H), 2864.64, 2220.41 (C≡N), 1601.35 (-CH=N-), 1247.34 (C-O), 1137.82 (C-N), 841.12; **^{1}H NMR (400 MHz, $CDCl_3$): δ (In ppm)**: 8.56 (s, 1H, -N=CH-), 8.01 (d, *J* = 8.4 Hz, 2H, Ar-H), 7.96 (d, *J* = 8.4 Hz, 2H, Ar-H), 7.94 (d, *J* = 8.4 Hz, 2H, Ar-H), 7.87 (d, *J* = 7.2 Hz, 2H, Ar-H), 7.82 (d, *J* = 8.0 Hz, 2H, Ar-H), 7.61 (s, 1H, Ar-H), 7.50 (d, *J* = 7.4 Hz, 2H, Ar-H), 7.46 (d, *J* = 8.0 Hz, 2H, Ar-H), 7.13 (d, *J* = 8.8 Hz, 2H, Ar-H), 7.00 (d, *J* = 9.2 Hz, 2H, Ar-H), 4.48 (t, *J* = 6 Hz, 4H, -O-CH_2- X 2); **^{13}C NMR (400MHz, $CDCl_3$): δ (In ppm):** 163.46, 162.00 (Ar C-O-), 159.92, 154.82, 147.19, 134.94, 133.18, 129.65, 127.98, 127.72, 126.42, 125.80, 125.30, 123.15, 118.63, 117.73, 114.94, 113.38, 68.36 (Ar-O-C-); **Elemental Analysis**: $C_{32}H_{24}N_4O_2$:(cal): C, 77.40; H, 4.87; N, 11.28; O, 6.44; found C, 77.36; H, 4.82; N, 11.24; O, 6.42; %;

***4-((E)-(4-(3-(4-((E)-(naphthalen-2-ylimino)methyl)phenoxy)propoxy)phenyl)diazenyl)benzonitrile* (*IV-3*):**

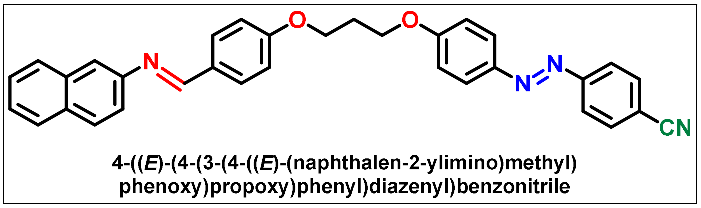

4-((*E*)-(4-(3-(4-((*E*)-(naphthalen-2-ylimino)methyl)
phenoxy)propoxy)phenyl)diazenyl)benzonitrile

Orange crystals, Yield: 67%; **IR** ν_{max}/cm^{-1}: 3062.62, 2959.68 (C_{sp3}-H), 2878.33, 2224.78 (C≡N), 1601.07 (-CH=N-), 1247.61 (C-O), 1138.41 (C-N), 841.02; **^{1}H NMR (400 MHz, $CDCl_3$): δ (In ppm)**: 8.54 (s, 1H, -N=CH-), 7.98 (d, *J* = 7.4 Hz, 2H, Ar-H), 7.96 (d, *J* = 8.4 Hz, 2H, Ar-H), 7.94 (d, *J* = 8.4 Hz, 2H, Ar-H), 7.88 (d, *J* = 8.4 Hz, 2H, Ar-H), 7.82 (d, *J* = 8.0 Hz, 2H, Ar-H), 7.59 (s, 1H, Ar-H), 7.49 (d, *J* = 7.4 Hz, 2H, Ar-H), 7.46 (d, *J* = 8.0 Hz, 2H, Ar-H), 7.08 (d, *J* = 8.8 Hz, 2H, Ar-H), 7.05 (d, *J* = 8.8 Hz, 2H, Ar-H), 4.30 (t, *J* = 6 Hz, 4H, -O-CH_2- X 2), 2.41-2.35 (m, 2H, -O-C-CH_2-); **^{13}C NMR (400MHz, $CDCl_3$): δ (In ppm):** 163.80, 162.33 (Ar C-O-), 159.77, 154.78, 147.19, 134.94, 133.18, 129.65, 127.98, 127.72, 126.42, 125.80, 125.30, 123.15, 118.64, 117.73, 114.93, 113.29, 68.36 (Ar-O-C-), 29.10; **Elemental Analysis**: $C_{33}H_{26}N_4O_2$:(cal): C, 77.63; H, 5.13; N, 10.97; O, 6.27; found C, 77.66; H, 5.18; N, 10.93; O, 6.24; %;

4-((E)-(4-(4-(4-((E)-(naphthalen-2-ylimino)methyl)phenoxy)butoxy)phenyl)diazenyl)benzonitrile (IV-4):

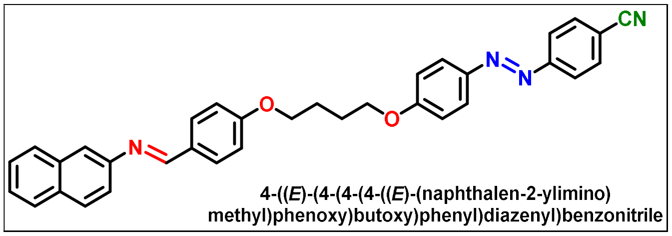

Orange crystals, Yield: 67%; **IR** ν_{max}/cm^{-1}: 3055.57, 2931.46 (C_{sp3}-H), 2873.87, 2222.33 (C≡N), 1597.45 (-CH=N-), 1248.06 (C-O), 1137.05 (C-N), 840.93; **^{1}H NMR (400 MHz, $CDCl_3$): δ (In ppm)**: 8.54 (s, 1H, -N=CH-), 7.98 (d, *J* = 8.4 Hz, 2H, Ar-H), 7.96 (d, *J* = 8.4 Hz, 2H, Ar-H), 7.94 (d, *J* = 8.4 Hz, 2H, Ar-H), 7.86 (d, *J* = 8.0 Hz, 2H, Ar-H), 7.81 (d, *J* = 8.4 Hz, 2H, Ar-H), 7.60 (s, 1H, Ar-H), 7.50 (d, *J* = 7.4 Hz, 2H, Ar-H), 7.46 (d, *J* = 8.0 Hz, 2H, Ar-H), 7.06 (d, *J* = 9.2 Hz, 2H, Ar-H), 7.02 (d, *J* = 8.0 Hz, 2H, Ar-H), 4.19 (t, *J* = 6 Hz, 4H, -O-CH_2- X 2), 2.22-2.08 (m, 4H, -O-C-CH_2- X 2); **^{13}C NMR (400MHz, $CDCl_3$): δ (In ppm):** 162.89, 161.55 (Ar C-O-), 158.53, 154.07, 145.78, 133.90, 132.13, 128.19, 127.96, 126.95, 126.66, 125.41, 125.30, 124.23, 118.64, 117.65, 113.88, 113.73, 68.13 (Ar-O-C-), 28.30; **Elemental Analysis**: $C_{34}H_{28}N_4O_2$:(cal): C, 77.84; H, 5.38; N, 10.68; O, 6.10; found C, 77.86; H, 5.41; N, 10.63; O, 6.06; %;

4-((E)-(4-((5-(4-((E)-(naphthalen-2-ylimino)methyl)phenoxy)pentyl)oxy)phenyl) diazenyl)benzonitrile (IV-5):

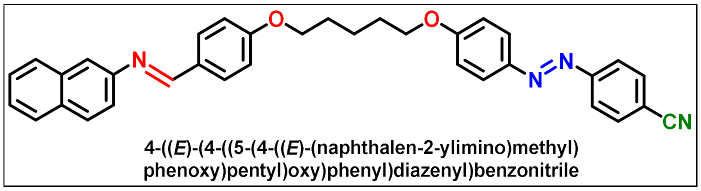

Orange crystals, Yield: 68%; **IR** ν_{max}/cm^{-1}: 3053.43, 2944.24 (C_{sp3}-H), 2867.30, 2220.96 (C≡N), 1602.74 (-CH=N-), 1247.41 (C-O), 1139.30 (C-N), 842.54; **^{1}H NMR (400 MHz, $CDCl_3$): δ (In ppm)**: 8.54 (s, 1H, -N=CH-), 7.97 (d, *J* = 8.4 Hz, 2H, Ar-

H), 7.93 (d, J = 8.4 Hz, 2H, Ar-H), 7.88 (d, J = 8.4 Hz, 2H, Ar-H), 7.85 (d, J = 7.2 Hz, 2H, Ar-H), 7.80 (d, J = 8.0 Hz, 2H, Ar-H), 7.60 (s, 1H, Ar-H), 7.51 (d, J = 7.4 Hz, 2H, Ar-H), 7.46 (d, J = 8.0 Hz, 2H, Ar-H), 7.06 (d, J = 8.8 Hz, 2H, Ar-H), 7.02 (d, J = 9.2 Hz, 2H, Ar-H), 4.13 (t, J = 6 Hz, 4H, -O-CH$_2$- X 2), 2.00-1.94 (m, 4H, -O-C-CH$_2$- X 2), 1.78-1.67 (m, 2H, -O-C-C-CH$_2$-); **^{13}C NMR (400MHz, CDCl$_3$): δ (In ppm):** 163.46, 162.00 (Ar C-O-), 159.92, 154.82, 150.33, 147.19, 134.94, 133.18, 129.65, 127.98, 127.72, 126.42, 125.80, 125.30, 123.15, 117.73, 115.09, 114.94, 68.36 (Ar-O-C-), 27.86, 21.68; **Elemental Analysis**: C$_{35}$H$_{30}$N$_4$O$_2$:(cal): C, 78.04; H, 5.61; N, 10.40; O, 5.94; found C, 78.06; H, 5.66; N, 10.37; O, 5.95; %;

4-((E)-(4-((6-(4-((E)-(naphthalen-2-ylimino)methyl)phenoxy)hexyl)oxy)phenyl) diazenyl)benzonitrile (*IV-6*):

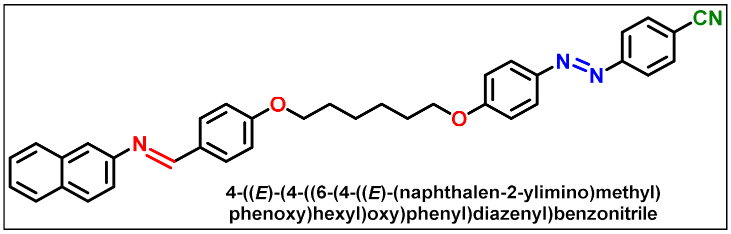

Orange crystals, Yield: 67%; **IR** ν$_{max}$/cm^{-1}: 3053.38, 2944.33 (C$_{sp3}$-H), 2867.61, 2220.98 (C≡N), 1602.56 (-CH=N-), 1246.87 (C-O), 1139.32 (C-N), 842.87; **^{1}H NMR (400 MHz, CDCl$_3$): δ (In ppm)**: 8.53 (s, 1H, -N=CH-), 7.97 (d, J = 8.4 Hz, 2H, Ar-H), 7.93 (d, J = 8.4 Hz, 2H, Ar-H), 7.89 (d, J = 8.4 Hz, 2H, Ar-H), 7.85 (d, J = 7.2 Hz, 2H, Ar-H), 7.80 (d, J = 8.0 Hz, 2H, Ar-H), 7.59 (s, 1H, Ar-H), 7.50 (d, J = 7.4 Hz, 2H, Ar-H), 7.46 (d, J = 8.0 Hz, 2H, Ar-H), 7.04 (d, J = 8.8 Hz, 2H, Ar-H), 7.02 (d, J = 9.2 Hz, 2H, Ar-H), 4.10 (t, J = 6 Hz, 4H, -O-CH$_2$- X 2), 2.00-1.94 (m, 4H, -O-C-CH$_2$- X 2), 1.79-1.65 (m, 2H, -O-C-C-CH$_2$-); **^{13}C NMR (400MHz, CDCl$_3$): δ (In ppm):** 163.46, 162.00 (Ar C-O-), 159.92, 154.82, 150.33, 147.19, 134.94, 133.18, 129.65, 127.98, 127.72, 126.42, 125.80, 125.30, 123.15, 117.73, 115.09, 114.94, 68.36 (Ar-O-C-), 29.08, 21.80; **Elemental Analysis**: C$_{36}$H$_{32}$N$_4$O$_2$:(cal): C, 78.24; H, 5.84; N, 10.14; O, 5.79; found C, 78.22; H, 5.86; N, 10.12; O, 5.74; %;

4-((E)-(4-((8-(4-((E)-(naphthalen-2-ylimino)methyl)phenoxy)octyl)oxy)phenyl) diazenyl)benzonitrile (*IV-8*):

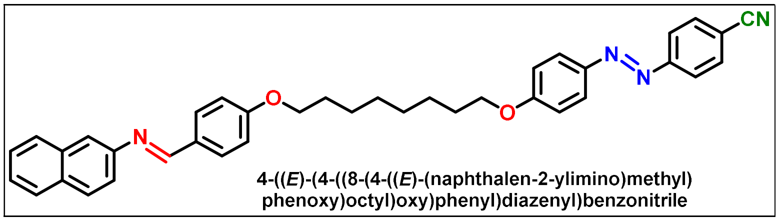

Orange crystals, Yield: 66%; **IR** ν_{max}/cm^{-1}: 3055.68, 2940.16 (C_{sp3}-H), 2865.84, 2224.43 (C≡N), 1602.92 (-CH=N-), 1249.33 (C-O), 1140.95 (C-N), 841.36; **^{1}H NMR (400 MHz, $CDCl_3$): δ (In ppm)**: 8.53 (s, 1H, -N=CH-), 7.98 (d, *J* = 8.4 Hz, 2H, Ar-H), 7.93 (d, *J* = 8.4 Hz, 2H, Ar-H), 7.88 (d, *J* = 8.4 Hz, 2H, Ar-H), 7.86 (d, *J* = 7.2 Hz, 2H, Ar-H), 7.80 (d, *J* = 8.0 Hz, 2H, Ar-H), 7.59 (s, 1H, Ar-H), 7.51 (d, *J* = 7.4 Hz, 2H, Ar-H), 7.44 (d, *J* = 8.0 Hz, 2H, Ar-H), 7.04 (d, *J* = 8.8 Hz, 2H, Ar-H), 7.01 (d, *J* = 9.2 Hz, 2H, Ar-H), 4.06 (t, *J* = 6 Hz, 4H, -O-CH_2- X 2), 1.87-1.86 (m, 4H, -O-C-CH_2- X 2), 1.54-1.45 (m, 8H, -O-C-C-(**CH_2**)$_4$-); **^{13}C NMR (400MHz, $CDCl_3$): δ (In ppm):** 164.24, 162.74 (Ar C-O-), 159.94, 154.83, 146.75, 134.93, 133.16, 129.82, 127.99, 127.72, 126.47, 125.79, 125.48, 123.07, 118.22, 114.89, 113.17, 68.36 (Ar-O-C-), 29.26, 29.12, 25.94; **Elemental Analysis**: $C_{38}H_{36}N_4O_2$:(cal): C, 78.59; H, 6.25; N, 9.65; O, 5.51; found C, 78.56; H, 6.26; N, 9.61; O, 5.49; %;

4-((E)-(4-((10-(4-((E)-(naphthalen-2-ylimino)methyl)phenoxy)decyl)oxy)phenyl) diazenyl)benzonitrile (IV-10):

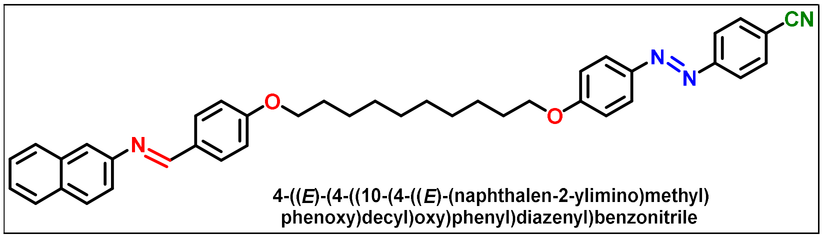

Orange crystals, Yield: 67%; **IR** ν_{max}/cm^{-1}: 3055.21, 2921.01 (C_{sp3}-H), 2851.54, 2221.30 (C≡N), 1603.16 (-CH=N-), 1251.59 (C-O), 1140.94 (C-N), 842.35 **^{1}H NMR (400 MHz, $CDCl_3$): δ (In ppm)**: 8.53 (s, 1H, -N=CH-), 7.97 (d, *J* = 8.4 Hz, 2H, Ar-H), 7.93 (d, *J* = 8.4 Hz, 2H, Ar-H), 7.88 (d, *J* = 8.4 Hz, 2H, Ar-H), 7.85 (d, *J* = 7.2 Hz, 2H, Ar-H), 7.80 (d, *J* = 8.0 Hz, 2H, Ar-H), 7.60 (s, 1H, Ar-H), 7.51 (d, *J* = 7.4 Hz, 2H, Ar-H), 7.46 (d, *J* = 8.0 Hz, 2H, Ar-H), 7.04 (d, *J* = 8.8 Hz, 2H, Ar-H), 7.02 (d, *J* = 9.2 Hz, 2H, Ar-H), 4.06 (t, *J* = 6.1 Hz, 4H, -O-CH_2- X 2), 1.89-1.85 (m, 4H, -O-C-CH_2- X 2), 1.51-1.39 (m, 12H, -O-C-C-(CH_2)$_6$-) ; **^{13}C NMR (400MHz, $CDCl_3$): δ (In ppm):** 163.21, 161.73 (Ar C-O-), 158.84, 154.82, 150.33, 147.19, 134.94, 133.18, 129.65, 127.98, 127.72, 126.42, 125.80, 125.30, 123.15, 117.73, 115.09, 114.94, 68.36 (Ar-O-C-), 28.42, 28.30, 28.13, 24.95; **Elemental Analysis**: $C_{40}H_{40}N_4O_2$:(cal): C, 78.92; H, 6.62; N, 9.20; O, 5.26; found C, 78.89; H, 6.59; N, 9.17; O, 5.23; %;

4-((E)-(4-((12-(4-((E)-(naphthalen-2-ylimino)methyl)phenoxy)dodecyl)oxy)phenyl) diazenyl)benzonitrile (IV-12):

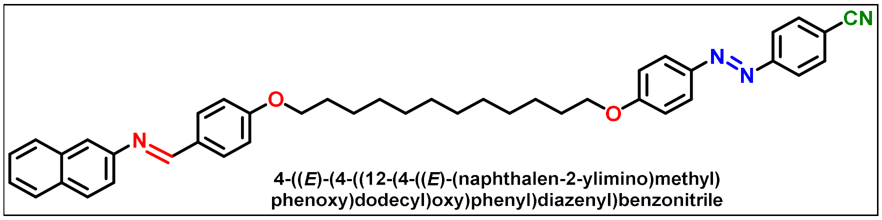

Orange crystals, Yield: 69%; **IR** ν_{max}/cm^{-1}: 3057.00, 2921.57 (C_{sp3}-H), 2852.45, 2221.48 (C≡N), 1602.28 (-CH=N-), 1251.15 (C-O), 1141.01 (C-N), 842.91; **^{1}H NMR (400 MHz, $CDCl_3$): δ (In ppm)**: 8.54 (s, 1H, -N=CH-), 7.97 (d, J = 8.4 Hz, 2H, Ar-H), 7.93 (d, J = 8.4 Hz, 2H, Ar-H), 7.88 (d, J = 8.4 Hz, 2H, Ar-H), 7.85 (d, J = 7.2 Hz, 2H, Ar-H), 7.80 (d, J = 8.0 Hz, 2H, Ar-H), 7.60 (s, 1H, Ar-H), 7.51 (d, J = 7.4 Hz, 2H, Ar-H), 7.46 (d, J = 8.0 Hz, 2H, Ar-H), 7.04 (d, J = 8.8 Hz, 2H, Ar-H), 7.01 (d, J = 9.2 Hz, 2H, Ar-H), 4.06 (t, J = 6 Hz, 4H, -O-CH_2- X 2), 1.85-1.83 (m, 4H, -O-C-CH_2- X 2), 1.50-1.34 (m, 16H, -O-C-C-$(CH_2)_8$-); **^{13}C NMR (400MHz, $CDCl_3$): δ (In ppm):** 164.27, 162.78 (Ar C-O-), 159.93, 154.83, 150.33, 146.73, 134.93, 133.16, 129.79, 127.99, 127.71, 126.42, 125.80, 125.32, 123.07, 117.78, 115.09, 114.90, 68.43 (Ar-O-C-), 29.55, 29.37, 29.16, 26.01; **Elemental Analysis**: $C_{42}H_{44}N_4O_2$:(cal): C, 78.21; H, 6.96; N, 8.80; O, 5.02; found C, 78.19; H, 6.95; N, 8.83; O, 5.05; %;

3.6 Spectras

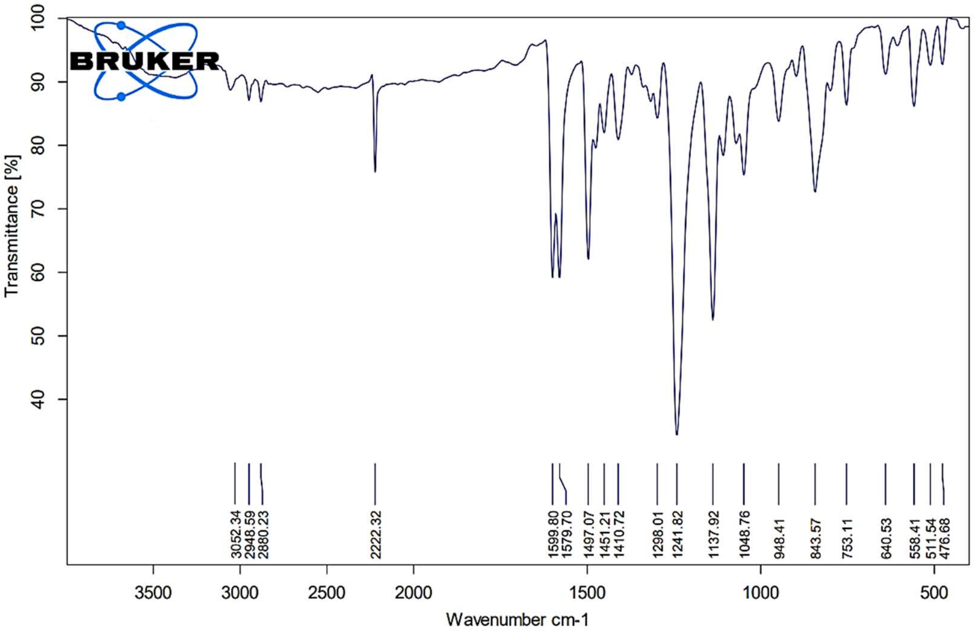

Fig. S3.1: FT-IR spectra of *III-2*

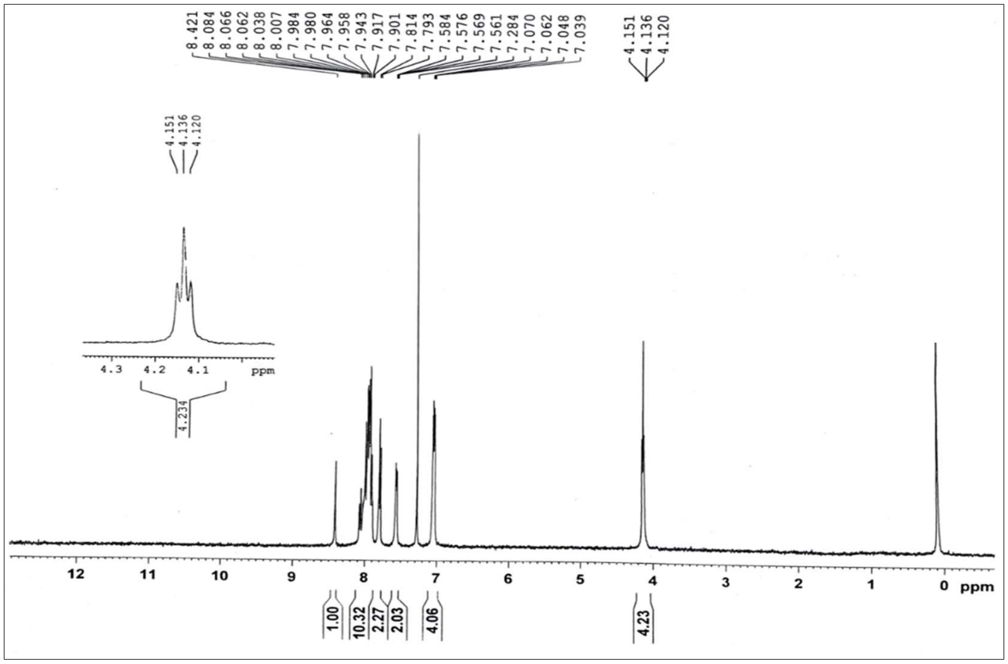

Fig. S3.2: ^{1}H-NMR spectra of *III-2*

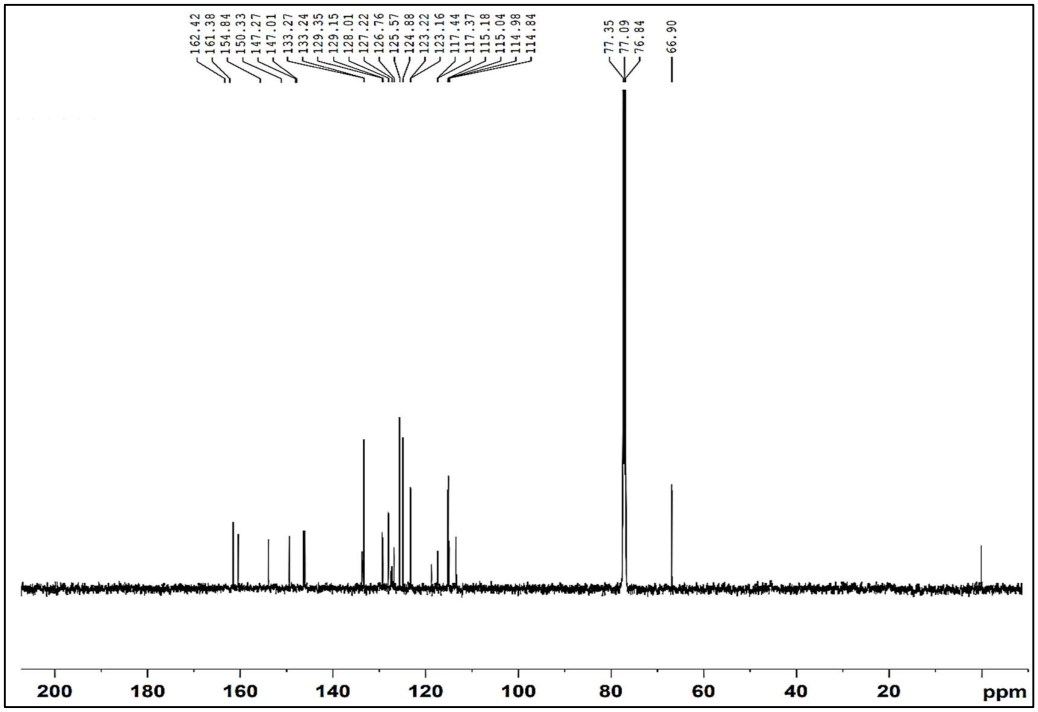

Fig. S3.3: ^{13}C-NMR spectra of *III-2*

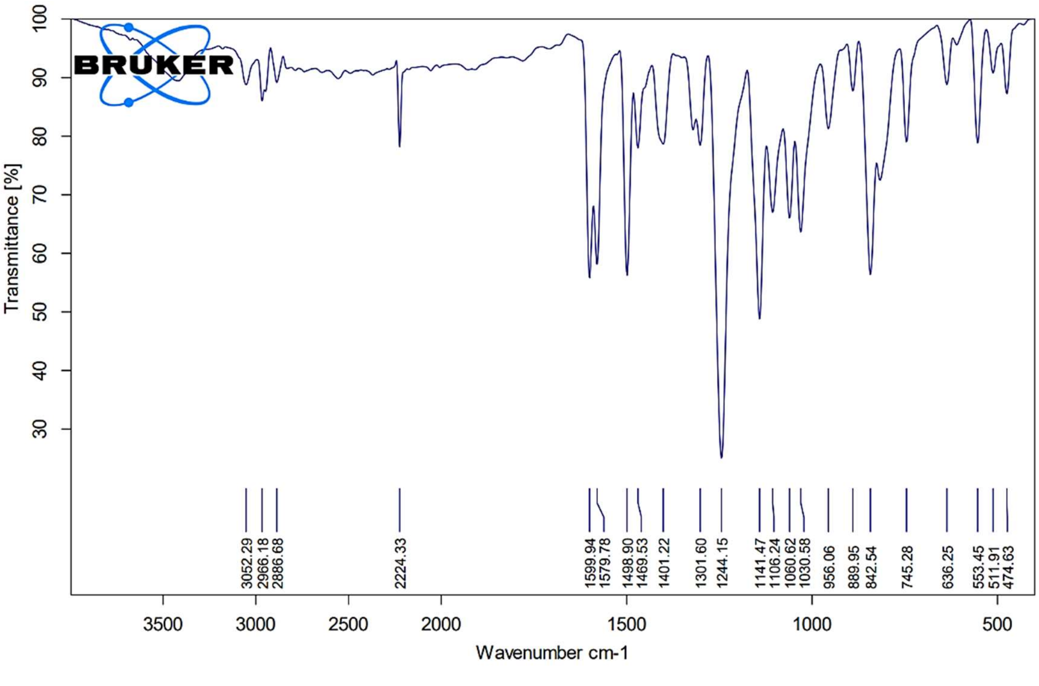

Fig. S3.4: FT-IR spectra of *III-3*

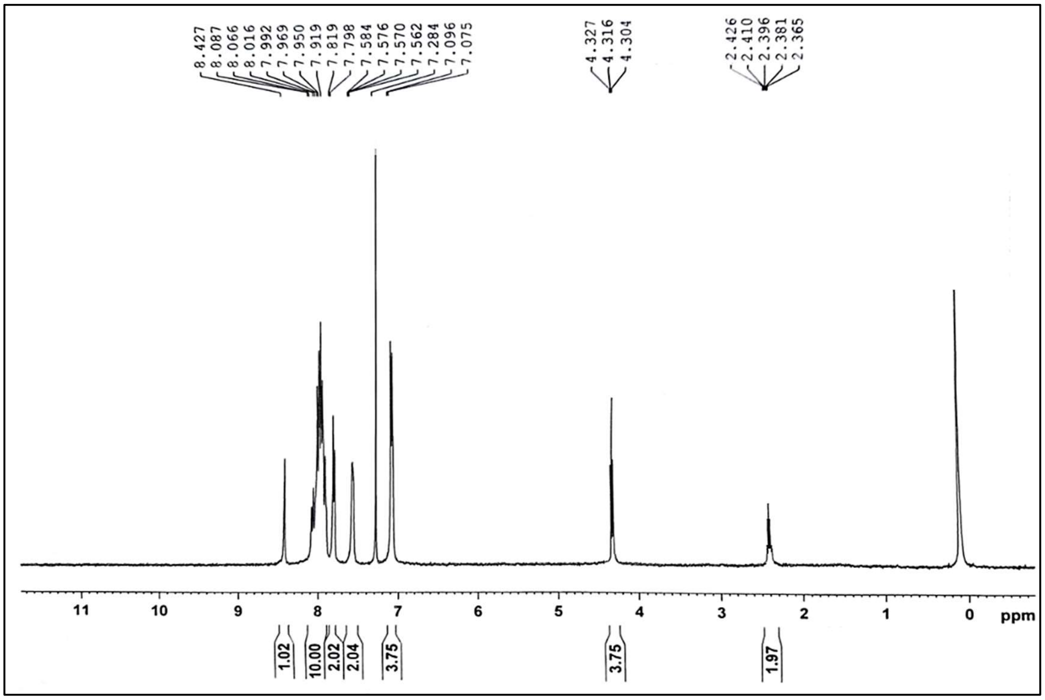

Fig. S3.5: ^{1}H-NMR spectra of *III-3*

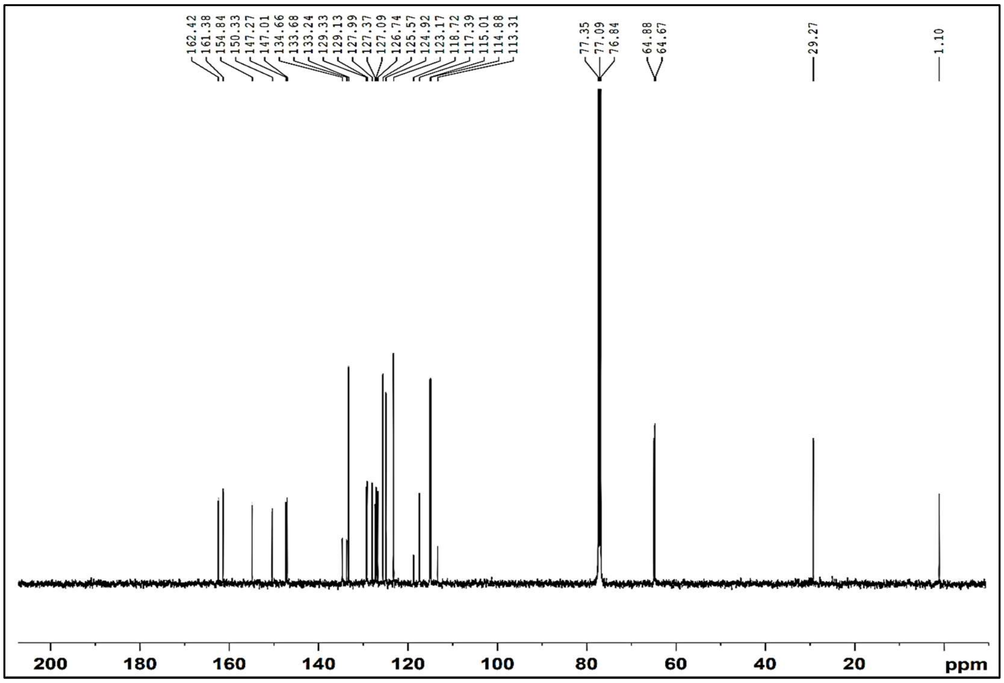

Fig. S3.6: ^{13}C-NMR spectra of *III-3*

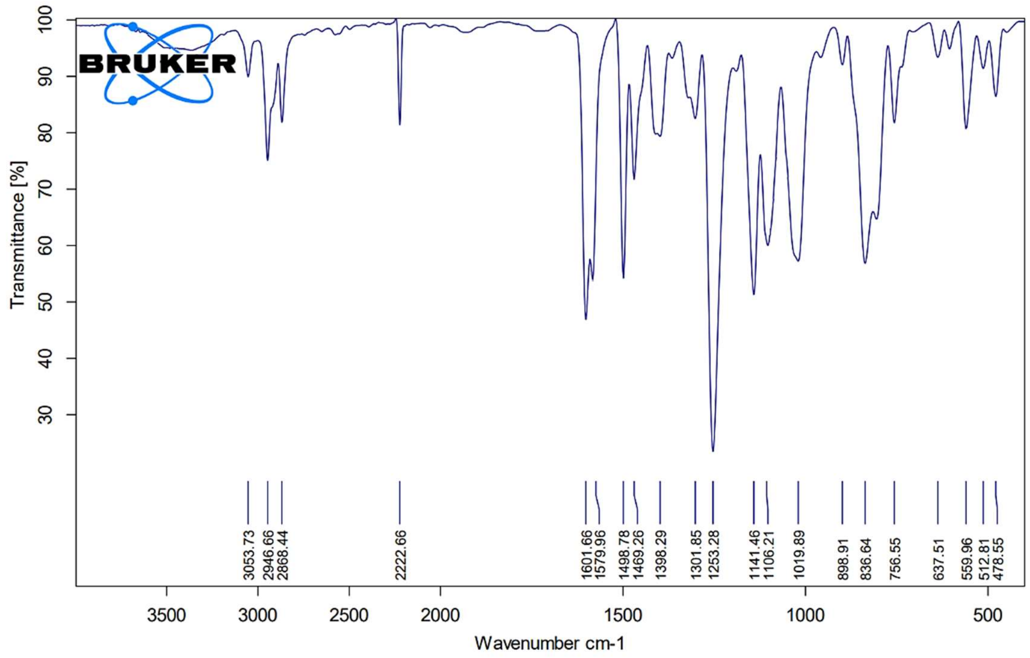

Fig. S3.7: FT-IR spectra of *III-4*

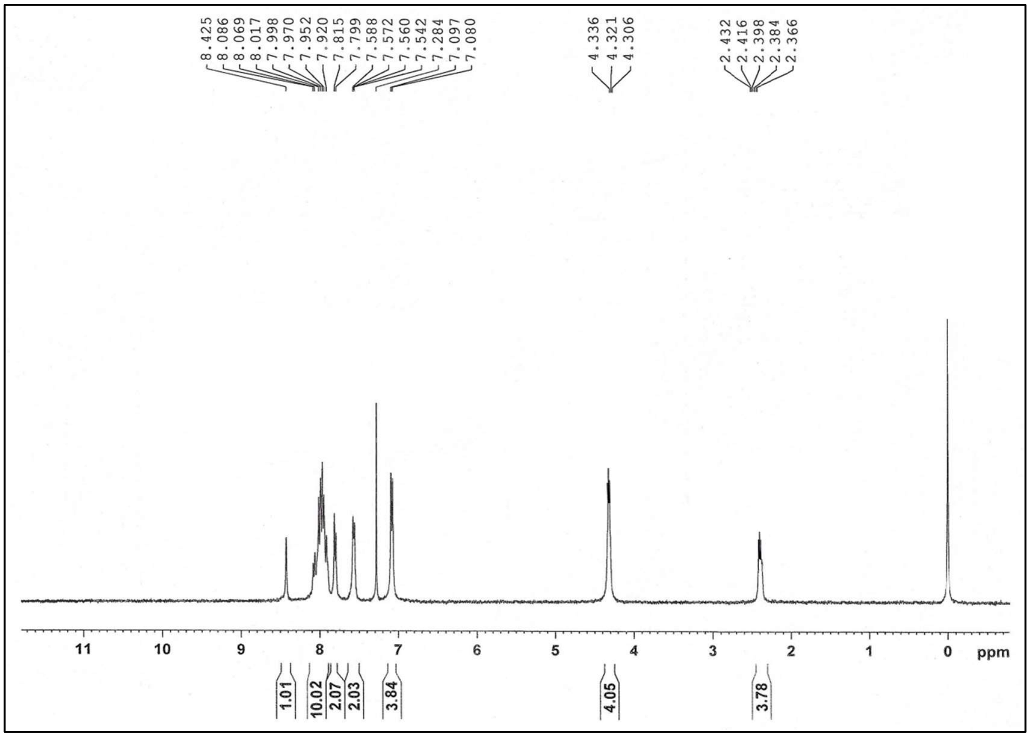

Fig. S3.8: ^{1}H-NMR spectra of *III-4*

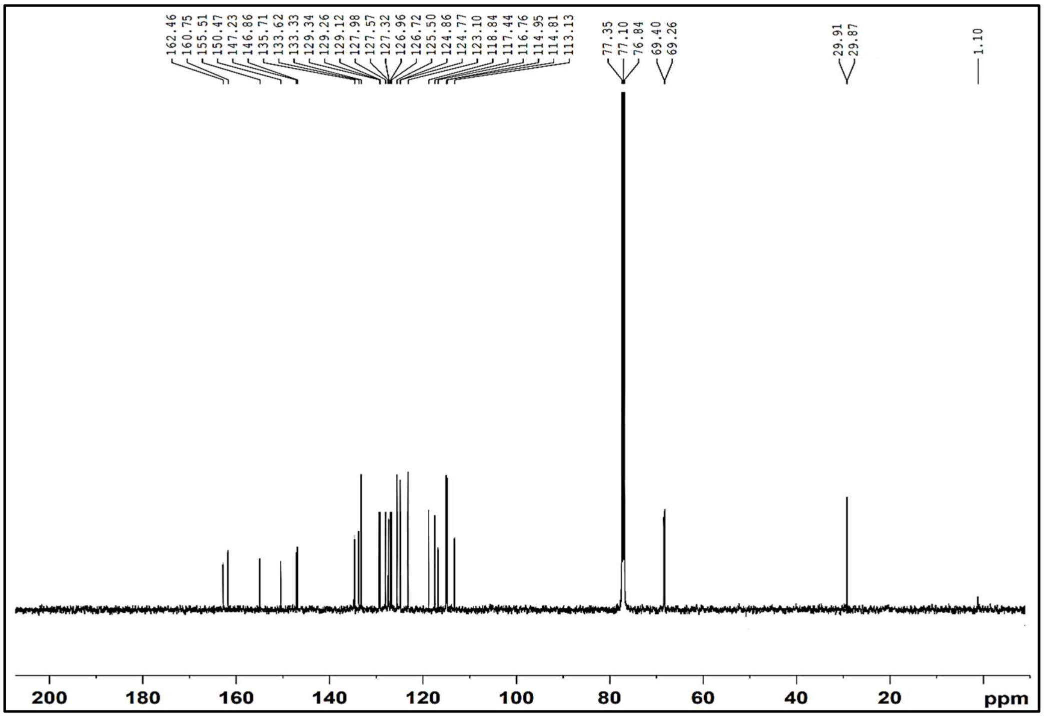

Fig. S3.9: ^{13}C-NMR spectra of *III-4*

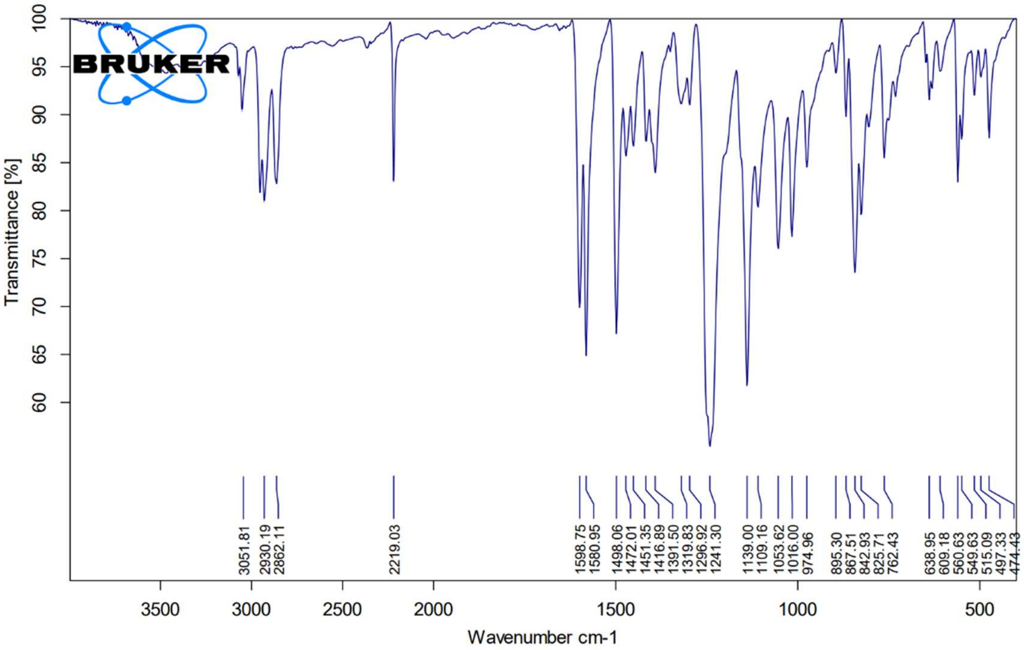

Fig. S3.10: FT-IR spectra of *III-5*

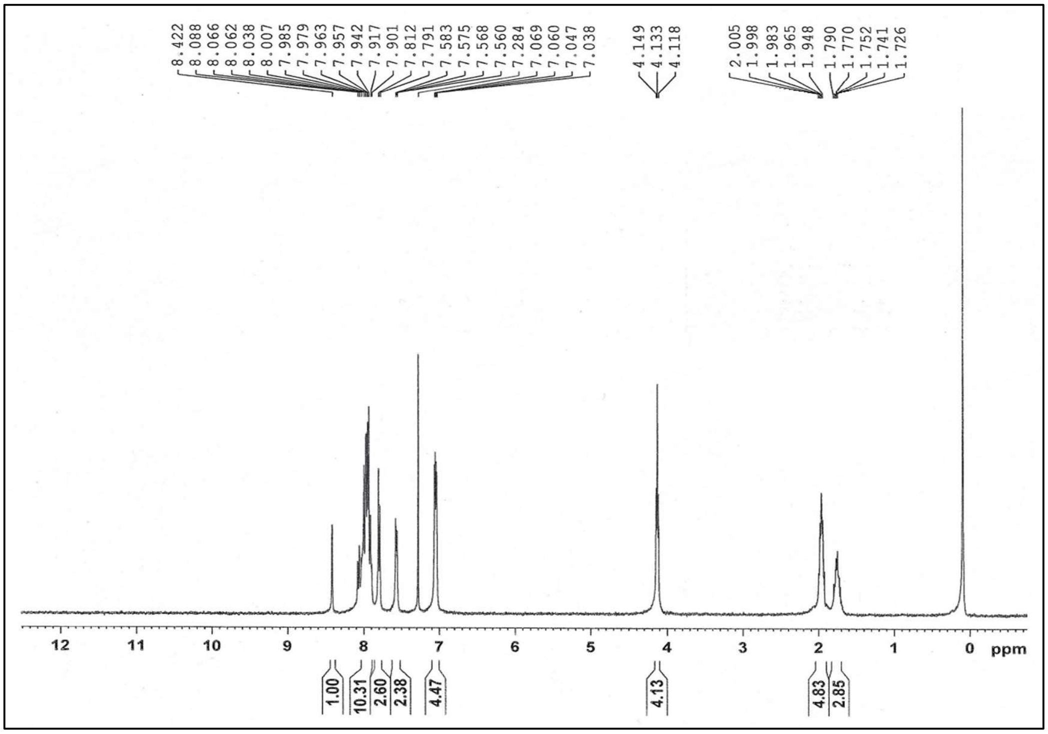

Fig. S3.11: ^{1}**H-NMR spectra of** ***III-5***

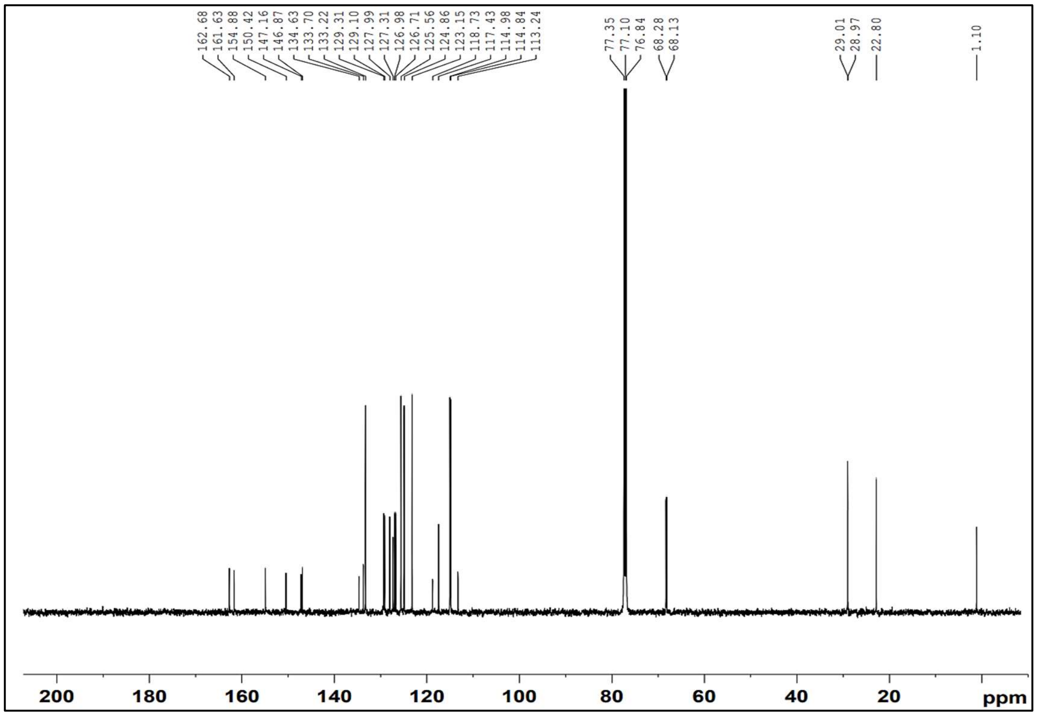

Fig. S3.12: ^{13}**C-NMR spectra of** ***III-5***

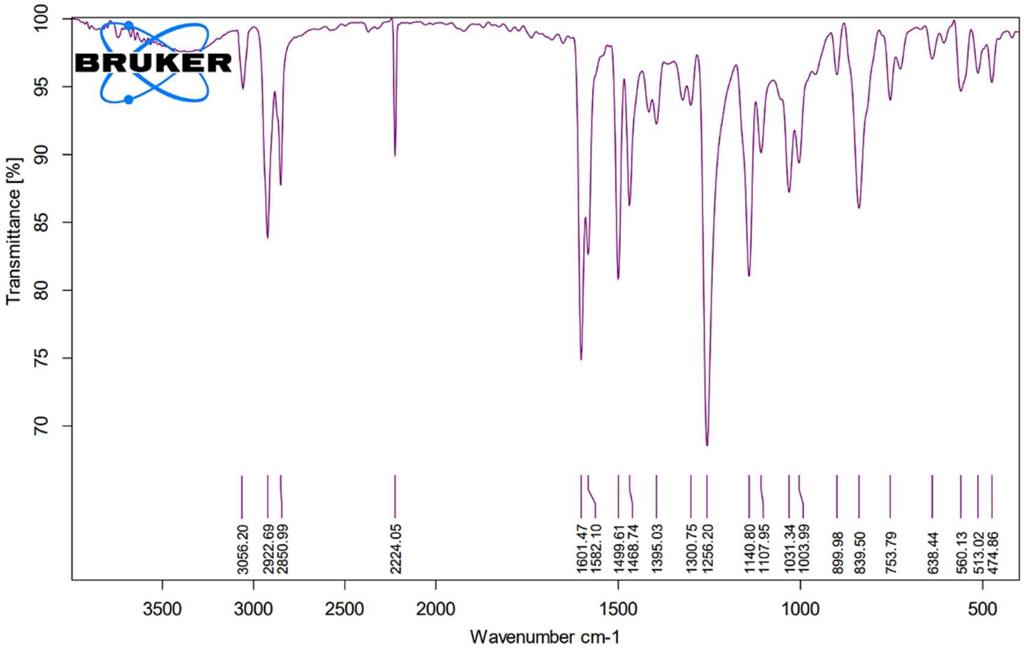

Fig. S313: FT-IR spectra of *III-6*

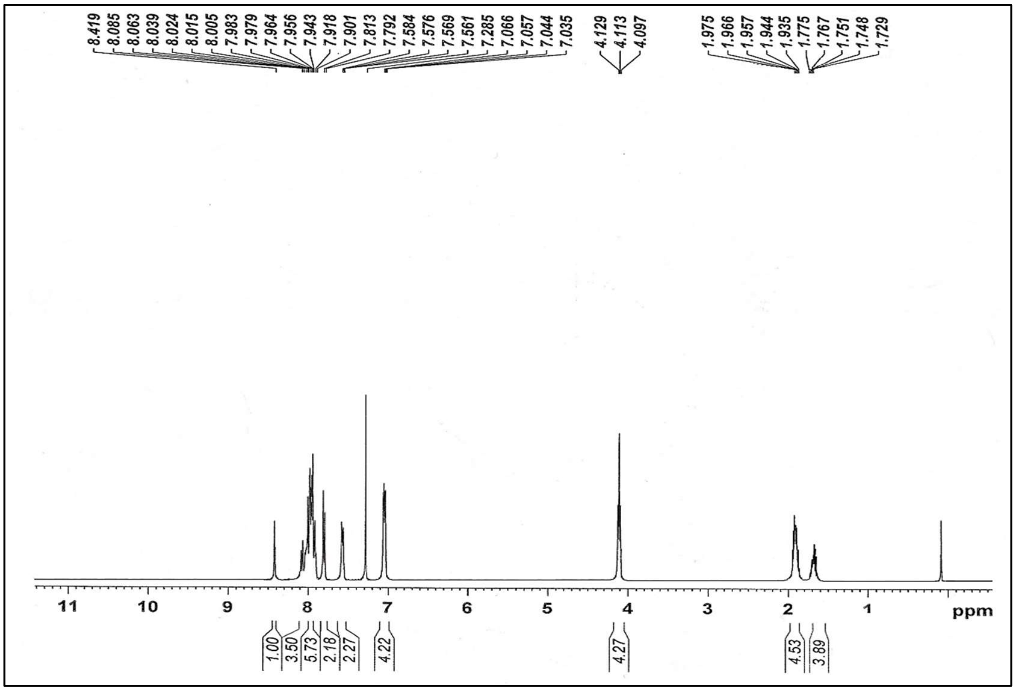

Fig. S3.14 ^{1}H-NMR spectra of *III-6*

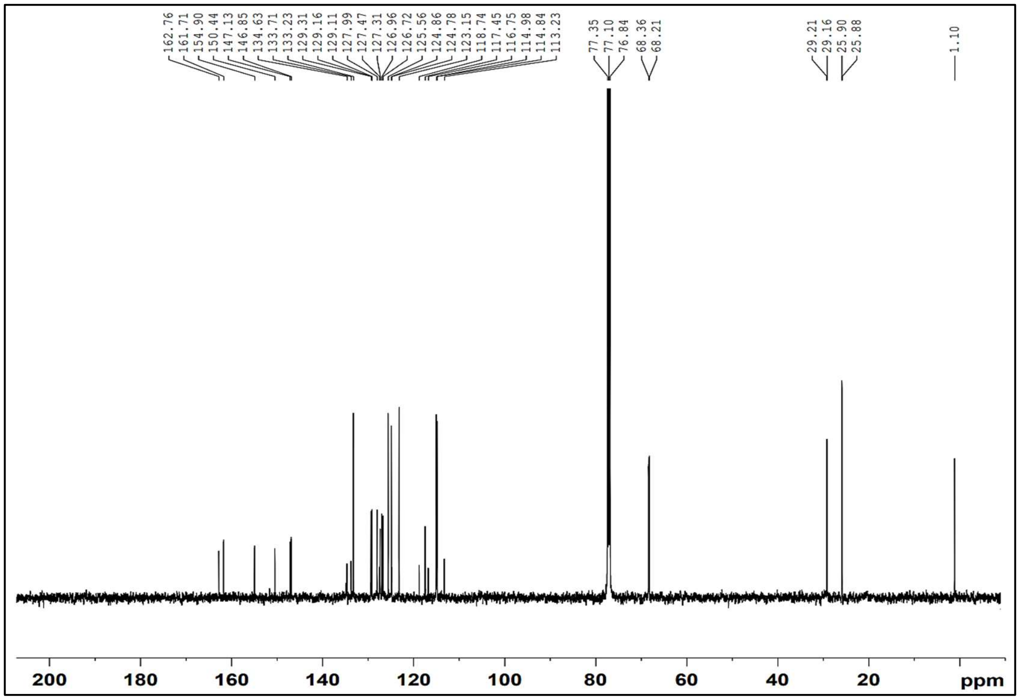

Fig. S3.15: ^{13}C-NMR spectra of *III-6*

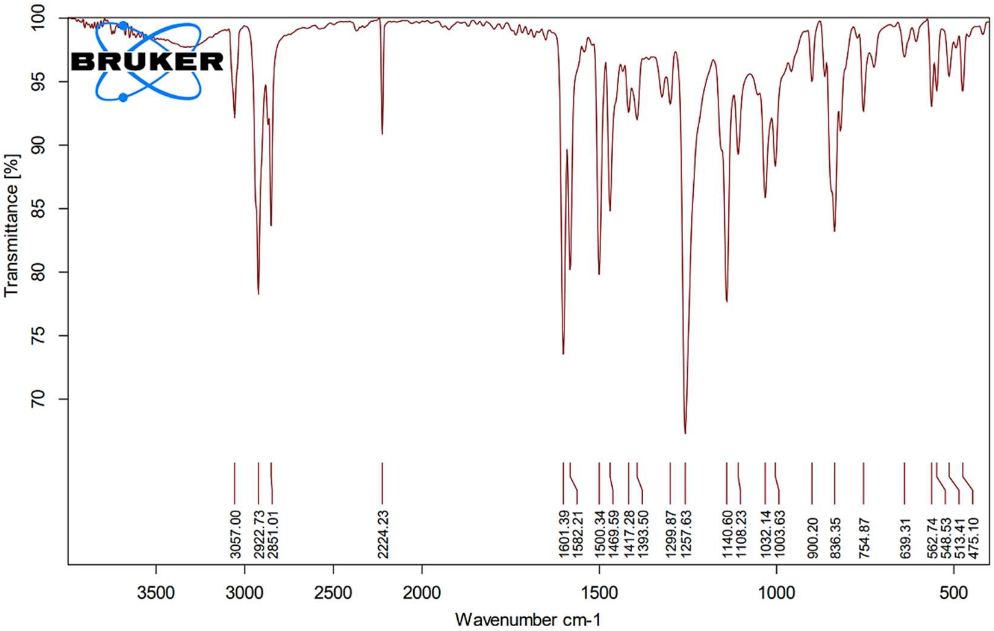

Fig. S3.16: FT-IR spectra of *III-8*

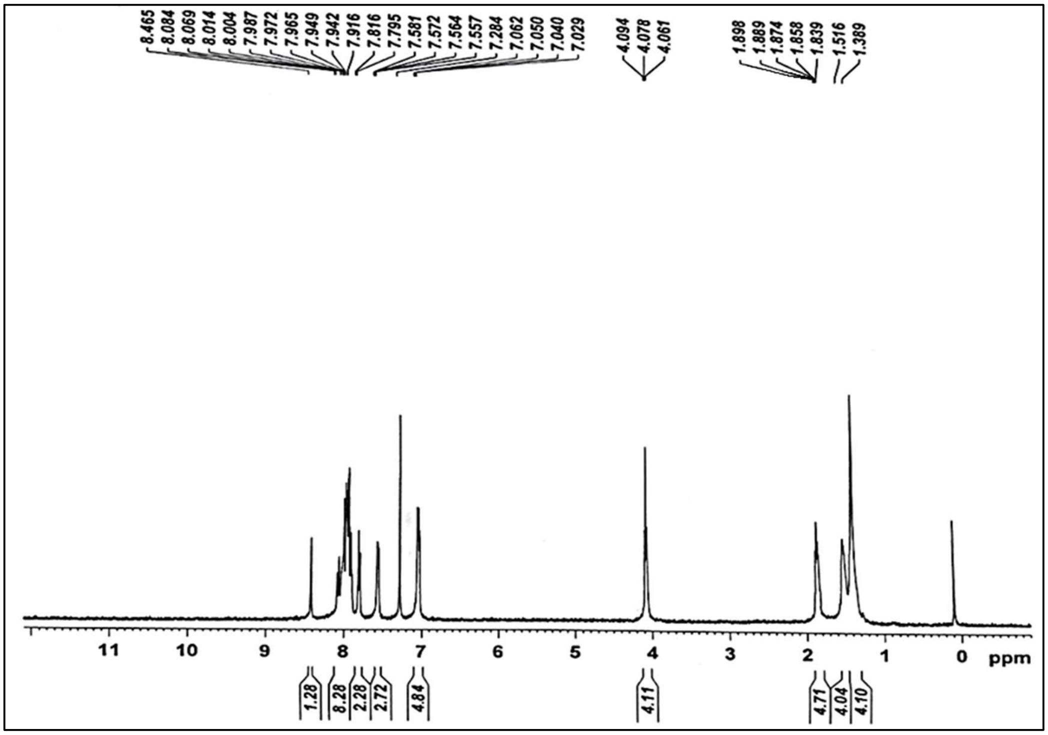

Fig. S3.17: ^{1}H-NMR spectra of *III-8*

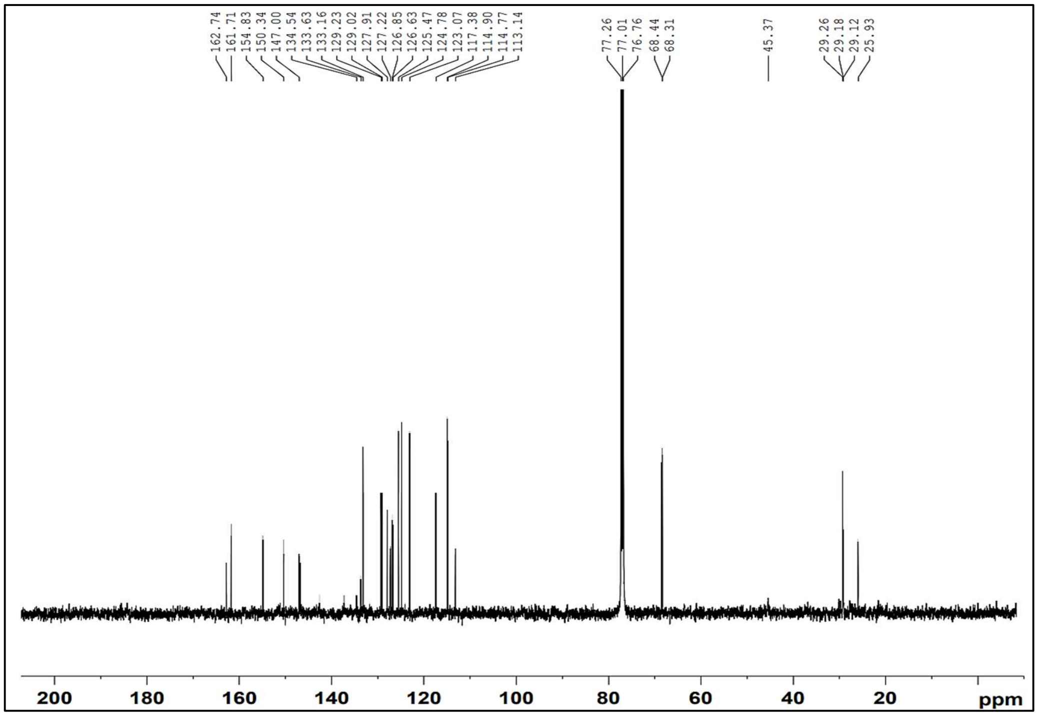

Fig. S3.18: ^{13}C-NMR spectra of *III-8*

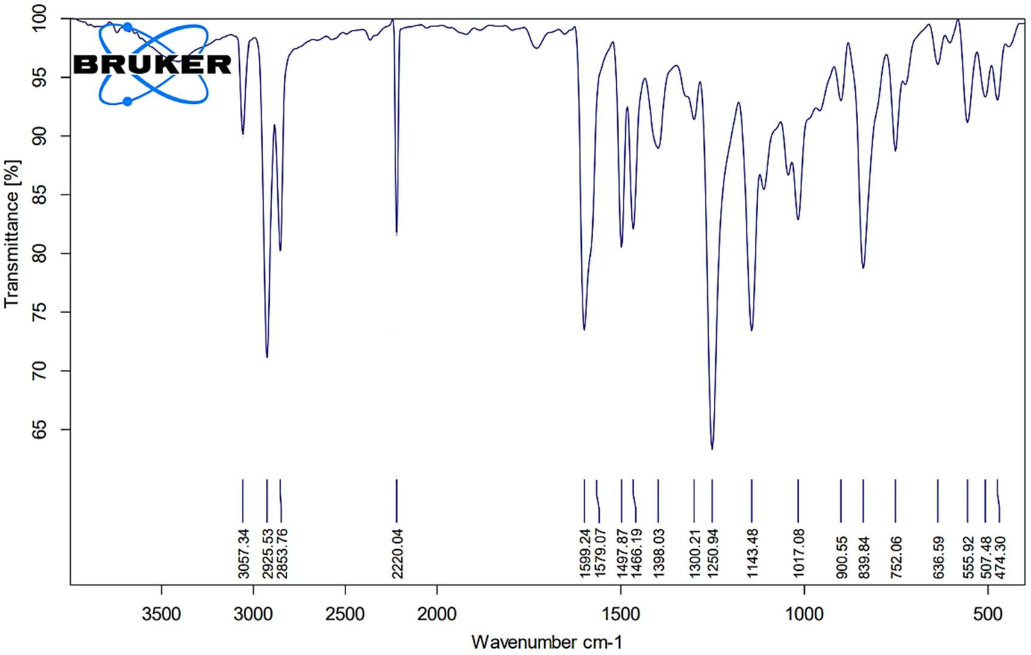

Fig. S3.19: FT-IR spectra of *III-10*

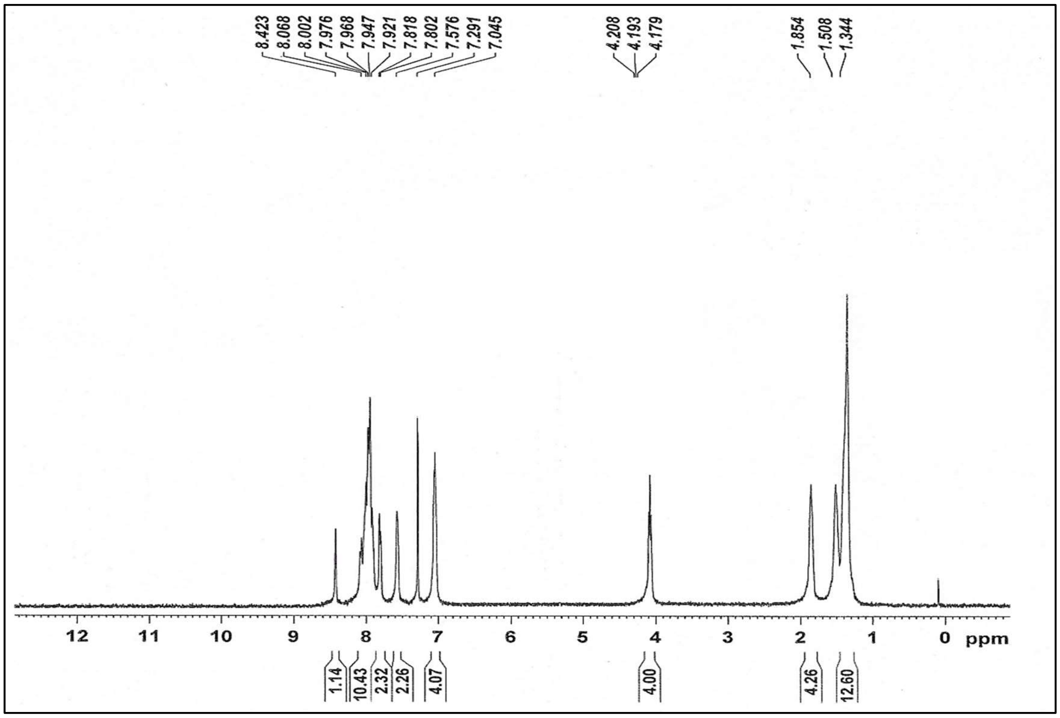

Fig. S3.20: ^{1}H-NMR spectra of *III-10*

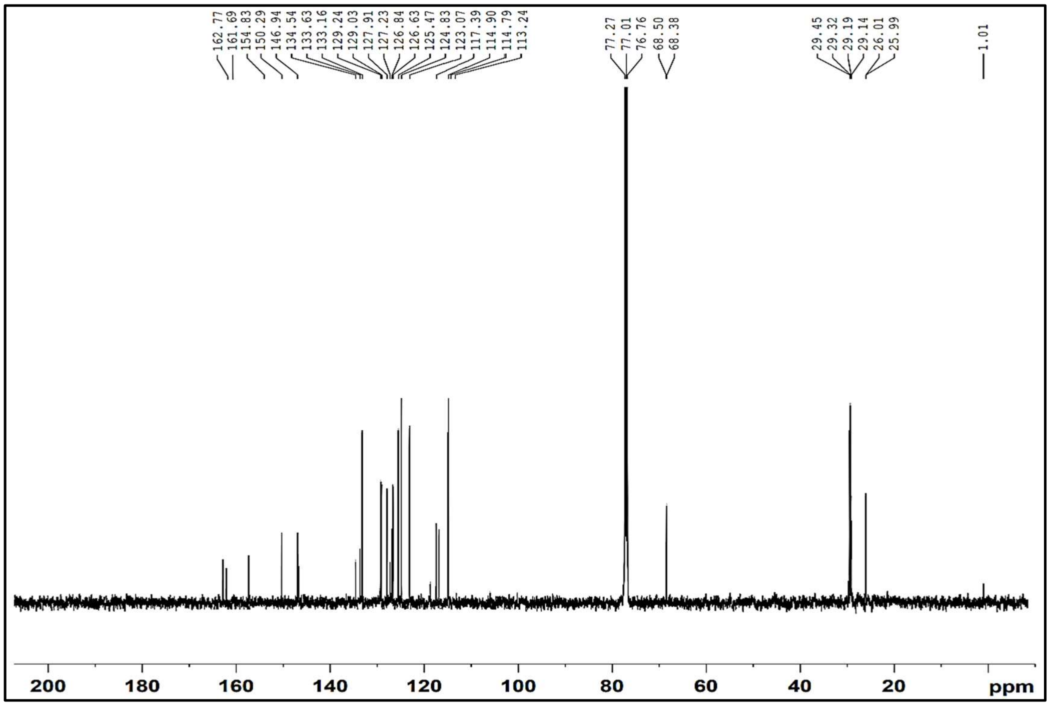

Fig. S3.21: ^{13}C-NMR spectra of *III-10*

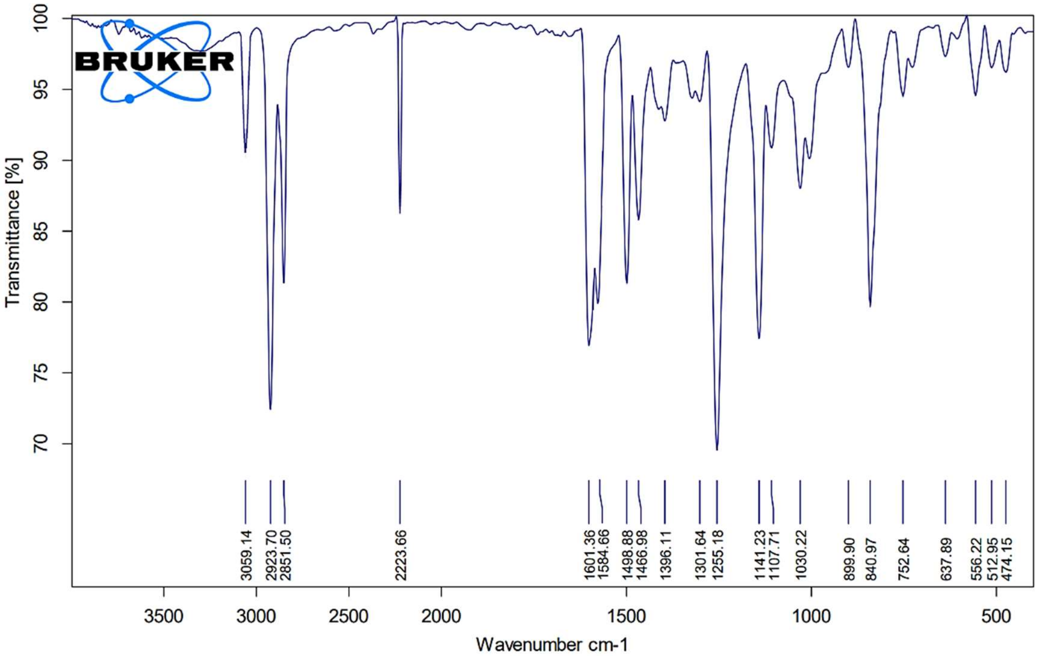

Fig. S3.22: FT-IR spectra of *III-12*

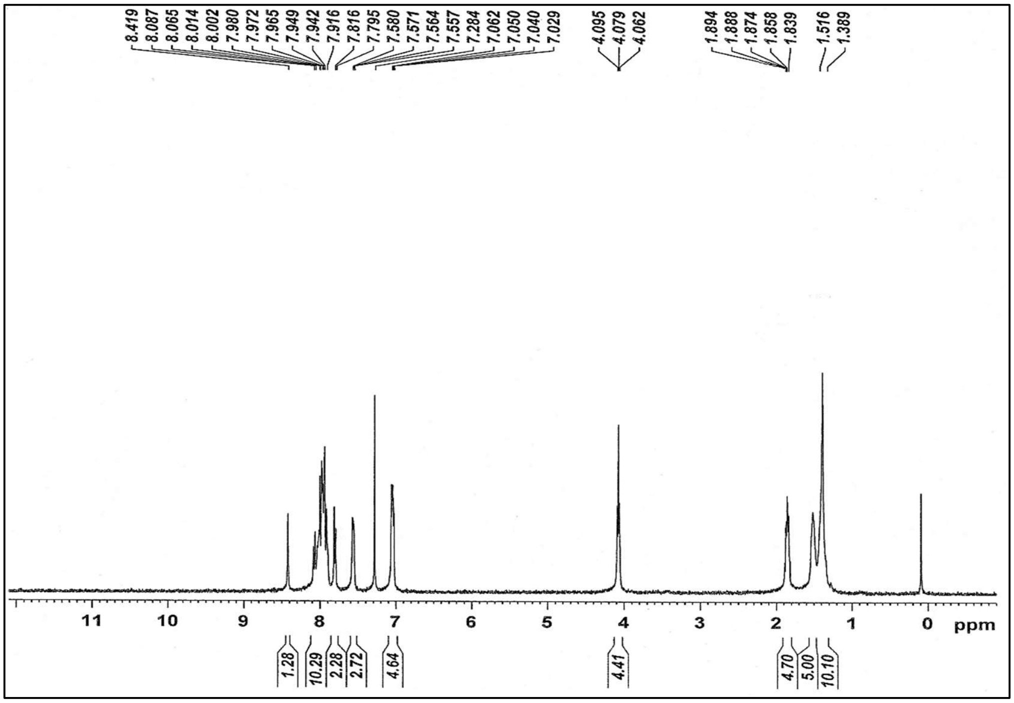

Fig. S3.23: ^{1}H-NMR spectra of *III-12*

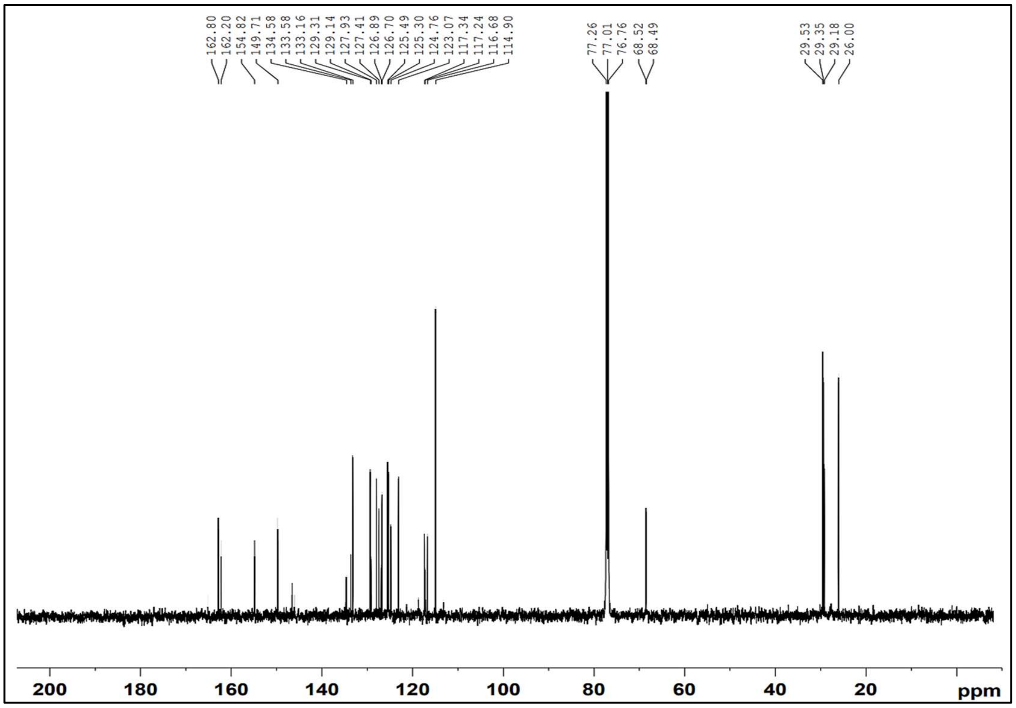

Fig. S3.24: ^{13}C-NMR spectra of *III-12*

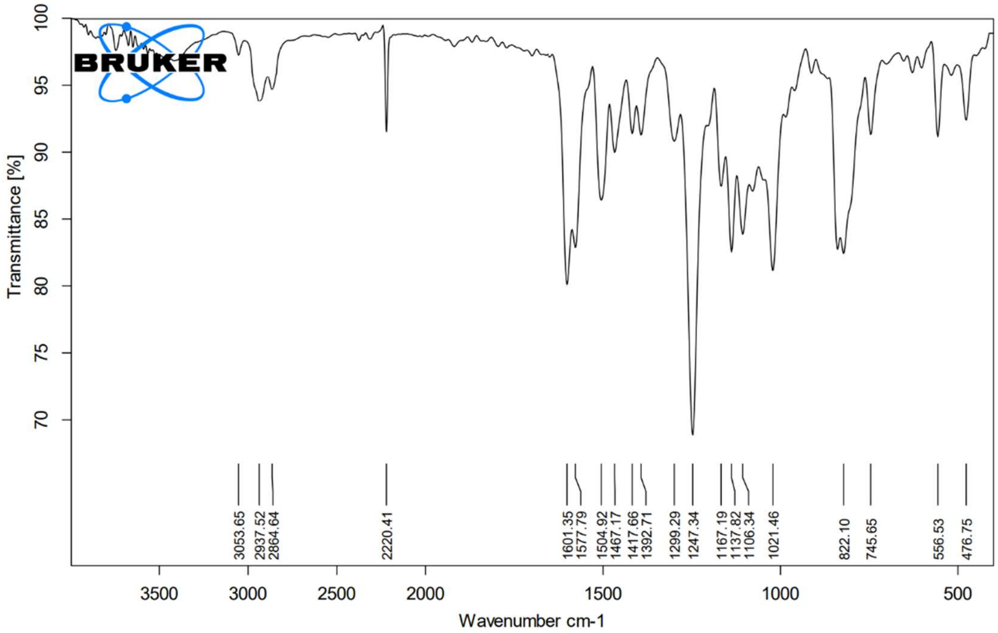

Fig. S3.25: FT-IR spectra of *IV-2*

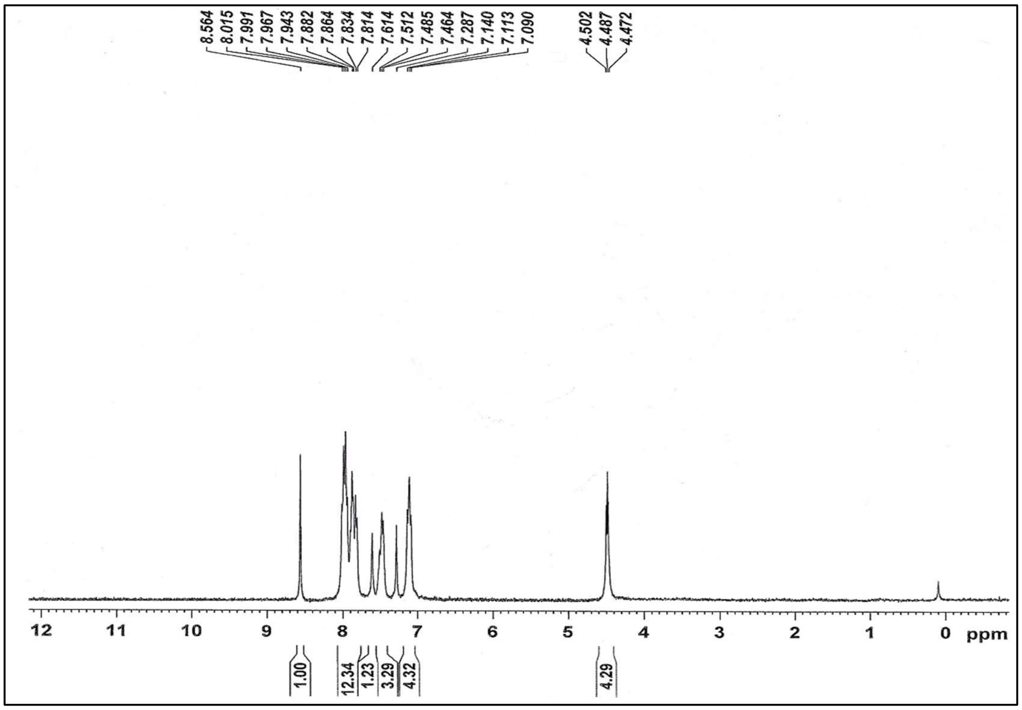

Fig. S3.26: ^{1}H-NMR spectra of *IV-2*

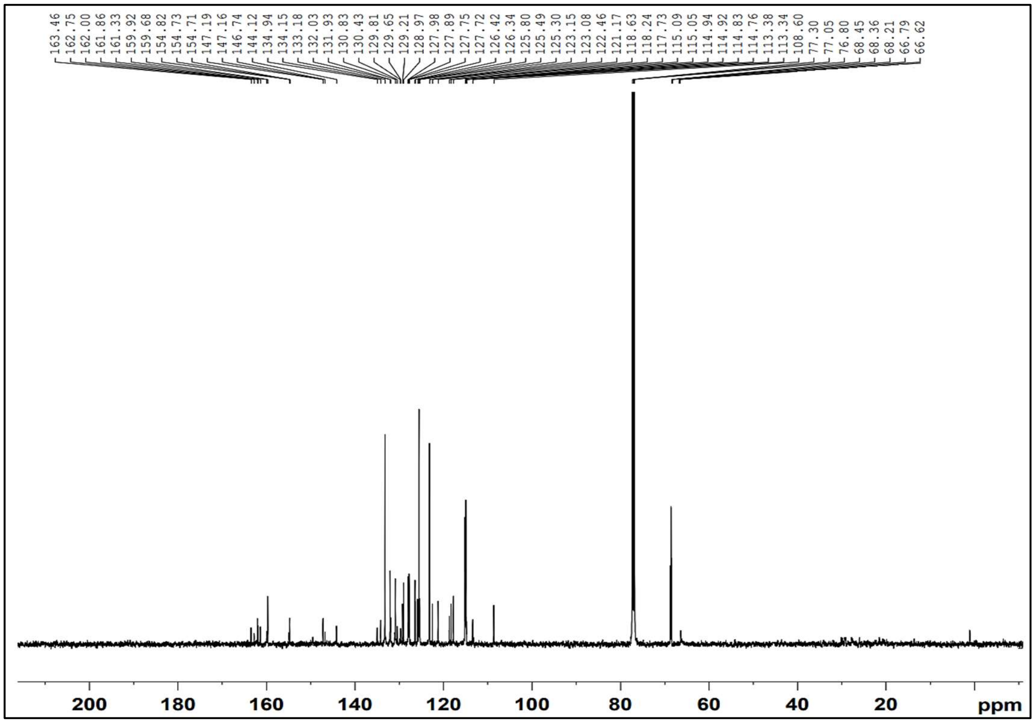

Fig. S3.27: ^{13}C-NMR spectra of *IV-2*

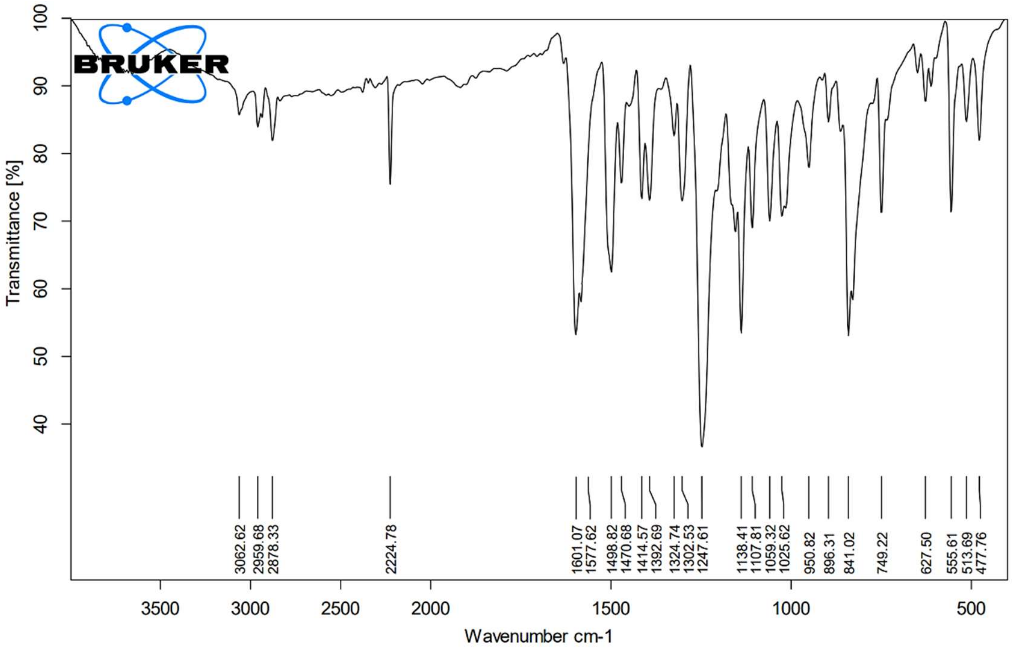

Fig. S3.28: FT-IR spectra of *IV-3*

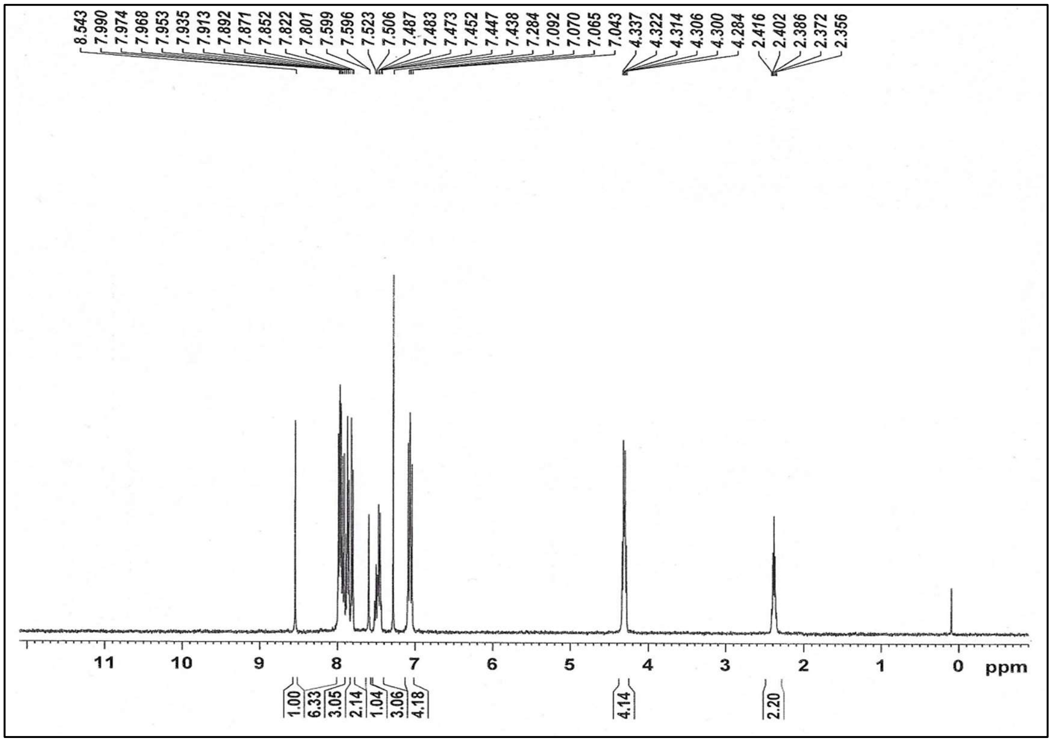

Fig. S3.29: ^{1}H-NMR spectra of *IV-3*

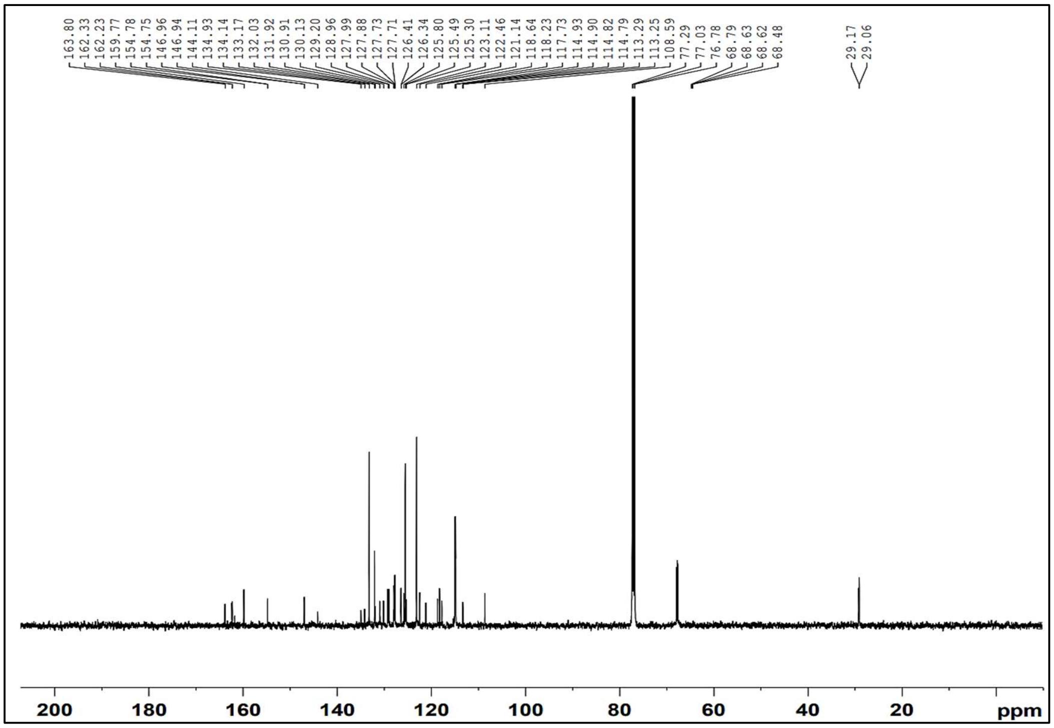

Fig. S3.30: ^{13}C-NMR spectra of *IV-3*

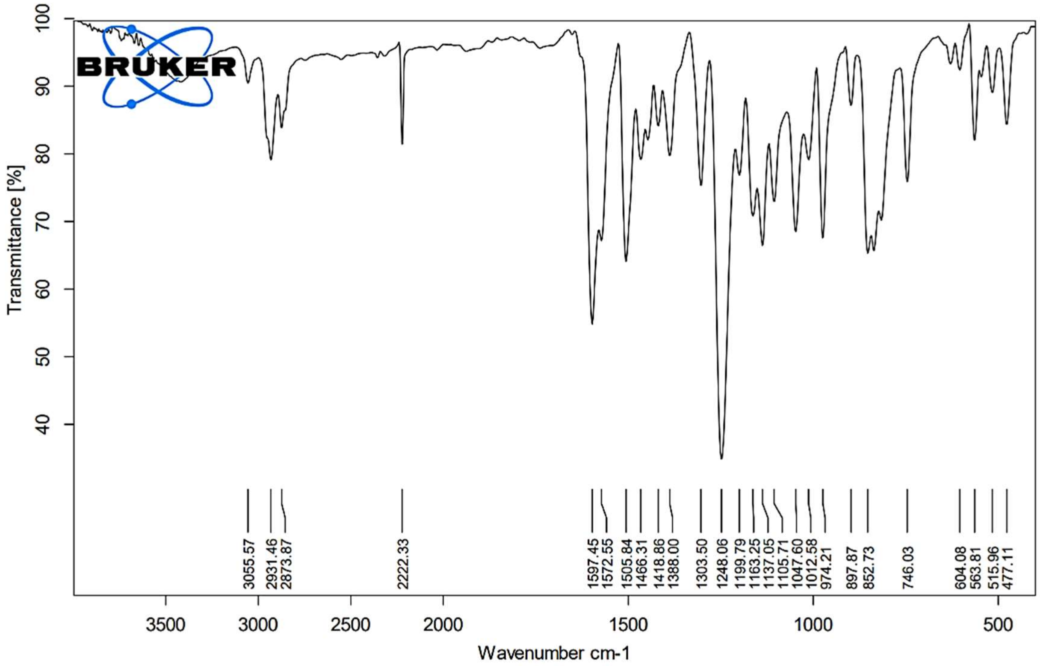

Fig. S3.31 FT-IR spectra of *IV-4*

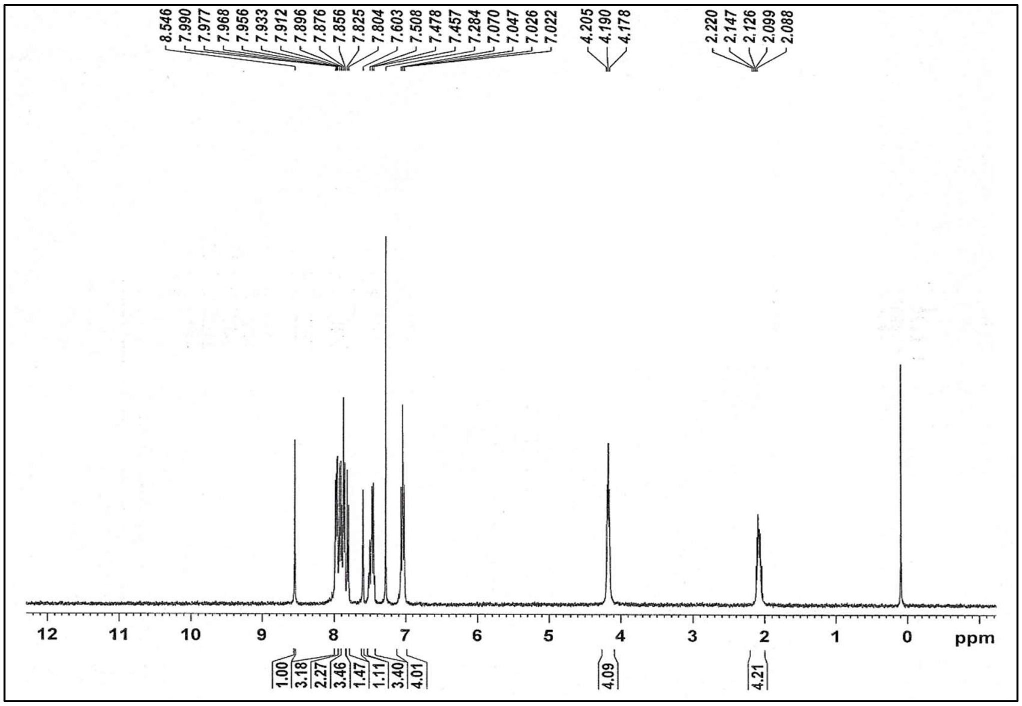

Fig. S3.32: ^{1}H-NMR spectra of *IV-4*

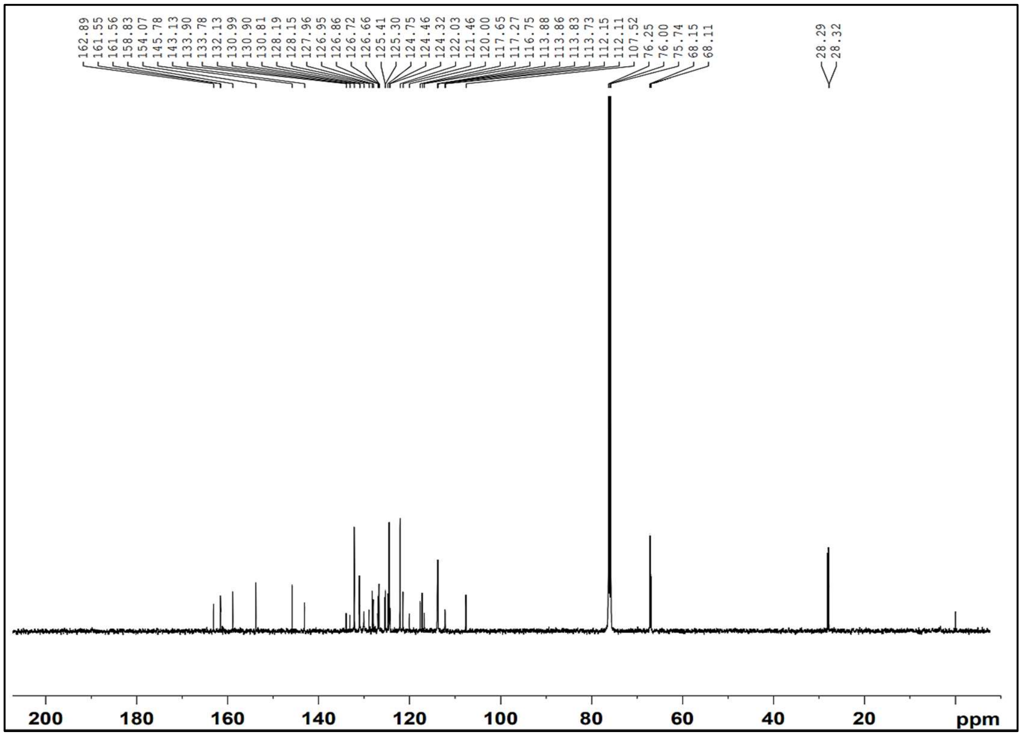

Fig. S3.33 ^{13}C-NMR spectra of *IV-4*

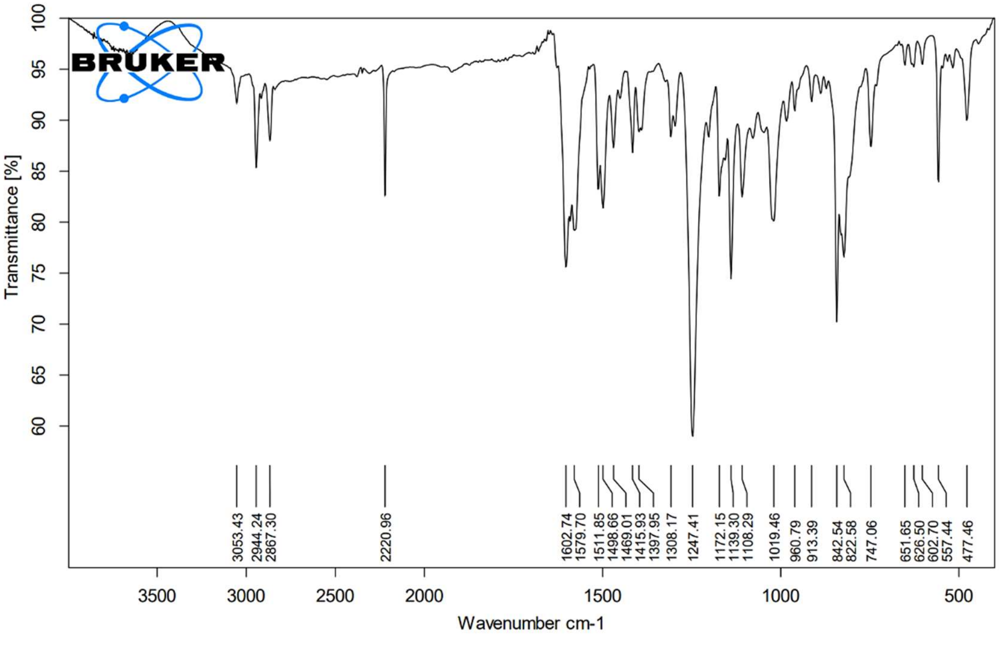

Fig. S3.34: FT-IR spectra of *IV-5*

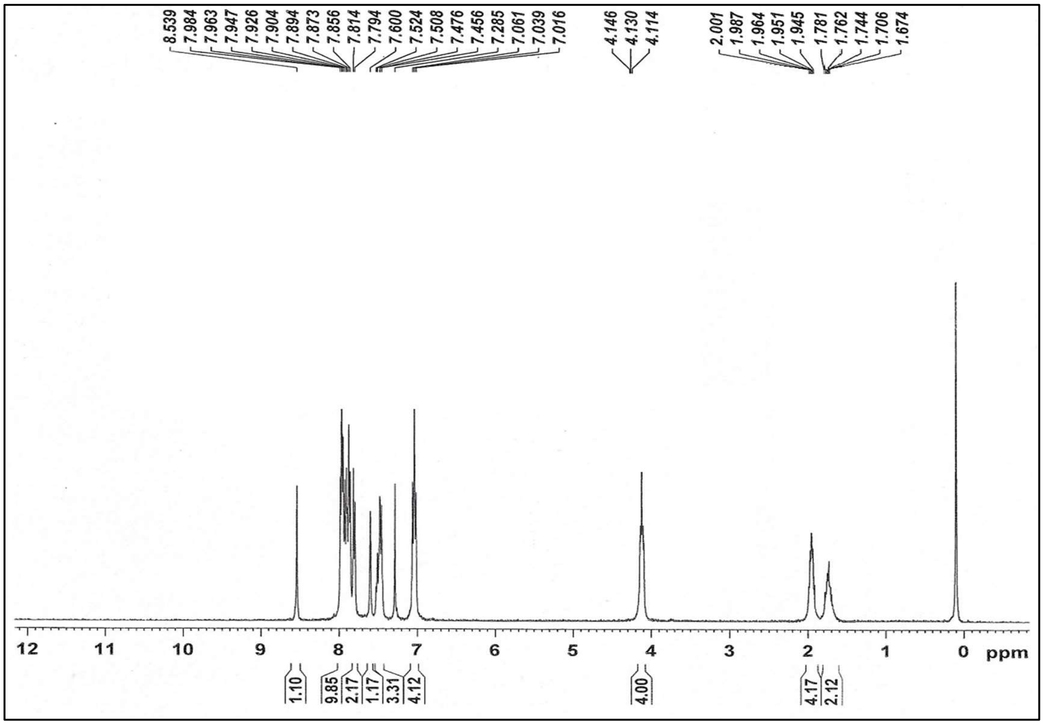

Fig. S3.35: ^{1}H-NMR spectra of *IV-5*

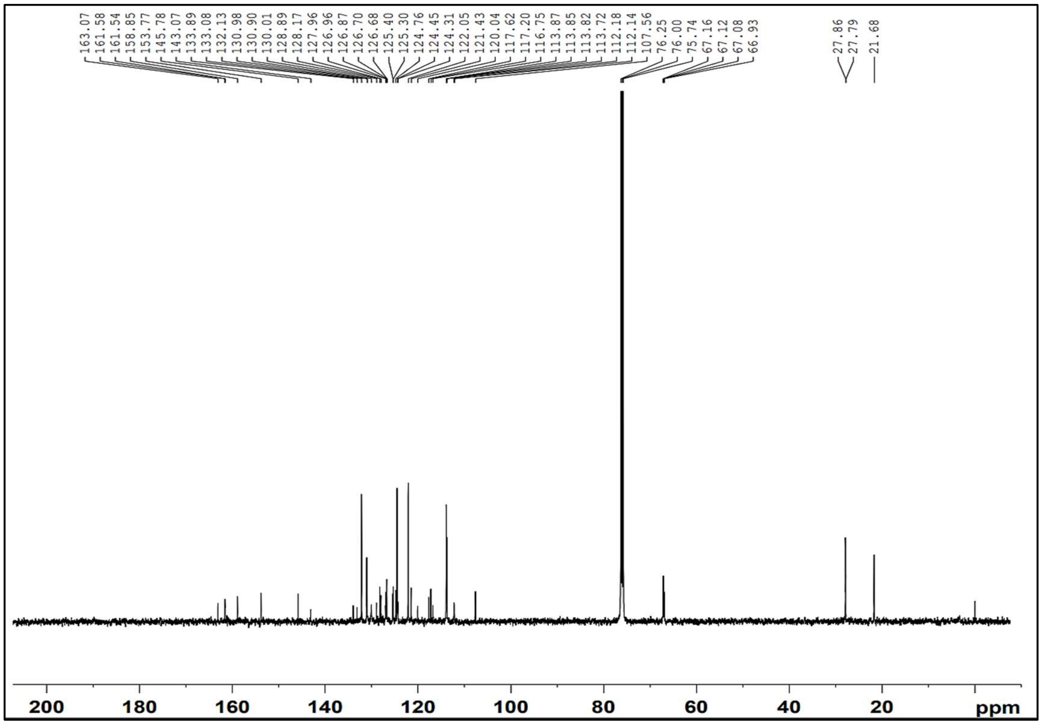

Fig. S3.36: ^{13}C-NMR spectra of *IV-5*

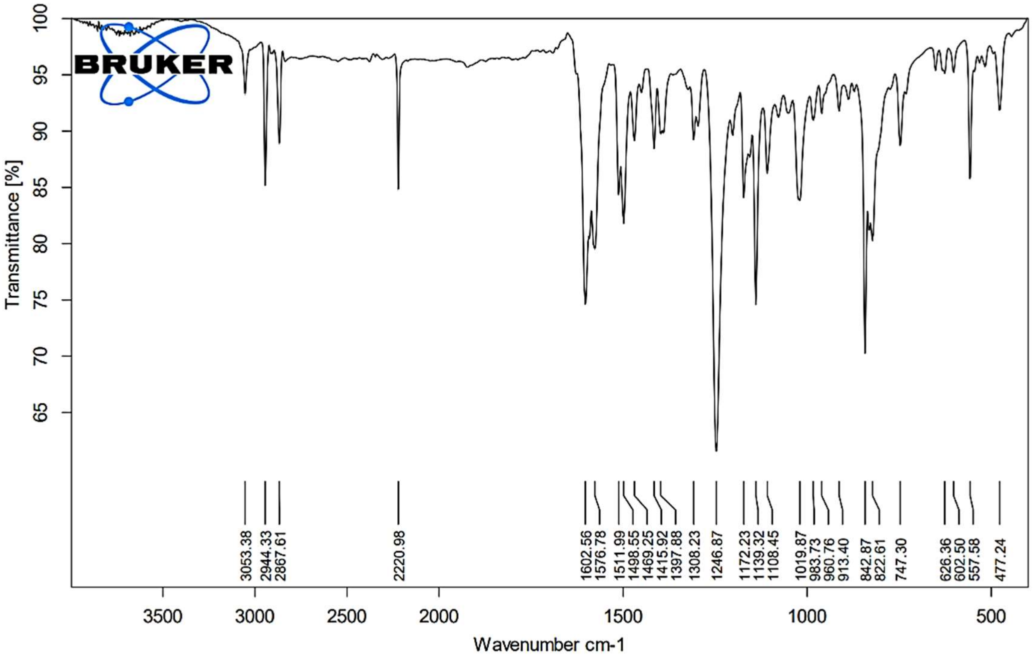

Fig. S3.37 FT-IR spectra of *IV-6*

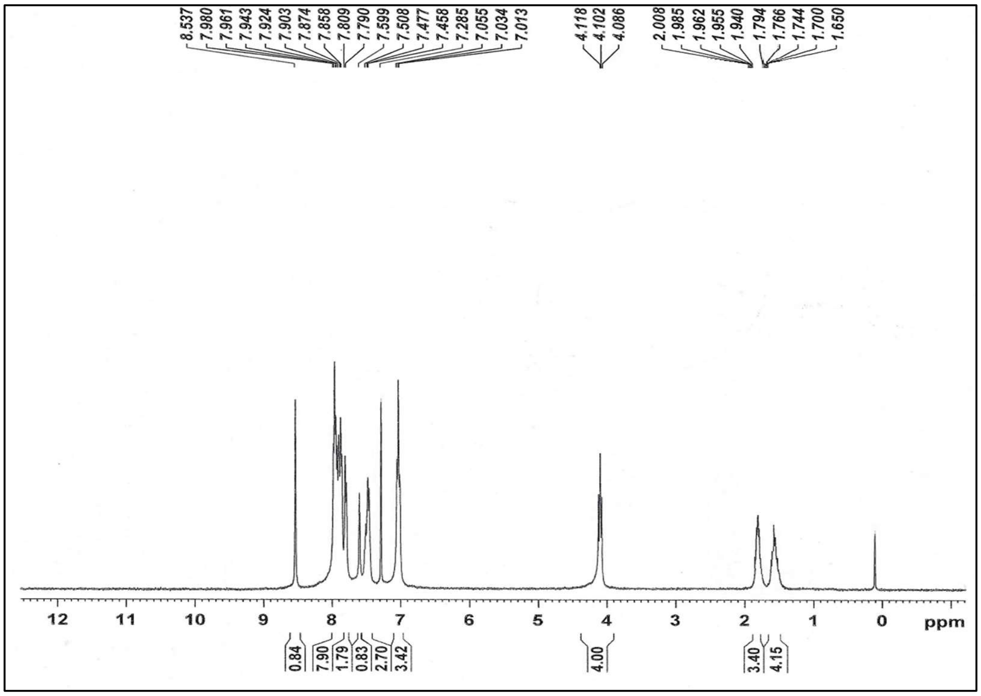

Fig. S3.38 ^{1}H-NMR spectra of *IV-6*

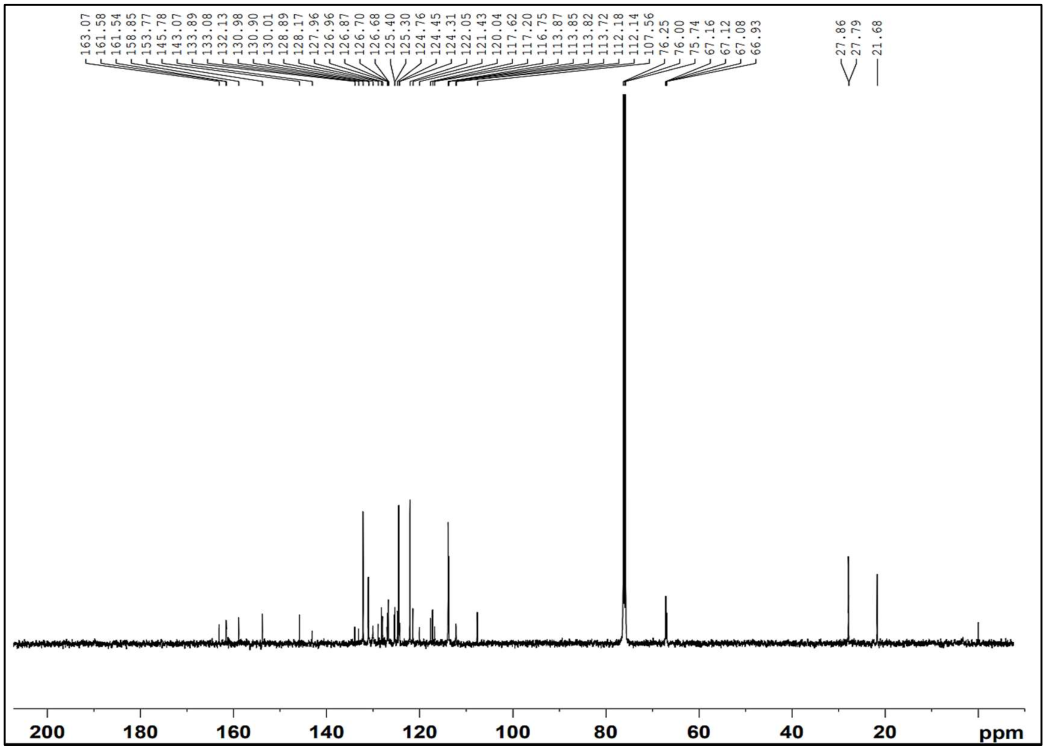

Fig. S3.39: ^{13}C-NMR spectra of *IV-6*

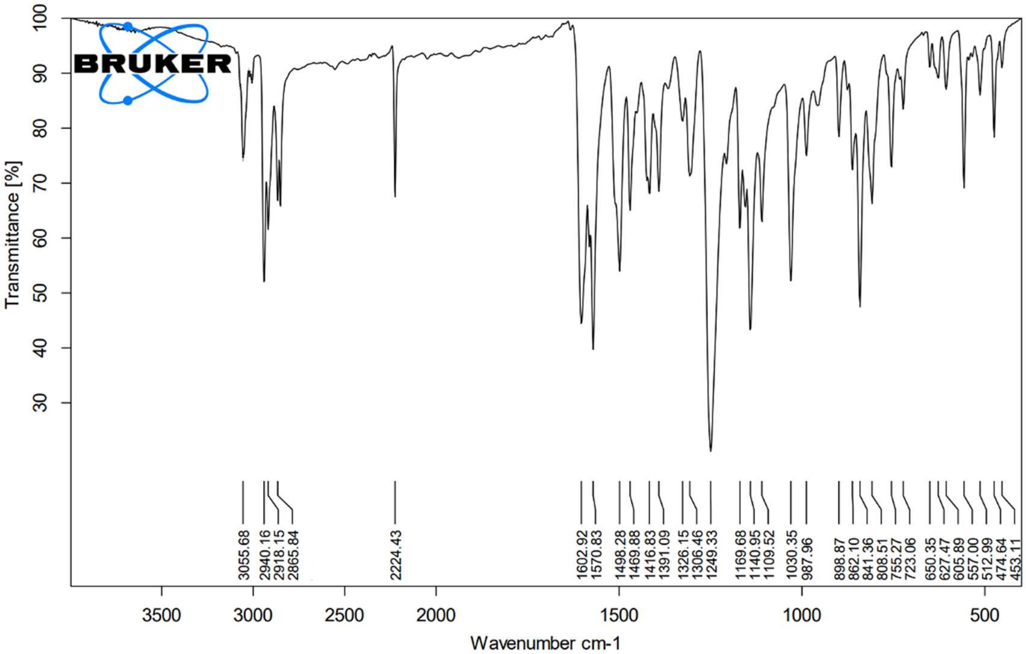

Fig. S3.40: FT-IR spectra of *IV-8*

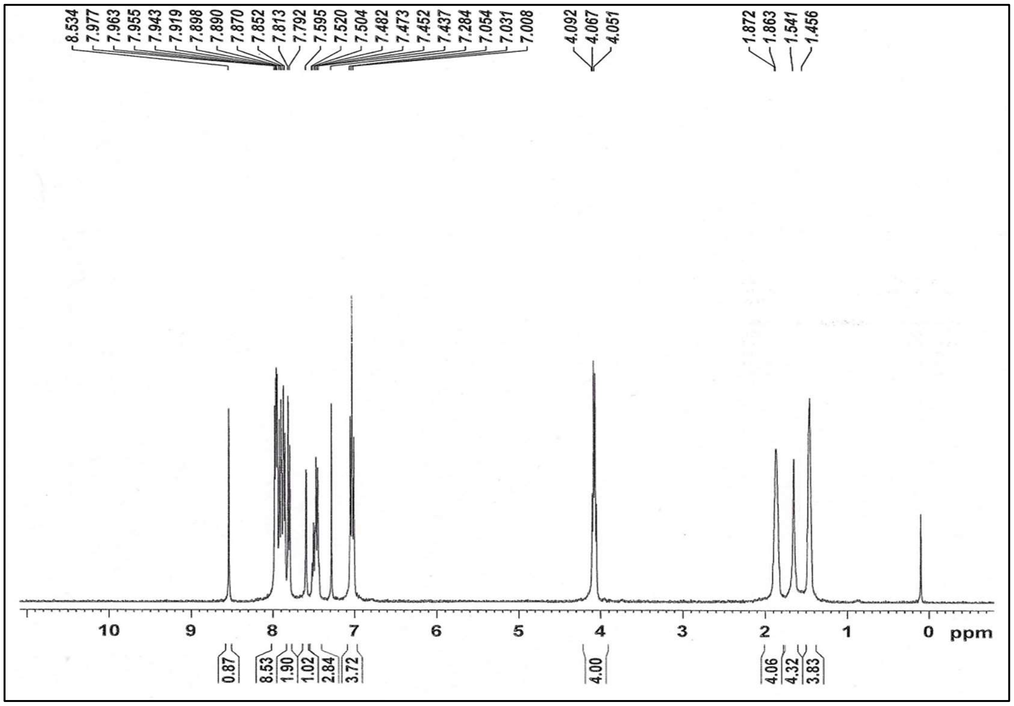

Fig. S3.41: ^{1}H-NMR spectra of *IV-8*

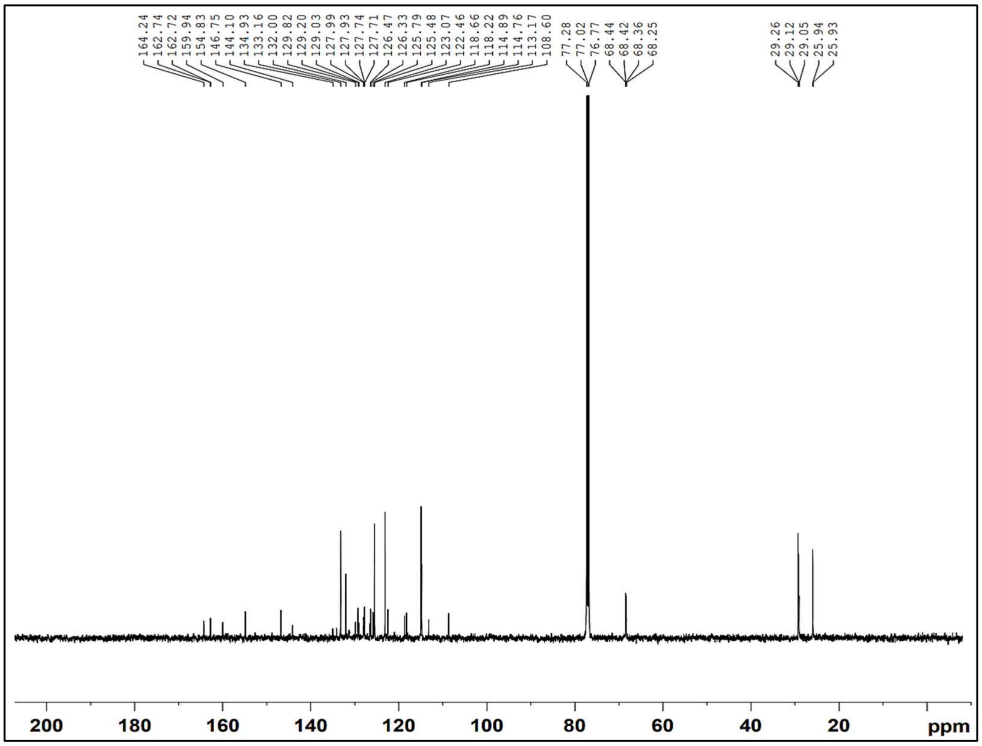

Fig. S3.42: ^{13}C-NMR spectra of *IV-8*

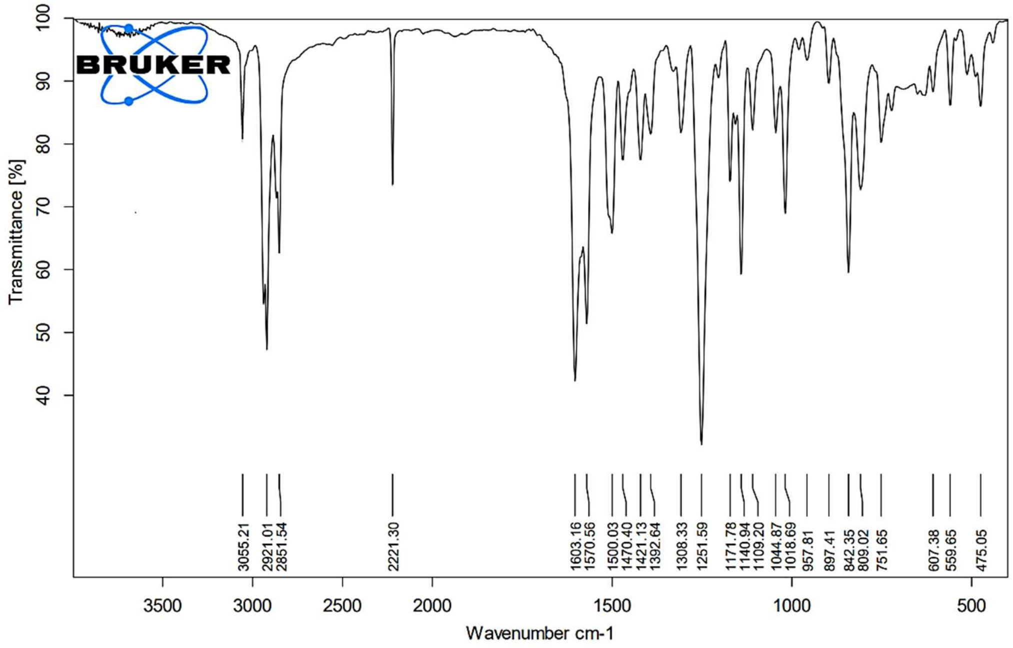

Fig. S3.43: FT-IR spectra of *IV-10*

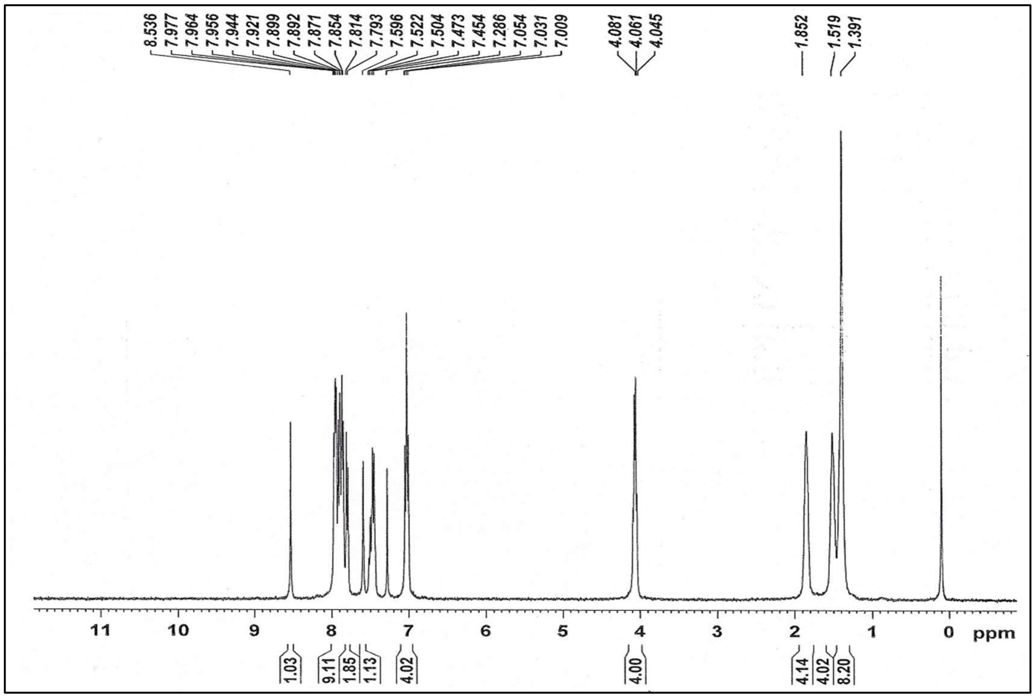

Fig. S3.44 ^{1}H-NMR spectra of *IV-10*

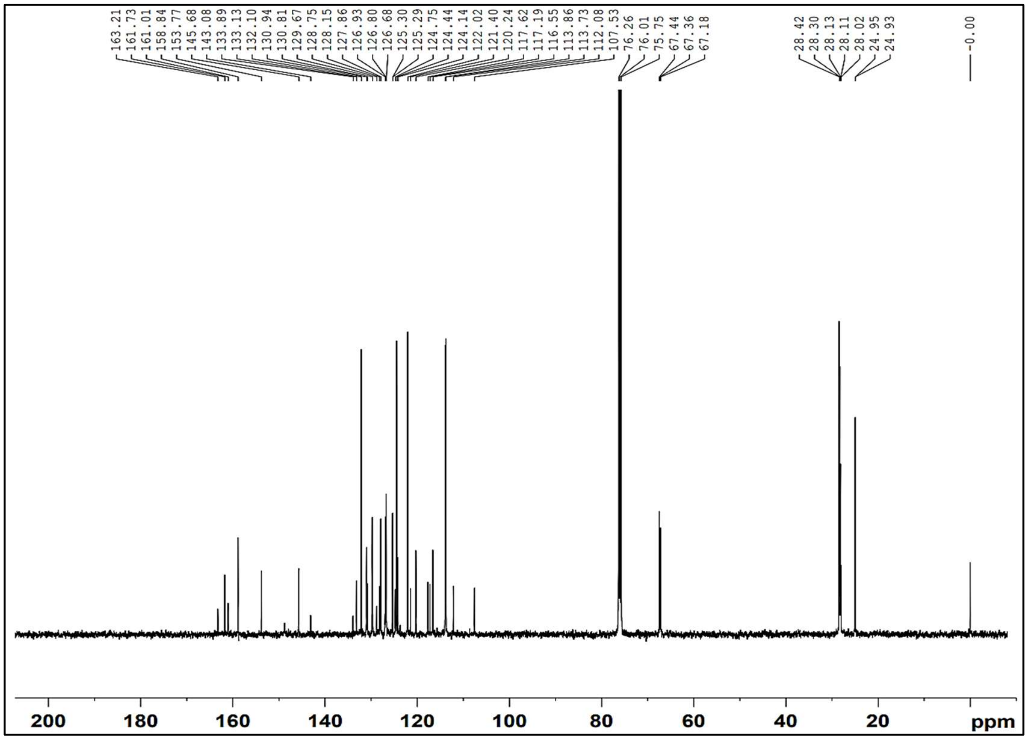

Fig. S3.45 ^{13}C-NMR spectra of *IV-10*

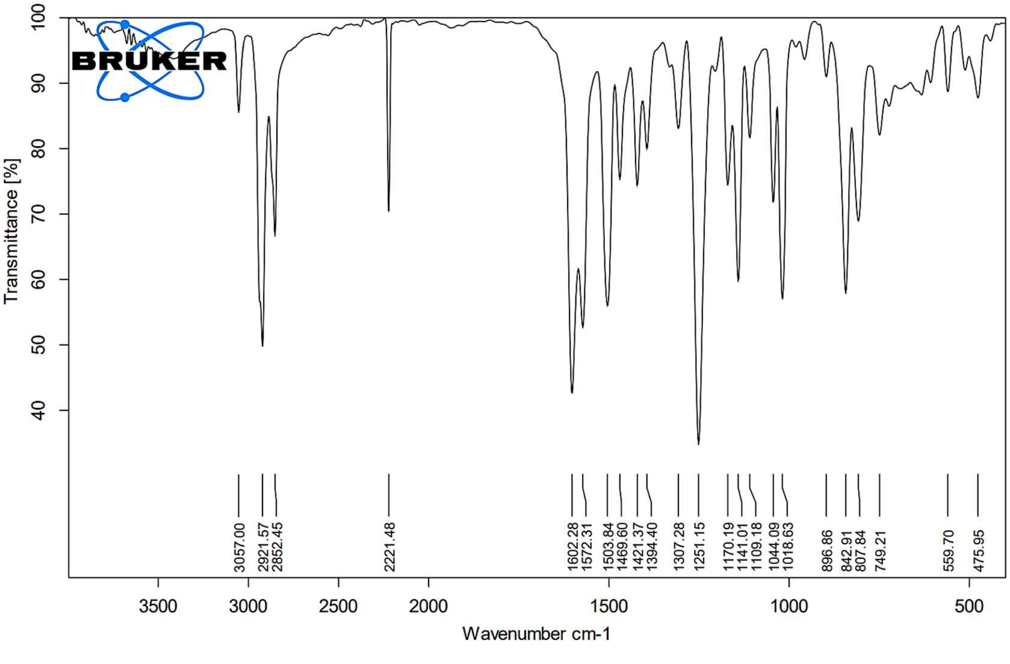

Fig. S3.46 FT-IR spectra of *IV-12*

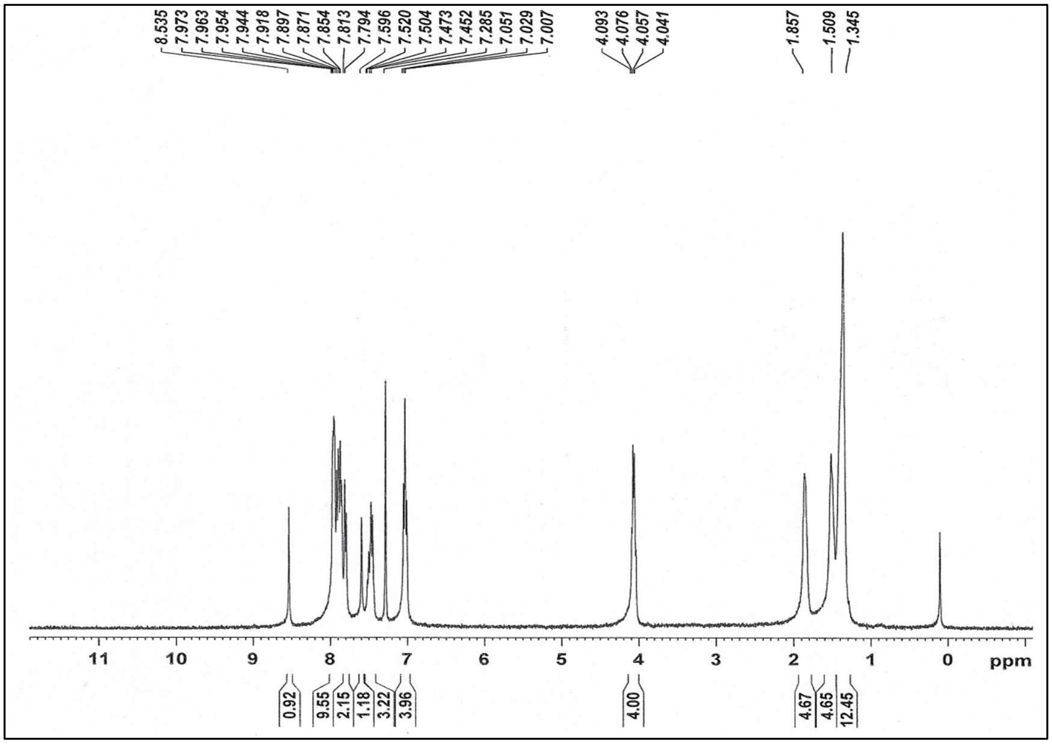

Fig. S3.47 ^{1}H-NMR spectra of *IV-12*

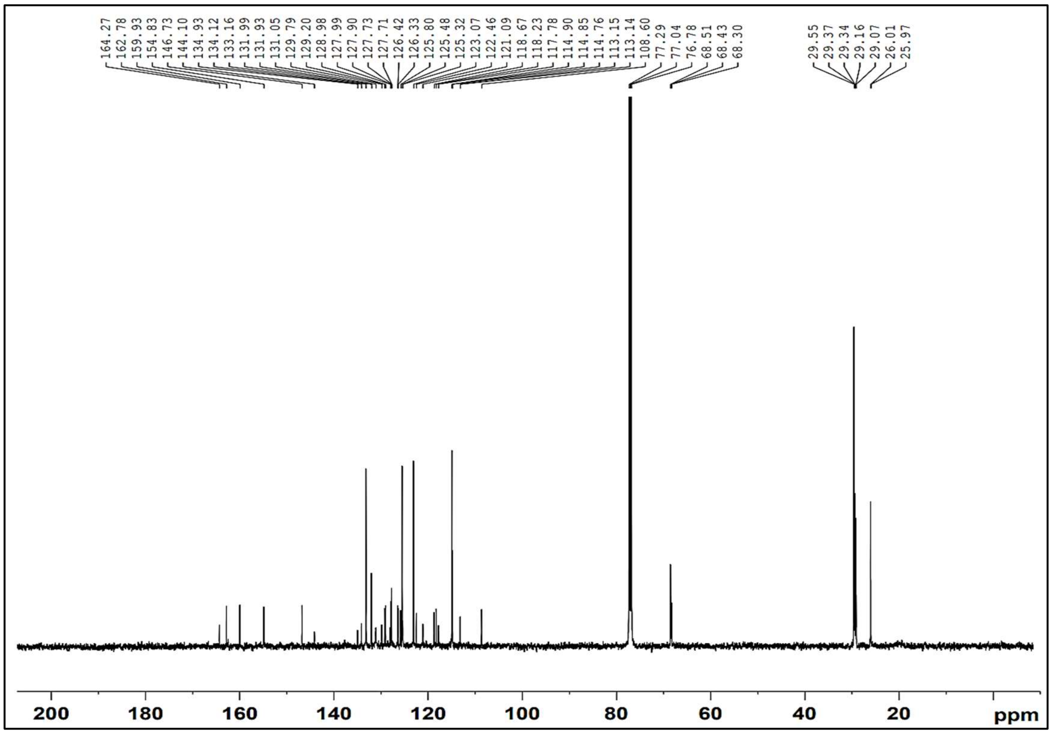

Fig. S3.48: ^{13}C-NMR spectra of *IV-12*

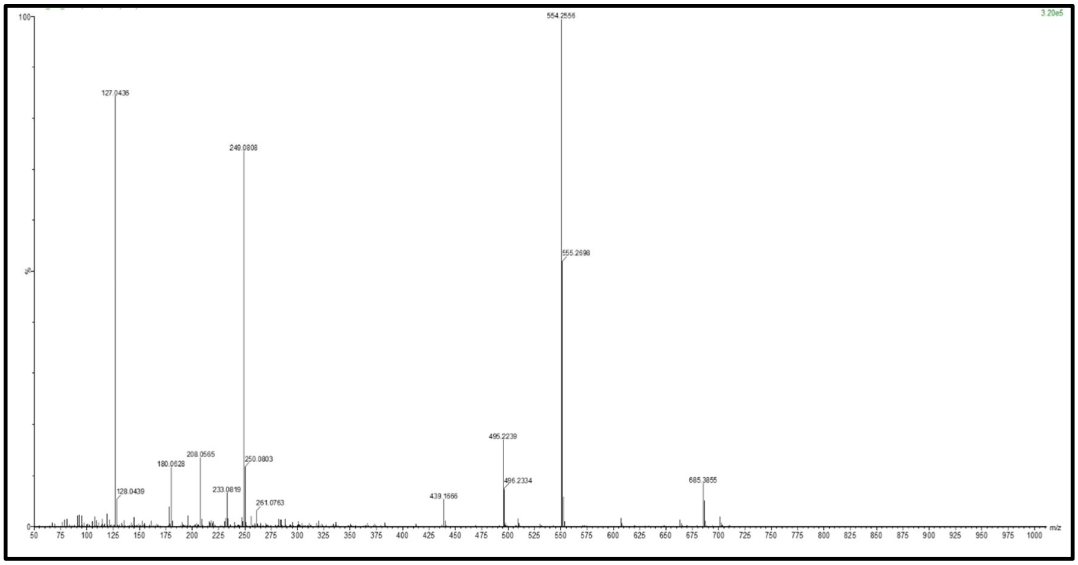

Fig. S3.49: Mass spectra of *III-6*

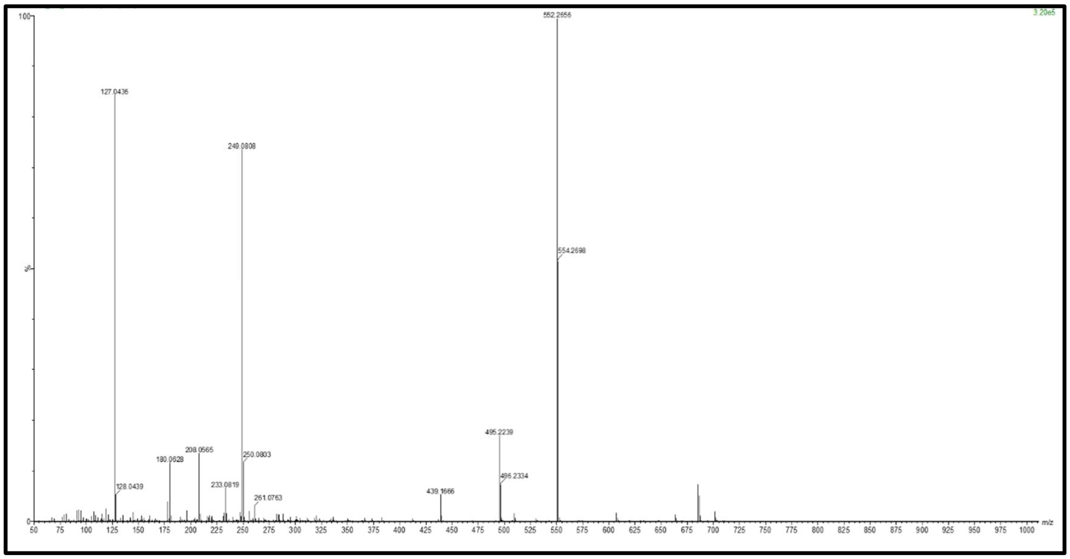

Fig. S3.50: Mass spectra of *IV-6*

3.7 DSC thermograms of the prepared dimers

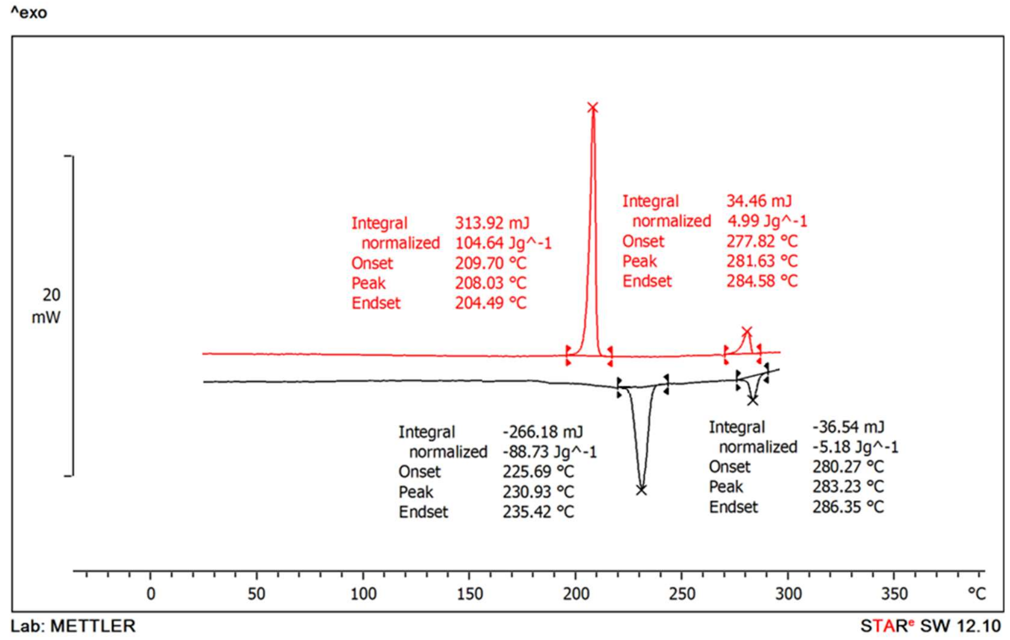

Fig. S3.51: DSC thermogram of *III-2*

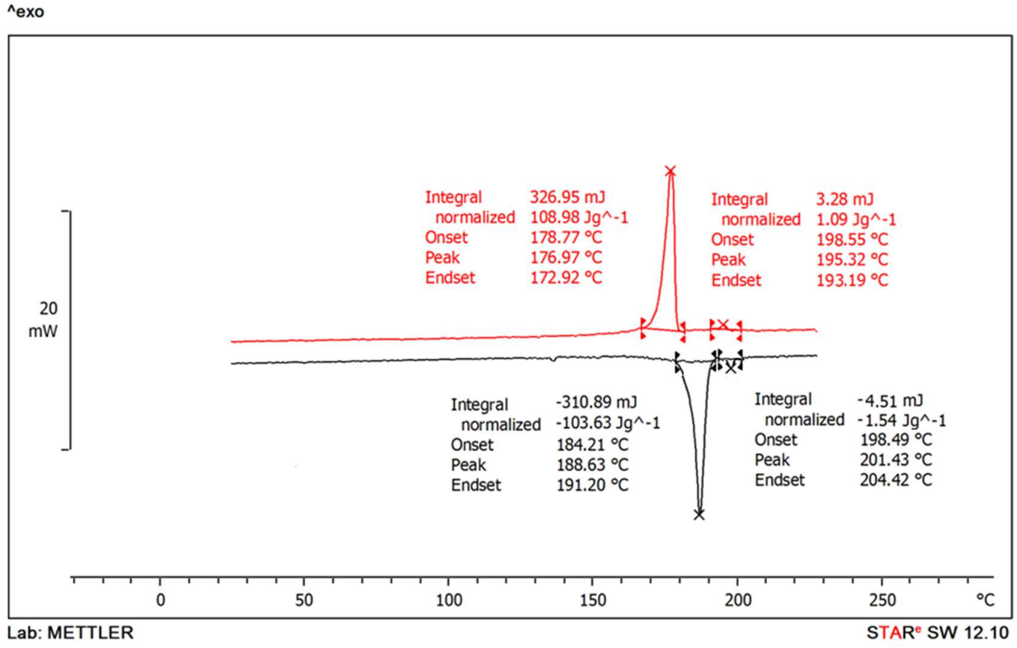

Fig. S3.52: DSC thermogram of *III-3*

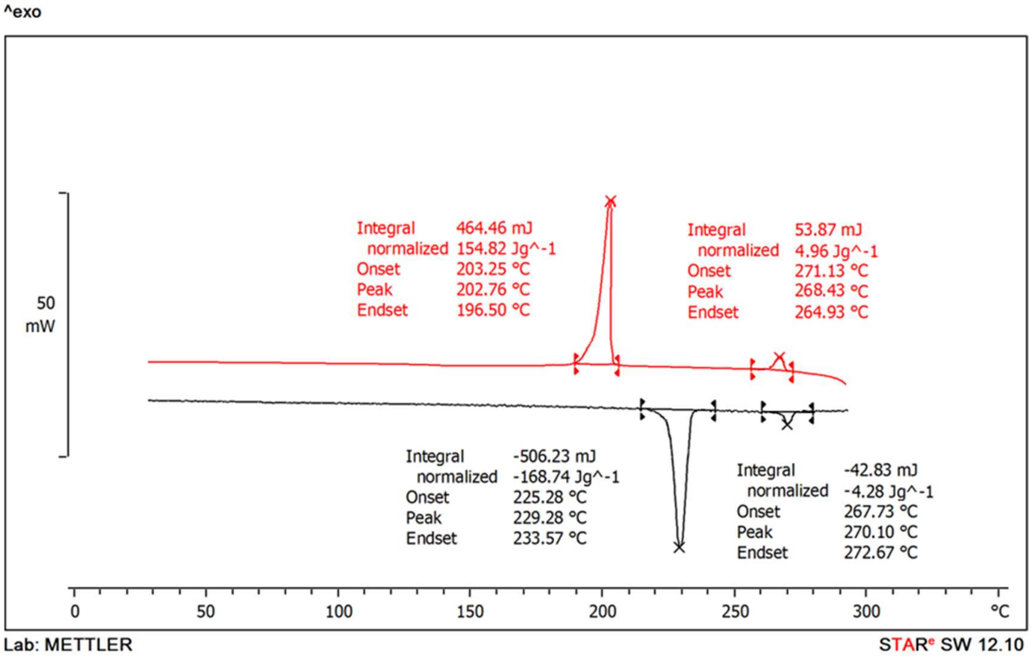

Fig. S3.53: DSC thermogram of *III-4*

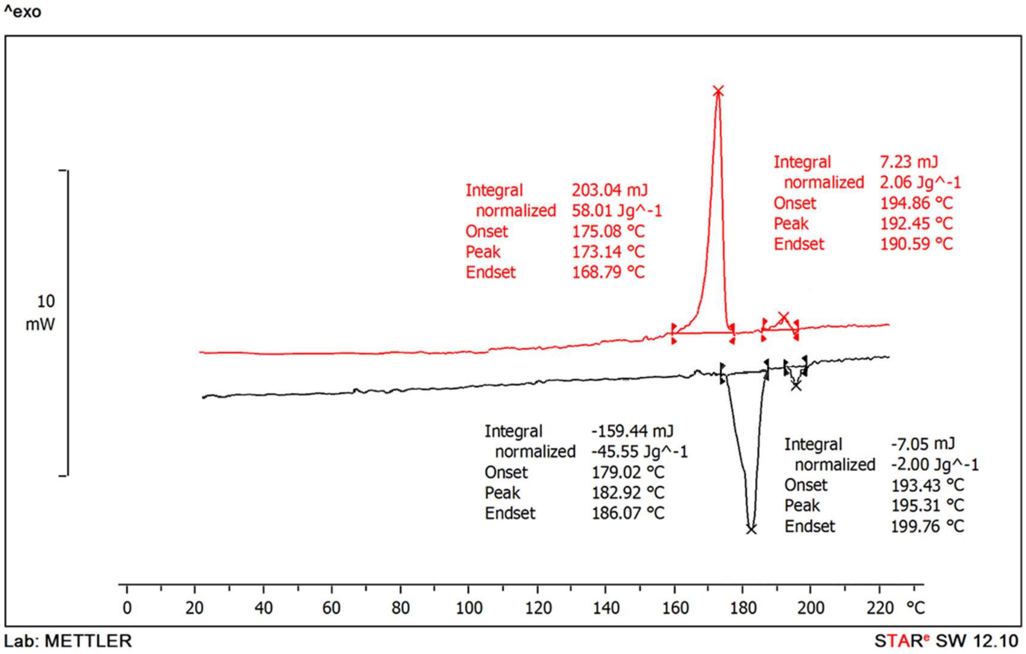

Fig. S3.54: DSC thermogram of *III-5*

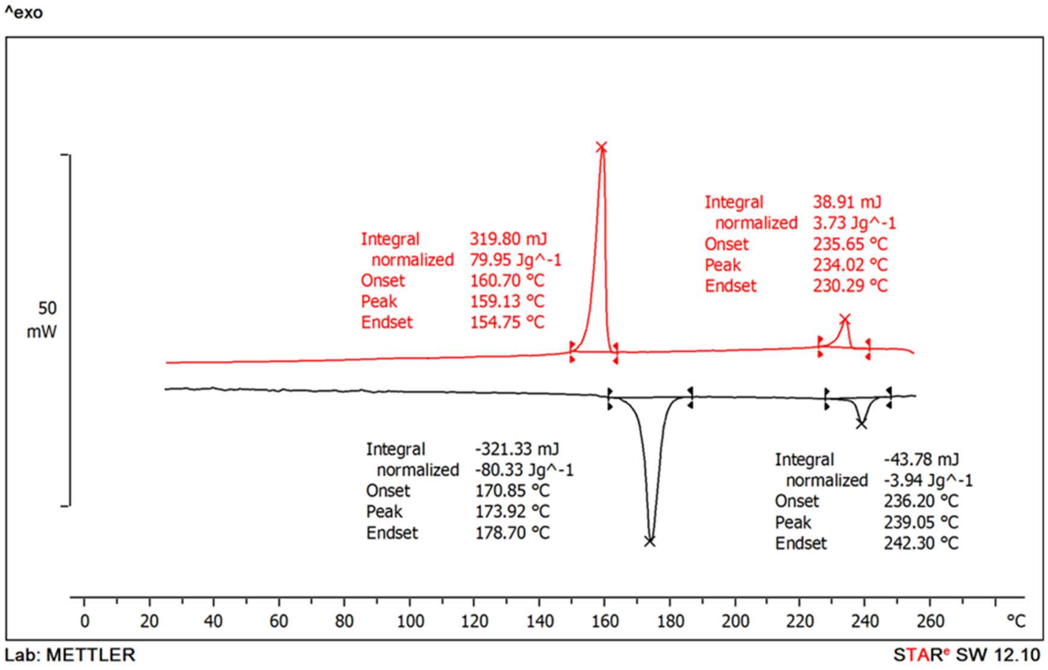

Fig. S3.55: DSC thermogram of *III-6*

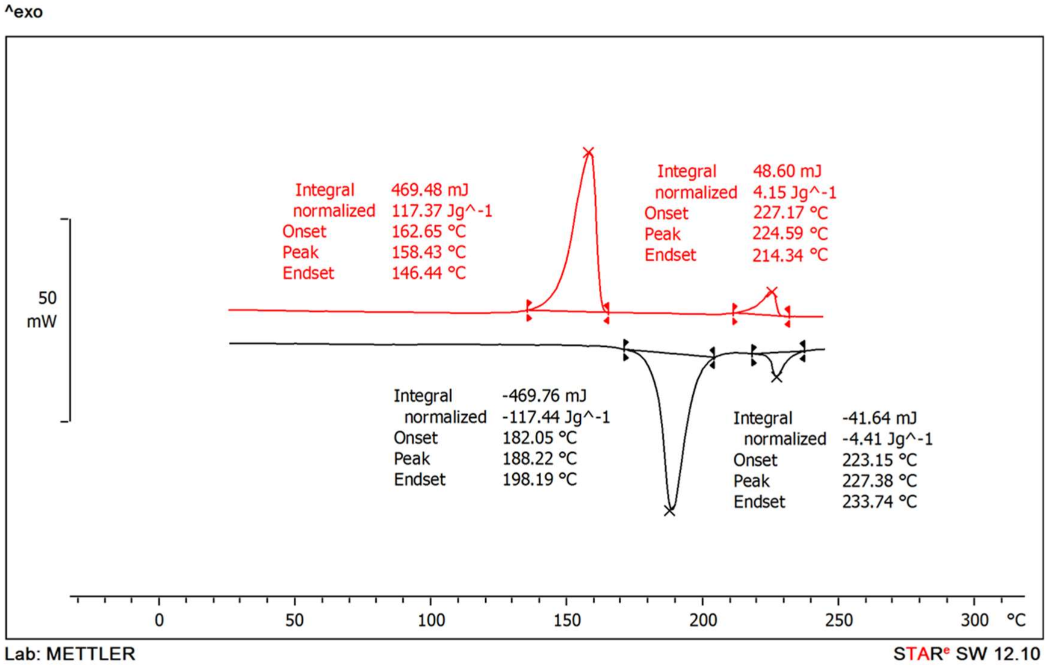

Fig. S3.56: DSC thermogram of *III-8*

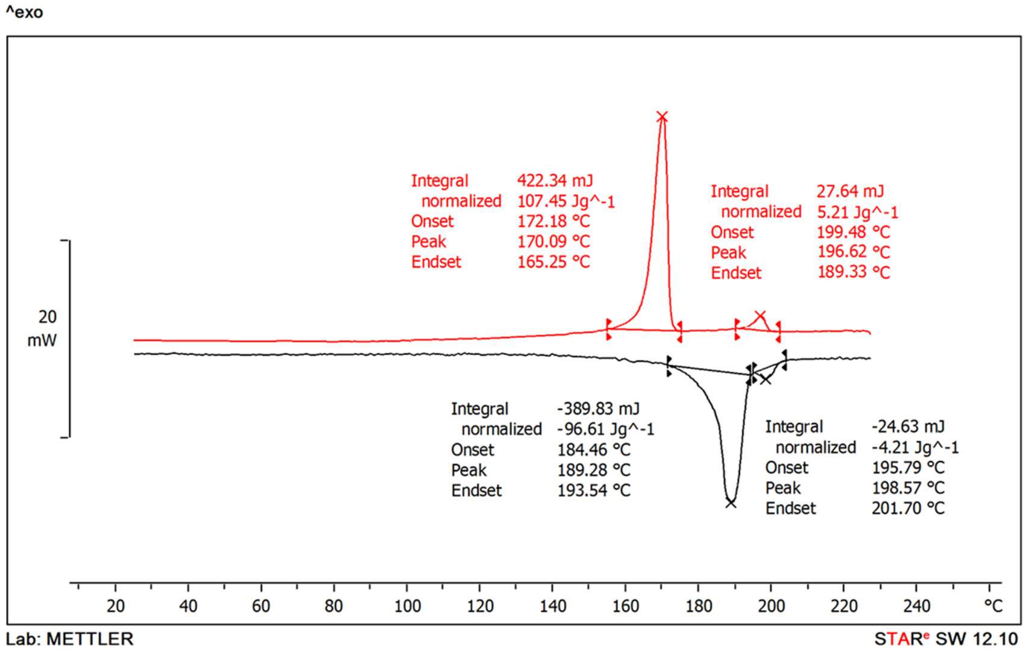

Fig. S3.57: DSC thermogram of *III-10*

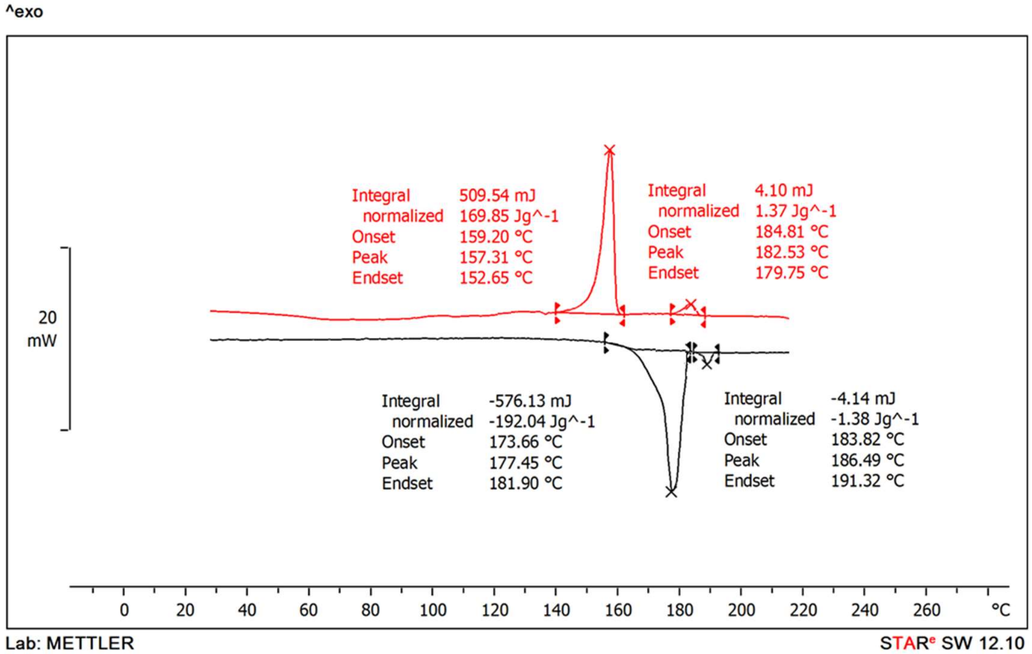

Fig. S3.58: DSC thermogram of *III-12*

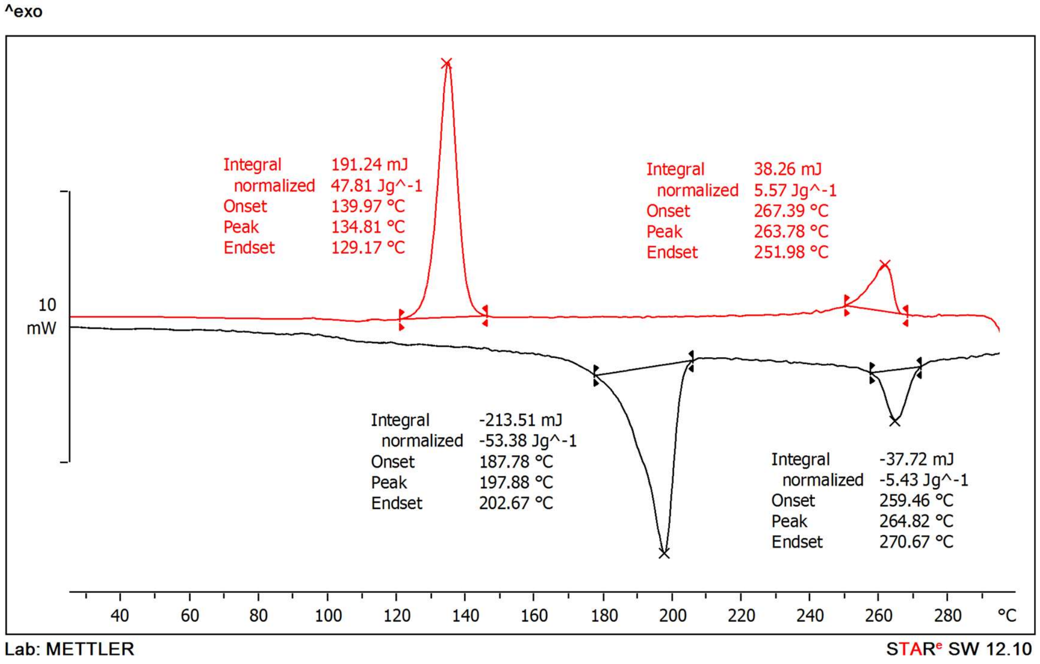

Fig. S3.59: DSC thermogram of *IV-2*

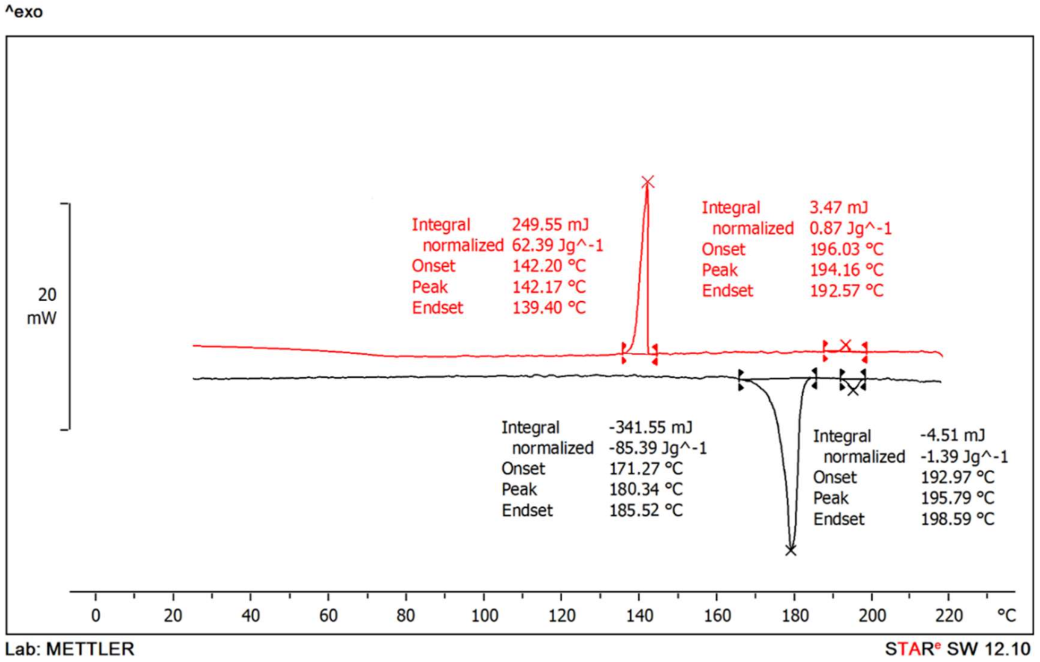

Fig. S3.60: DSC thermogram of *IV-3*

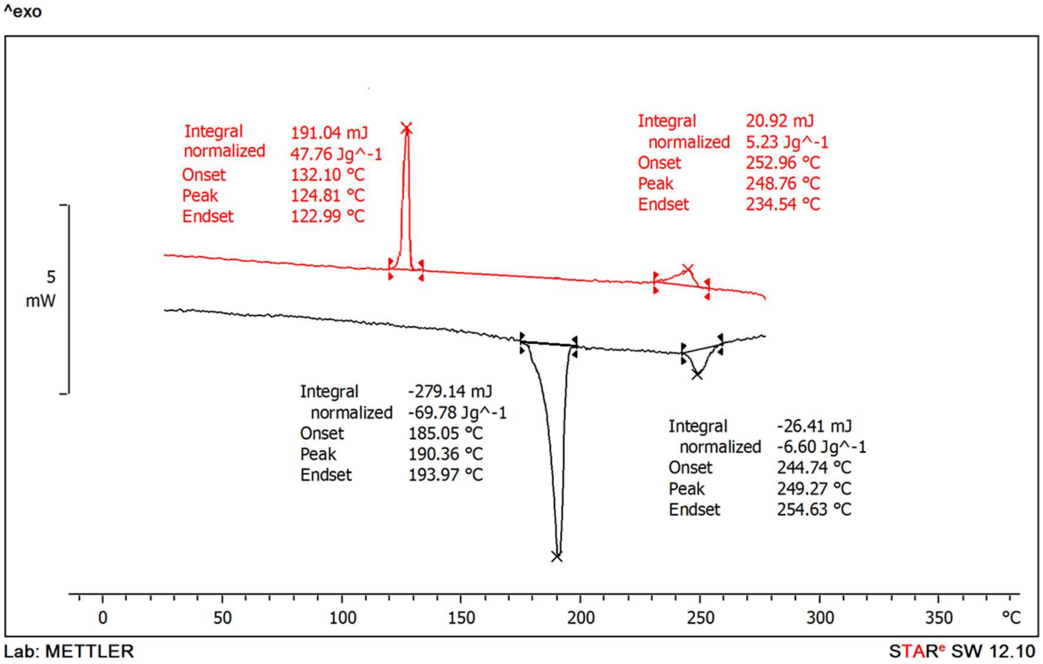

Fig. S3.61: DSC thermogram of *IV-4*

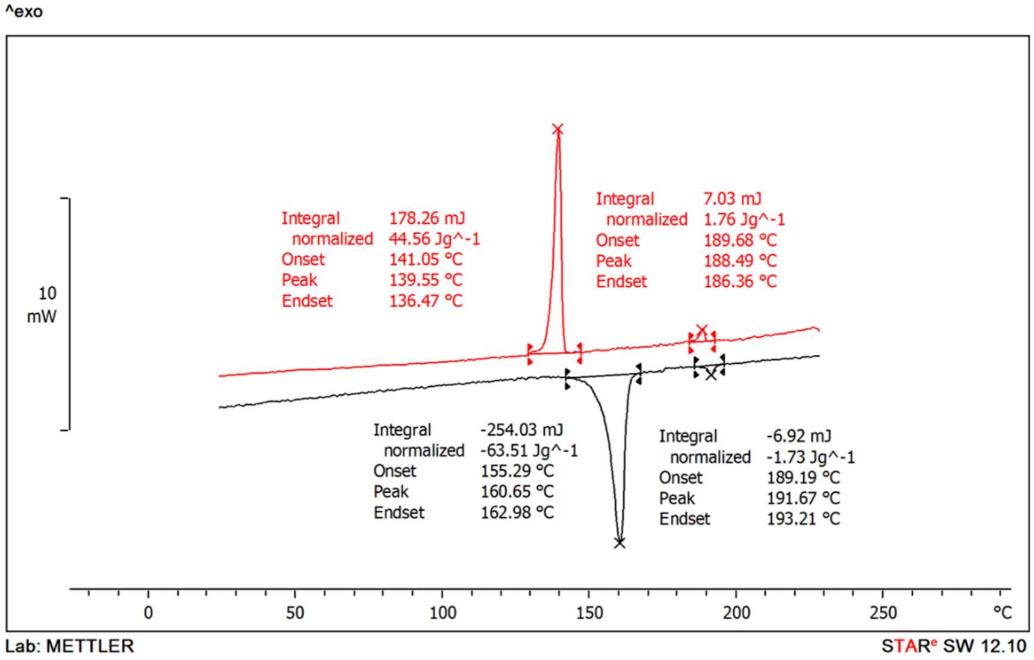

Fig. S3.62: DSC thermogram of *IV-5*

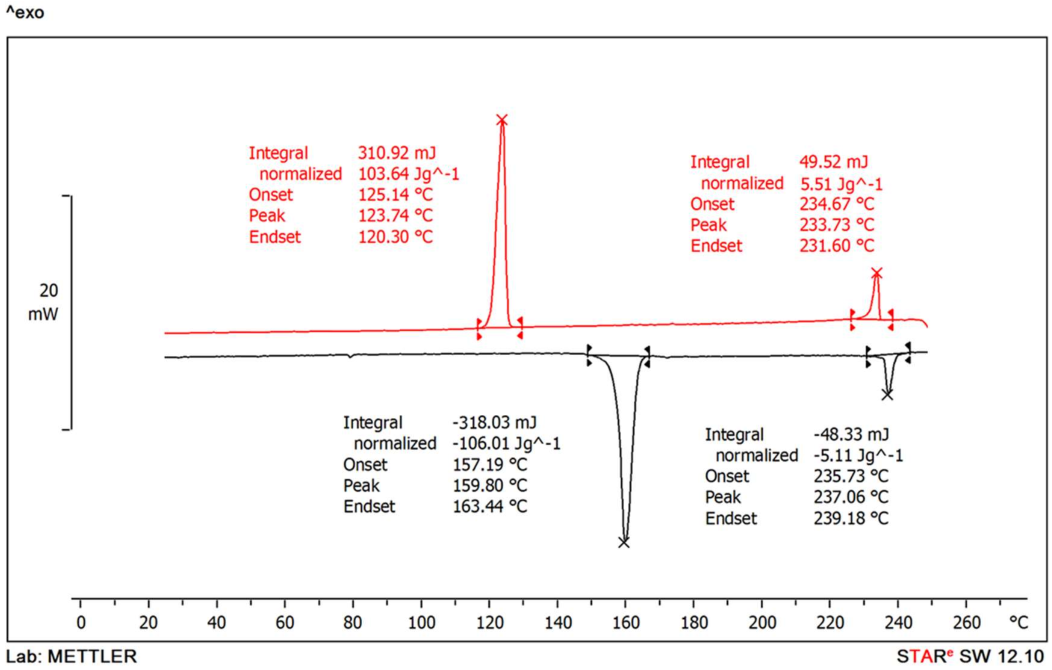

Fig. S3.63: DSC thermogram of *IV-6*

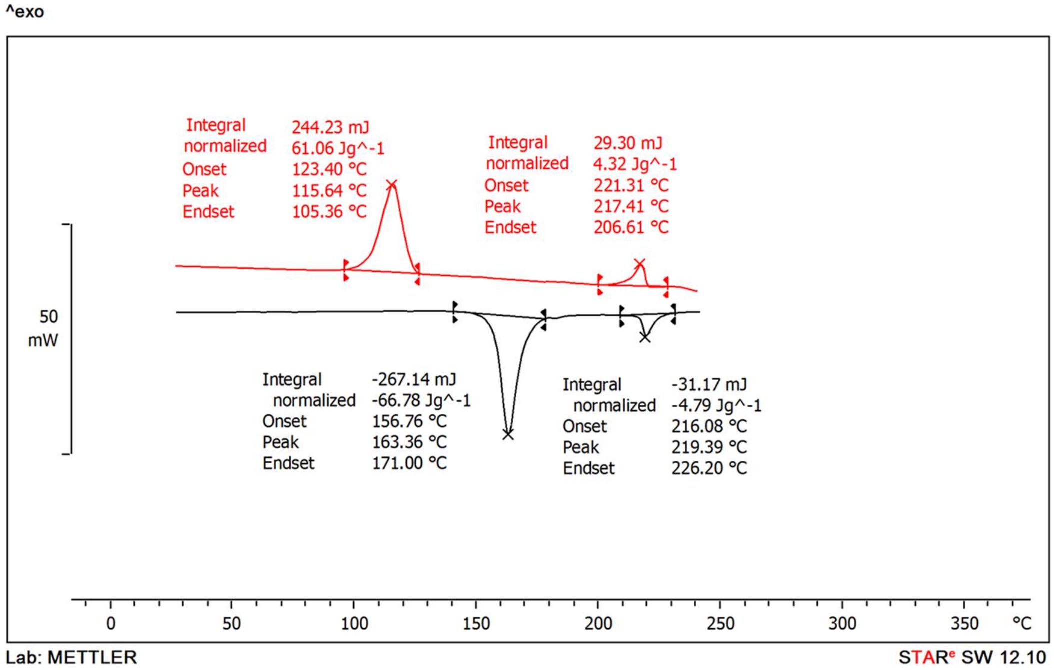

Fig. S3.64: DSC thermogram of *IV-8*

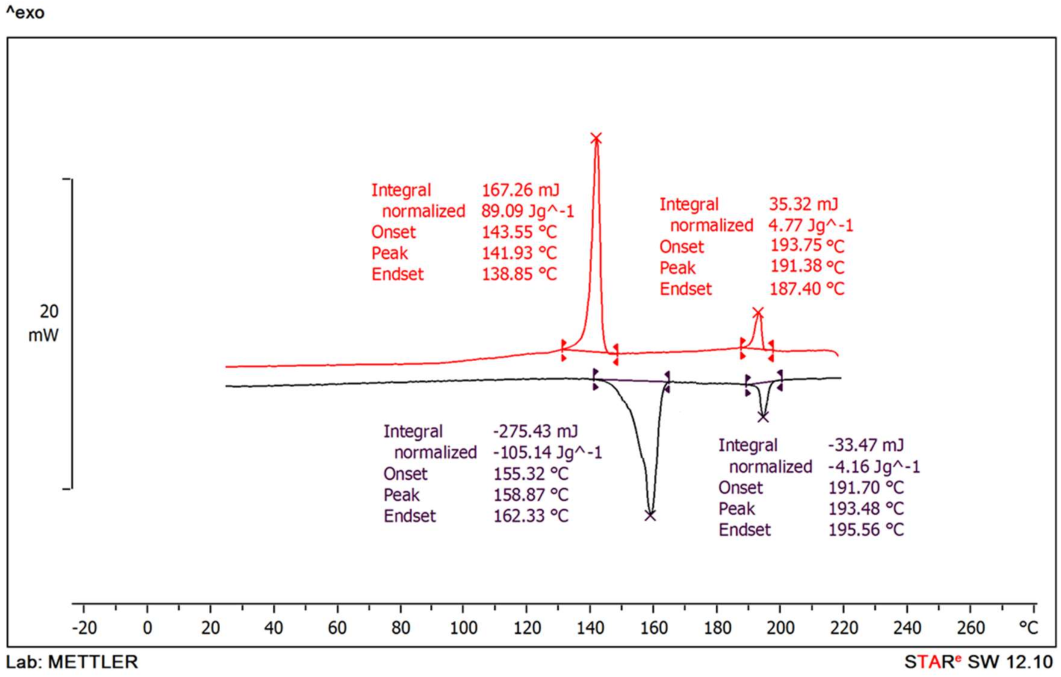

Fig. S3.65: DSC thermogram of *IV-10*

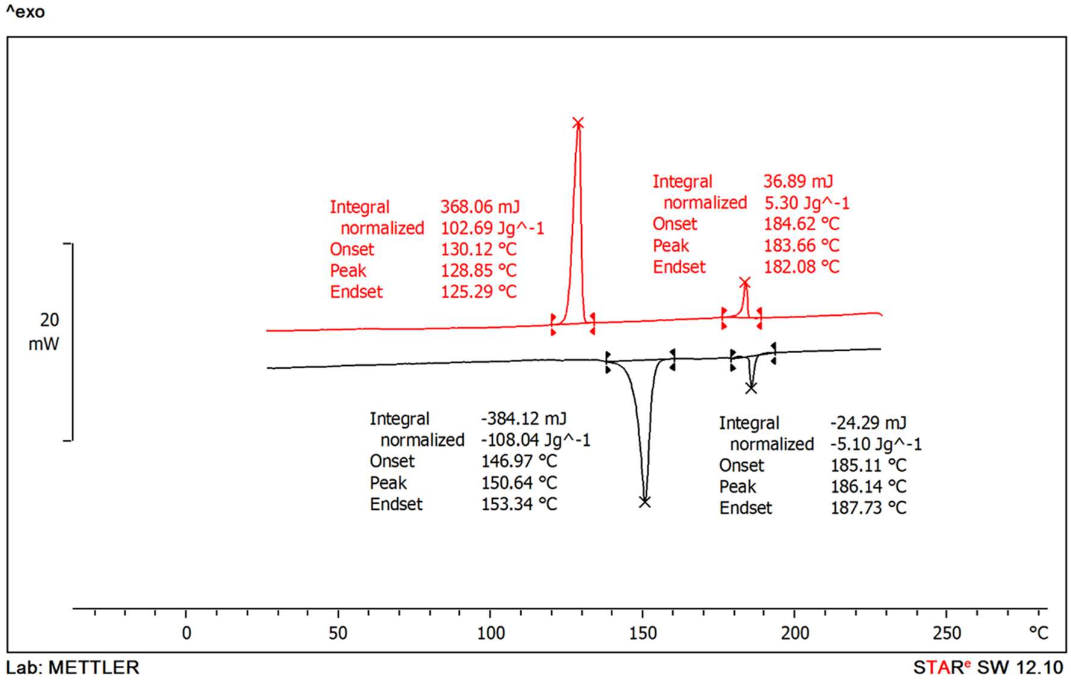

Fig. S3.66: DSC thermogram of *IV-12*

3.8 References

1 C. T. Imrie and P. A. Henderson, *Chem. Soc. Rev.*, 2007, **36**, 2096–2124.

2 C. T. Imrie, *Liq. Cryst.*, 2006, **33**, 1449–1485.

3 R. J. Mandle, M. P. Stevens and J. W. Goodby, *Liq. Cryst.*, 2017, **44**, 2046–2059.

4 S. S. Subala, B. S. Sundar and S. S. Sastry, *J. Chem.*, 2013, **2013**, 939406.

5 D. A. Paterson, R. Walker, J. P. Abberley, J. Forestier, W. T. A. Harrison, J. M. D. Storey, D. Pociecha, E. Gorecka and C. T. Imrie, *Liq. Cryst.*, 2017, **44**, 2060–2078.

6 B. Bai, H. Wang, X. Lin, X. Ran, C. Zhao and M. Li, *Lett. Org. Chem.*, 2012, **9**, 76–80.

7 T. N. Chan, Z. Lu, W. S. Yam, G. Y. Yeap and C. T. Imrie, *Liq. Cryst.*, 2012, **39**, 393–402.

8 A. Martínez-Felipe and C. T. Imrie, *J. Mol. Struct.*, 2015, **1100**, 429–437.

9 S. Pan, B. Mu, Y. Zhou, Q. Li, B. Wu, J. Fang and D. Chen, *RSC Adv.*, 2016, **6**, 49556–49566.

10 M. C. Varia, S. Kumar and A. K. Prajapati, *Liq. Cryst.*, 2012, **39**, 933–942.

11 N. G. Nagaveni, V. Prasad and A. Roy, *Liq. Cryst.*, 2013, **40**, 1001–1015.

12 R. Yang, D. Zhao, G. Dong, Y. Liu and D. Wang, *Crystals*, 2018, **8**, 147.

13 S. M. Gan, A. R. Yuvaraj, M. R. Lutfor, M. Y. Mashitah and H. Gurumurthy, *RSC Adv.*, 2015, **5**, 6279–6285.

14 L. Ma, Y. Xia, D. Li and R. Hou, *Liq. Cryst.*, 2021, **48**, 1095–1102.

15 G. Y. Yeap, H. C. Lee, W. A. K. Mahmood, C. T. Imrie, D. Takeuchi and K. Osakada, *Phase Transitions*, 2011, **84**, 29–37.

16 G. Y. Yeap, T. C. Hng, D. Takeuchi, K. Osakada, W. Ahmad Kamil Mahmood and M. M. Ito, *Mol. Cryst. Liq. Cryst.*, 2009, **506**, 134–149.

17 G. Y. Yeap, F. Osman and C. T. Imrie, *J. Mol. Struct.*, 2016, **1111**, 118–125.

18 C.-K. Seou, H. Tiong, Y.-F. Win and G.-Y. Yeap, *Lett. Org. Chem.*, 2023, **20,** 632-646

19 Z. Rabeea Banoon, A. Kareem A. Al-Lami, A. M. Abbas, M. Al-Shakban, B. A. A. Balboul, M. Gad, E. A. El Fadaly, M. M. Khalifa, H. Ahmed Rudayni, H. E. Alfassam, A. A. Allam, M. R. Abukhadra, M. Hamdy Eid and M. A. Abdelzaher, *Results Chem.*, 2023, **6**, 101166.

20 G. S. Attard, S. Garnett, C. G. Hickman, C. T. Imrie and L. Taylor, *Liq. Cryst.*,

1990, **7**, 495–508.

21 P. J. Le Masurier and G. R. Luckhurst, *J. Chem. Soc. - Faraday Trans.*, 1998, **94**, 1753–1760.

22 M. Rabari, Y. Parmar and A. K. Prajapati, *Liq. Cryst.*, 2023, **50**, 2552-2570.

23 G. S. Attard and C. T. Imrie, *Liq. Cryst.*, 1992, **11**, 785–789.

24 G. S. Attard, C. T. Imrie and F. E. Karasz, *Chem. Mater.*, 1992, **4**, 1246–1253.

25 R. Walker, M. Majewska, D. Pociecha, A. Makal, J. M. D. Storey, E. Gorecka and C. T. Imrie, *ChemPhysChem*, 2021, **22**, 461–470.

26 M. Rabari, C. Koli and A. K. Prajapati, *Soft Mater.*, 2024, **22**, 1–12.

27 M. Shukla and S. Saha, *Comput. Theor. Chem.*, 2013, **1015**, 27–33.

28 M. J. Sani, *Comput. Theor. Chem.*, 2023, **1223**, 114100.

29 N. S. Venkataramanan, A. Suvitha and R. Sahara, *Comput. Theor. Chem.*, 2019, **1148**, 44–54.

30 S. Sundaram, V. N. Vijayakumar and V. Balasubramanian, *Comput. Theor. Chem.*, 2022, **1217**, 113920.

31 C. T. Imrie, P. A. Henderson and G.-Y. Yeap, *Liq. Cryst.*, 2009, **36**, 755–777.

32 M. Hagar, H. A. Ahmed and O. A. Alhaddad, *Liq. Cryst.*, 2019, **46**, 2223–2234.

33 H. Alyar, M. Bahat, Z. Kantarcı and E. Kasap, *Comput. Theor. Chem.*, 2011, **977**, 22–28.

34 S. K. Prasad, P. L. Madhuri, P. Satapathy and C. V Yelamaggad, *Appl. Phys. Lett.*, 2018, **112**, 253701.

35 D. A. Paterson, J. Xiang, G. Singh, R. Walker, D. M. Agra-Kooijman, A. Martínez-Felipe, M. Gao, J. M. D. Storey, S. Kumar, O. D. Lavrentovich and C. T. Imrie, *J. Am. Chem. Soc.*, 2016, **138**, 5283–5289.

36 D. Zaton, A. Karamoula, G. J. Strachan, J. M. D. Storey, C. T. Imrie and A. Martinez-Felipe, *J. Mol. Liq.*, 2021, **344**, 117680.

37 K. Prasad, K. L. Sandhya, G. Nair, U. Hiremath and C. Yelamaggad, *J. Appl. Phys. - J APPL PHYS*, 2002, **92**, 838–841.

38 R. Sahoo, C. Reshma, D. S. Shankar Rao, C. V Yelamaggad and S. Krishna Prasad, *J. Mol. Liq.*, 2024, **393**, 123443.

39 Y. Zhang, S. Pei, Y. Wang, Z. Cui, N. Li, Y. Zhu, H. Zhang and Z. Jiang, *Dye. Pigment.*, 2013, **99**, 1117–1123.

40 C.-Z. Zhang, *Acta Crystallogr. Sect. E. Struct. Rep. Online*, 2008, **64**, 618.

41 G. K. Joshi, K. N. Blodgett, B. B. Muhoberac, M. A. Johnson, K. A. Smith and R. Sardar, *Nano Lett.*, 2014, **14**, 532–540.

42 K. E. Lee, J. U. Lee, D. G. Seong, M.-K. Um and W. Lee, *J. Phys. Chem. C*, 2016, **120**, 23172–23179.

43 C. A. Rezende, L.-T. Lee and F. Galembeck, *Microsc. Microanal.*, 2005, **11**, 110–113.

44 C. J. Barrett, J. Mamiya, K. G. Yager and T. Ikeda, *Soft Matter*, 2007, **3**, 1249–1261.

45 L. Dong, Y. Feng, L. Wang and W. Feng, *Chem. Soc. Rev.*, 2018, **47**, 7339–7368.

46 Z. Wang, R. Losantos, D. Sampedro, M. Morikawa, K. Börjesson, N. Kimizuka and K. Moth-Poulsen, *J. Mater. Chem. A*, 2019, **7**, 15042–15047.

47 T. Eom, W. Yoo, S. Kim and A. Khan, *Biomaterials*, 2018, **185**, 333–347.

48 N. Delorme, J.-F. Bardeau, A. Bulou and F. Poncin-Epaillard, *Langmuir*, 2005, **21**, 12278–12282.

49 P. Arya, J. Jelken, N. Lomadze, S. Santer and M. Bekir, *J. Chem. Phys.*, 2020, **152**, 24904.

50 C. Qin, Y. Feng, W. Luo, C. Cao, W. Hu and W. Feng, *J. Mater. Chem. A*, 2015, **3**, 16453–16460.

51 M. Alemani, M. V Peters, S. Hecht, K.-H. Rieder, F. Moresco and L. Grill, *J. Am. Chem. Soc.*, 2006, **128**, 14446–14447.

52 N. Al-Aqtash and R. Sabirianov, *J. Mater. Chem. C*, 2014, **2**, 6873–6878.

53 T. Asano, T. Okada, S. Shinkai, K. Shigematsu, Y. Kusano and O. Manabe, *J. Am. Chem. Soc.*, 1981, **103**, 5161–5165.

54 S. Loudwig and H. Bayley, *J. Am. Chem. Soc.*, 2006, **128**, 12404–12405.

55 B. Kumar, A. K. Prajapati, M. C. Varia and K. A. Suresh, *Langmuir*, 2009, **25**, 839–844.

56 B. Kumar and K. A. Suresh, *Phys. Rev. E*, 2009, **80**, 21601.

57 H.-K. Shin, J.-M. Kim, Y.-S. Kwon, E. Park and C. Kim, *Opt. Mater. (Amst).*, 2003, **21**, 389–394.

58 S. N. Yogitha, B. Kumar, Raghavendra, Imranpasha and S. K. Gupta, *Mater. Sci. Eng. B*, 2021, **267**, 115094.

59 F. Serra and E. M. Terentjev, *Macromolecules*, 2008, **41**, 981–986.

60 K. S. Schanze, T. F. Mattox and D. G. Whitten, *J. Am. Chem. Soc.*, 1982, **104**, 1733–1735.

61 S. Smith and F. Bou-Abdallah, *J. Thermodyn. Catal.*, 2017, **8**, 1–6.

62 Z. F. Liu, K. Morigaki, T. Enomoto, K. Hashimoto and A. Fujishima, *J. Phys. Chem.*, 1992, **96**, 1875–1880.

63 I. Mita, K. Horie and K. Hirao, *Macromolecules*, 1989, **22**, 558–563.

64 H. Rau, *ChemInform*.

65 I. Muzikante, L. Gerca, E. Fonavs, M. Rutkis, D. Gustina, E. Markava, B. Stiller, L. Brehmer and G. Knochenhauer, *Mater. Sci. Eng. C*, 2002, **22**, 339–343.

66 K. S. Yim and G. G. Fuller, *Phys. Rev. E*, 2003, **67**, 41601.

67 Raghavendra, S. K. Gupta and B. Kumar, *Colloid Polym. Sci.*, 2021, **299**, 603–609.

68 S. Samai, D. J. Bradley, T. L. Y. Choi, Y. Yan and D. S. Ginger, *J. Phys. Chem. C*, 2017, **121**, 6997–7004.

69 Raghavendra and B. Kumar, *Thin Solid Films*, 2021, **732**, 138764.

70 Y. Zhang, S. Pei, Y. Wang, Z. Cui, N. Li, Y. Zhu, H. Zhang and Z. Jiang, *Dye. Pigment.*, 2013, **99**, 1117–1123.

71 C.-Z. Zhang, *Acta Crystallogr. Sect. E. Struct. Rep. Online*, 2008, **64**, o618.